

1837
2017
YEARS



HELLENIC REPUBLIC

**National and Kapodistrian
University of Athens**

Mineralogy & Geochemistry of Fe-bearing clay minerals
in stylolites of carbonate formations of NW Greece

Master Thesis

Eleni S. Mloukie

Supervisor: Assistant Professor Dr. Athanasios Godelitsas

Athens, Greece

July, 2019

Contents

1. Introduction	01
1.1. Clay Minerals	01
1.2. Formation of minerals in chemical compaction (pressure-solution) features. Stylolites.	04
1.3. Study Area	11
1.4. Scope of the present study	14
2. Materials and Methods	15
2.1. Samples and preparation	15
2.2. Powder X-Ray Diffraction (XRD)	16
2.3. Electron microscopic study (SEM-EDS)	16
2.4. Bulk geochemical analyses by Inductively-Coupled Plasma Emission/Mass-Spectrometry (ICP-ES/MS)	17
2.5. Mössbauer spectroscopy	17
2.6. TEM-EDS	18
3. Results	19
3.1. Mineralogy	19
3.1.1. X-Ray Diffraction (XRD) analyses of specimens	19
3.1.2. Scanning Electron Microscope - Energy Dispersive Microanalyses (SEM-EDS)	22
3.2. Geochemistry	30
3.3. Fe-speciation	40
3.4. Nanomineralogy	43
4. Discussion & Conclusions	60
5. References	63

1. Introduction

1.1 Clay Minerals

Clay minerals are hydrous aluminosilicates with a sheet or layered structure and are part of the phyllosilicate family (Weaver 1989, Tucker 2001). They are fine-grained and were initially defined as consisting of grains less than 2 μm in diameter, beyond the limit of microscopic resolution, although nowadays in many instances, the phyllosilicate minerals have been proven to be silt-sized (Velde 1992, Weaver 1989). This was a definition of the nineteenth century, which had only microscopic means of investigation (Velde 1992).

The layer silicates are constructed of planes of atoms forming tetrahedral and octahedral sheets arranged in various combinations (Bailey 1980). The tetrahedral sheets are composed of tetrahedra interconnected, by sharing oxygen ions at three corners each. The basal oxygens (shared oxygens) form an infinite two-dimensional hexagonal pattern. The fourth tetrahedral oxygen (apical oxygen) of all tetrahedra is perpendicular to the sheet and forms a corner of the adjacent octahedral sheet. In the octahedral sheet, each octahedron connects to its neighbouring octahedra by sharing edges. Sheets of hexagonal or pseudo-hexagonal symmetry are formed by edge-shared octahedra. The tetrahedral cations are primarily Si^{4+} and Al^{3+} , and rarely Fe^{3+} , but Be, B, Ga, and Ge are also documented. Octahedral cations are usually Al^{3+} , Fe^{3+} , Mg^{2+} , Fe^{2+} , but other cations, such as Li^+ , Mn^{2+} , Co^{2+} , Ni^{2+} , Cu^{2+} , Zn^{2+} , V^{3+} , Cr^{3+} , and Ti^{4+} are also observed. The cations comprising the octahedral sheet are octahedrally coordinated by shared apical oxygens plus unshared OH's that lie at the centre of the hexagonal hole formed by basal oxygens (Fig.1) (Weaver 1989, Brigatti et al. 2011).

The stacking arrangement of the sheets determines the clay-mineral type, as does the replacement of Si and Al ions by other elements. Structurally, the two basic groups of clay minerals are the kandite group and smectite group (Tucker 2001). Members of the kandite group have a two-layered structure consisting of a silica tetrahedral sheet linked to an alumina octahedral (gibbsite) sheet by common O/OH ions (Fig.1). Replacement of Al and Si does not occur so that the structural formula is $(\text{OH})_4\text{Al}_2\text{Si}_2\text{O}_5$. Members of the kandite group are kaolinite, by far the most important, the rare dickite and nacrite, which have a different lattice structure, and halloysite, which consists of kaolinite layers separated by sheets of water. Related structurally to kaolinite are the alumino-ferrous silicates berthierine and chamosite and the ferrous silicate greenalite (Tucker 2001). Kaolinite has a basal spacing, i.e. distance between one silica layer and the next, of 7 Å. Members of the smectite group have a three-layered structure in which an alumina octahedral layer is situated between two layers of silica tetrahedra (Fig.1). Smectites have a basal spacing typically, of 14 Å, but their ability to absorb water molecules can change the basal spacing, which may vary from 9.6 Å (with no

adsorbed water) to 21.4 Å (Tucker 2001). The common smectite is montmorillonite; it approximates to $Al_4(Si_4O_{10})_2(OH)_4 \cdot nH_2O$ but the substitution of the Al^{3+} by Fe^{2+} , Mg^{2+} and Zn^{2+} can take place. A net negative charge resulting from such substitutions is balanced by other cations, especially Ca^{2+} and Na^+ , which are contained in interlayer positions.

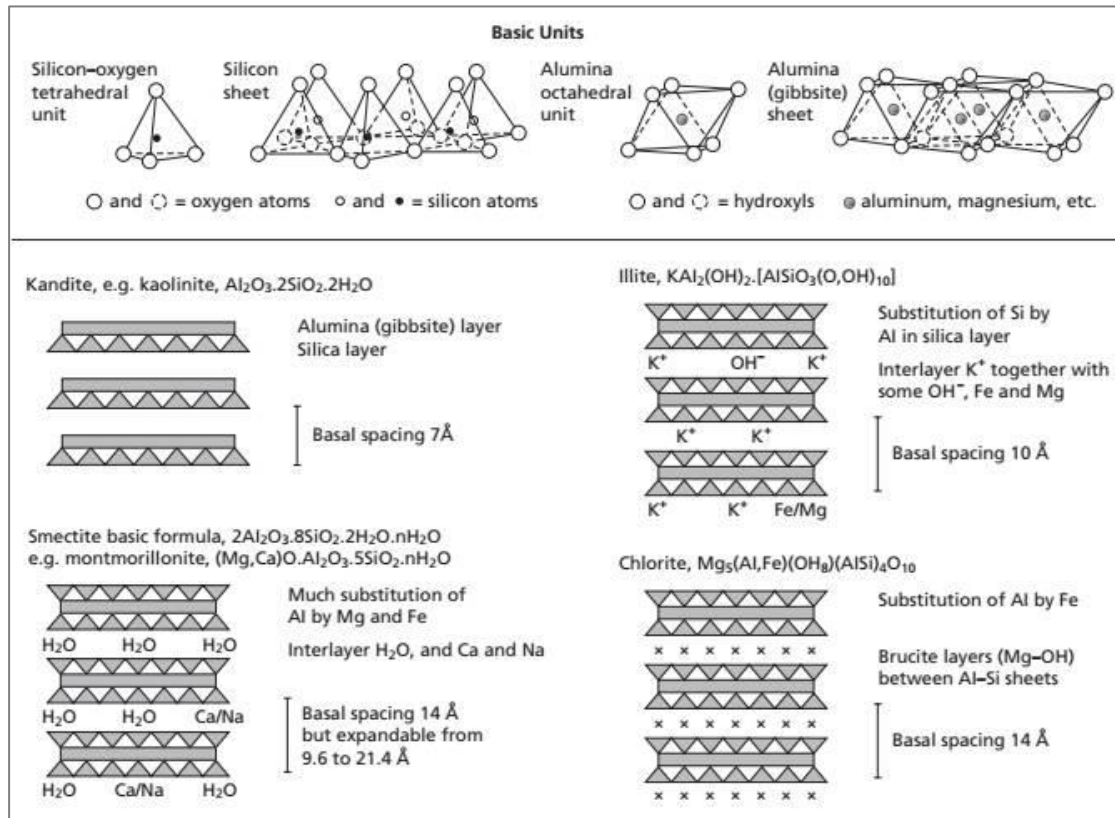


Figure 1. Diagrams illustrating the structures of clay minerals (from Tucker 2001).

Clay minerals occur in all types of sediments and sedimentary rocks and are the most abundant minerals in these rocks, perhaps comprising as much as 40% of the minerals in them. The most common clay minerals in the Earth's crust are illite, followed, in order of relative abundance, by montmorillonite, kaolinite and chlorite, as well as, mixed-layer clays like illite-montmorillonite, and chlorite-montmorillonite.

During weathering and diagenesis, interlayer cations can be leached out of the clay minerals by percolating waters. Such non-stoichiometric clays are termed *degraded* and in fact many illites and smectites in modern sediments are degraded, as well as some chlorites, biotites and muscovites (Tucker 2001). In view of their fine crystal size and the presence of unsatisfied bonds, clay minerals are important in the process of ion exchange. Ions in aqueous solutions can be adsorbed onto and desorbed from clays, with the water chemistry controlling the exchange process. Some elements, such as iron and manganese can be transported by adsorption on clays (Tucker 2001).

The fine grained micas belong to the illite family. The dioctahedral illites greatly predominate over the trioctahedral. Like the smectites, illite has a three-layered

structure, but Al^{3+} substitution for Si^{4+} in the tetrahedral layer results in a deficit of charge, which is balanced by potassium ions in interlayer positions (Weaver 1973, Tucker 2001). Statistically illite is predominantly of a dioctahedral type close to muscovite. Nevertheless illite generally contains more Si, Mg, H_2O and less K than ideal muscovite. In fact the term illite can designate all types of small micas, and sometimes corresponds to a mixture of micaceous minerals of different origins. Illite basal spacing is about 10 Å and some hydroxyl OH^- , Fe^{2+} and Mg^{2+} ions also occur (Weaver 1973, Tucker 2001).

The dioctahedral iron illites are the minerals glauconite and celadonite. Glauconite is also used as a rock name and is applied to any aggregate of fine-grained, green, layer minerals. The iron illite layers, alike the aluminum illites, similar to the aluminum illites, occur interlayered with montmorillonite-like layers. In glauconites more than half the octahedral positions are filled with iron, the more abundant being ferric iron (Weaver & Pollard 1973, Velde 1992). The aluminum content of the tetrahedral sheet is usually less than that of the aluminum illites and the magnesium content of the octahedral sheet greater. Celadonite has more octahedral Mg and less tetrahedral Al than glauconite (Weaver & Pollard 1973, Velde 1992).

1.2 Formation of minerals in chemical compaction (pressure-solution) features. Stylolites.

Carbonate sediments are highly affected by diagenesis, almost since their deposition. Diagenesis encompasses all the processes which affect the sediments after deposition until above the realm of low-grade metamorphism, at elevated temperatures and pressures. Diagenesis includes processes such as cementation to produce limestones and dissolution to form cave systems but it also includes more subtle processes such as the development of microporosity and changes in trace element and isotopic signatures (Tucker & Wright 1990). Diagenetic changes can begin on the seafloor, as the grains are still being washed around or as a reef is still growing, or it may hold off until burial when overburden pressure has increased or pore-fluid chemistry has changed so that reactions are then induced within the sediments (Choquette & James 1987, Tucker & Wright 1990). Carbonate diagenesis operates in three principal environments: the marine, near-surface meteoric and burial environments, and there are features of the cement fabrics and other textures which are diagnostic of a particular diagenetic environment (Fig.2) (Tucker & Wright 1990, Tucker & Bathurst 2009, Moore & Wade 2013).

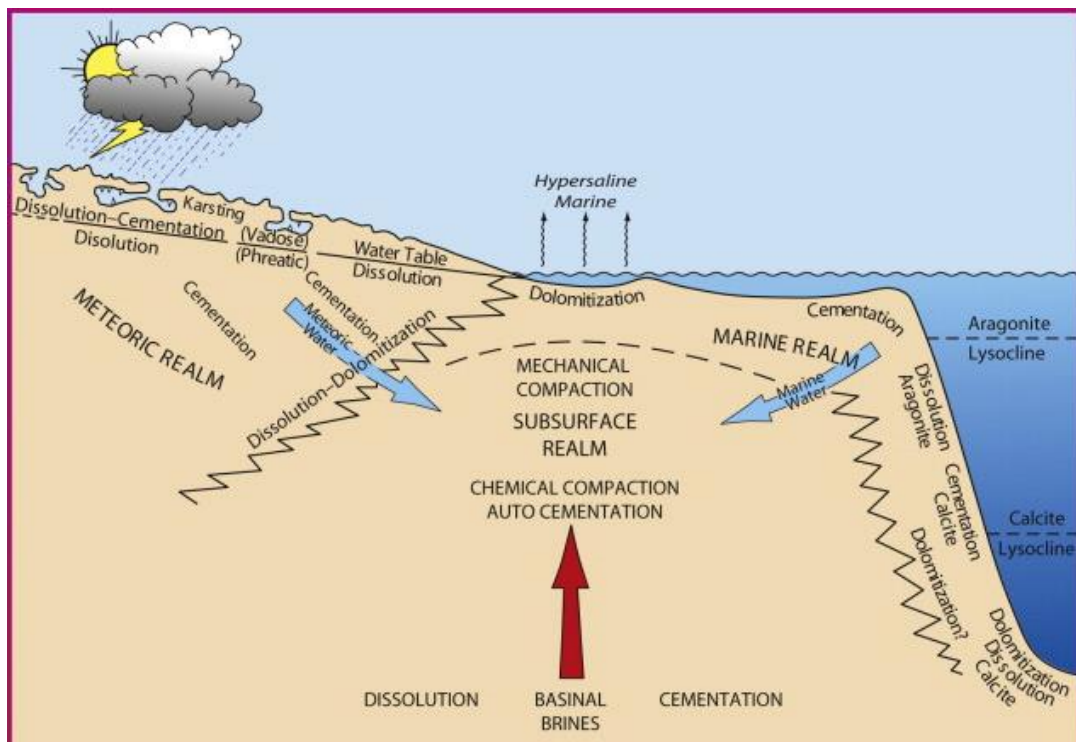


Figure 2. Diagenetic environments and processes (after Moore & Wade 2013)

Burial diagenesis represents alteration that occurs below the zone of near-surface water circulation (i.e., below the meteoric phreatic mixing zone or below the zone of active seawater circulation) and above the realm of low-grade metamorphism (Choquette & Pray 1970, Bathurst 1975, Choquette & James 1987, Tucker & Wright 1990, Scholle & Usher-Scholle 2003). It may begin at depths of a very few metres to a few hundreds of metres beneath subaerial surfaces, and a metre or so to very few tens of metres beneath sea-floor surfaces (Choquette & James 1987). The effects are progressive, subtle at first, obvious later, so that it is usually not possible to pinpoint the onset of burial diagenetic effects and in ancient limestones it is often very difficult to relate the products of burial diagenesis to precise depths. Shallow-marine carbonates enter the burial diagenetic realm from one of two standpoints: they may be buried directly from the marine environment, with marine pore-fluids, or they may be affected by meteoric diagenetic processes first, so that sediment mineralogy is stabilized and pore-fluids are fresh or mixed marine-meteoric. The early diagenetic history of a carbonate sediment has important considerations during later, burial diagenesis (Tucker & Wright 1990).

Burial diagenesis is mainly a consequence of overburden due to burial beneath younger strata and of resulting changes in hydrology, pore-water chemistry, pressure and temperature (Choquette & James 1987, Moore 1989). Complex arrays of processes are operative in the deep-burial diagenetic environment (Table 1). Dominant among them are physical (mechanical) compaction and dewatering, chemical compaction (pressure-solution), cementation, sub-surface dolomitization, alteration of hydrous minerals to anhydrous ones, thermally driven mineral stabilization reactions, and alteration and maturation of organic acids and hydrocarbons. Burial diagenesis is also very important in porosity reduction by compaction and cementation, at increasing temperatures and pressures, in the presence of pore waters (Choquette & Pray 1970, Choquette & James 1987, Moore 1989, Tucker & Wright 1990, Scholle & Usher-Scholle 2003). Important changes may occur over burial-history time spans of 10^6 - 10^8 years, although the rates of some modifications, such as mechanical compaction, will commonly fall off rapidly with increasing depths of burial (Choquette & Pray 1970, Tucker & Bathurst 2009).

In this environment, diagenetic fluids are cut off from free exchange with chemically active gases of the atmosphere (most particularly oxygen and CO_2) temperature and pressure progressively increase and the exchange of diagenetic fluids diminishes because of continuous porosity reduction. Pore fluids undergo a slow compositional evolution driven by rock-water interaction and mixing of basin-derived waters (Moore 1989). Subsurface (or formation) waters are generally brines, with salinities reaching several 100‰ and in many basins there is an increase in salinity with depth. The chemical composition of subsurface brines is rather different from surface waters. Expressing the composition relative to seawater, it is usually found that subsurface

brines are strongly depleted in K^+ , Mg^{2+} , and SO_4^{2-} , slightly depleted in Na^+ and considerably enriched in moderately saline brines, and the relative proportions of both Ca^{2+} and K^+ increase with increasing salinity (Tucker & Wright 1990). There is also a higher molar Ca/Mg ratio (average 3.5) in subsurface water compared to seawater (0.19). Subsurface brines are derived from mixtures of meteoric water, seawater, and juvenile and magmatic waters (Moore 1989, Tucker & Wright 1990).

General processes and products in the deep-burial domain.	
Processes	Products
Physical compaction	Reduced thickness, porosity and permeability; Re-oriented and commonly broken allochems; Compressed textures and structures
Chemical compaction	Reduced thickness, porosity and permeability; Stylolites and other pressure-solution structures; Ions for new carbonate cement
Cementation	Mosaic/drusy to very coarse or poikilotopic calcite and saddle dolomite
Burial dolomitization	Anhedral-crystalline dolomite, generally rather coarse
Mineral reactions	Smectite to illite Gypsum to anhydrite Opal A and CT to quartz Fe hydroxides to Fe oxides
Biochemical alteration of organic matter	Kerogen and organic acids
Thermochemical alteration of kerogen	Hydrocarbons and CO_2
Burial dissolution of Ca, carbonate and sulphate	Solution porosity

Table 1. General processes and products in the deep-burial domain (*after Choquette & James 1987*)

Once a carbonate sediment has been mechanically compacted, and a stable grain framework has been established (regardless of whether the grains are mud-sized or sand-sized), continued burial will increase the elastic strain at individual grain contacts. Increased strain leads to an increased chemical potential, reflected as an increase in solubility at the grain contact, and ultimately resulting in point dissolution at the contact. Away from the grain contact, elastic strain is less, the relative solubility of calcium carbonate reduced, and ions diffusing away from the site of dissolution will tend to precipitate on the unstrained grain surfaces (Bathurst 1975, Moore 1989). Chemical compaction and pressure dissolution are very important burial processes (Fig.3). Apart from producing a range of dissolution textures, they also result in the dissolution of grains and sediment, and this may be a significant source of CaCO₃ for burial cementation (Bathurst 1975, Moore 1989, Tucker & Wright 1990). A thin film of water exists at the site of pressure dissolution and ions going into solution may join the main pore-fluid reservoir of the limestone (Fig.4). A chemical potential gradient is set up with ions moving away from the pressure dissolution site by diffusion or solution transfer. The CaCO₃ in solution may be reprecipitated as a cement in the immediate vicinity, where the stress field is lower, or carried away in an active pore-fluid system to a more distant site of precipitation. The stresses arise from increasing overburden but also from tectonic stress (Bathurst 1975, Choquette & James 1987, Moore 1989). The dissolution of limestone leads to the accumulation of insoluble residue which mostly consists of clay minerals, iron oxides/hydroxides and organic matter (Tucker & Wright 1990). Pressure solution (Fig.5) is manifested in a variety of scales from the microscopic, sutured, grain contacts generated during grain-to-grain pressure solution, to the classic, macroscopic, high-amplitude stylolites that generally cut across most textural elements of the rock along with a number of intermediate forms, such as horsetails, solution seams, and others (Bathurst 1975, Bathurst 1984, Moore 1989).

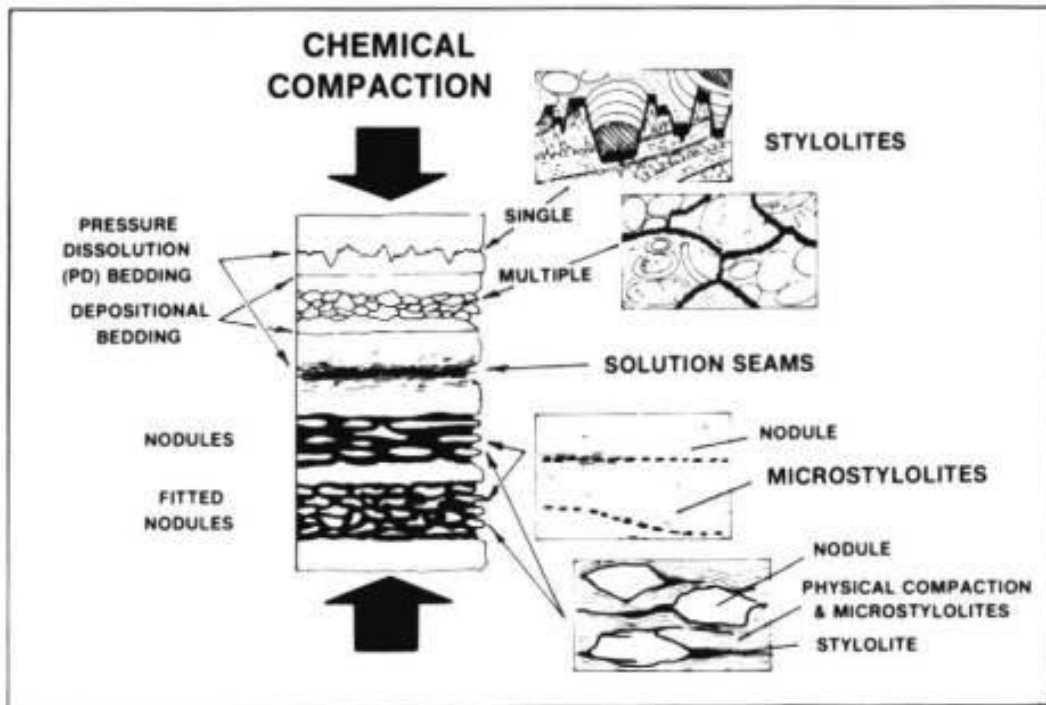


Figure 3. Sketches of features produced by chemical (pressure-solution) compaction (after Choquette & James 1987)

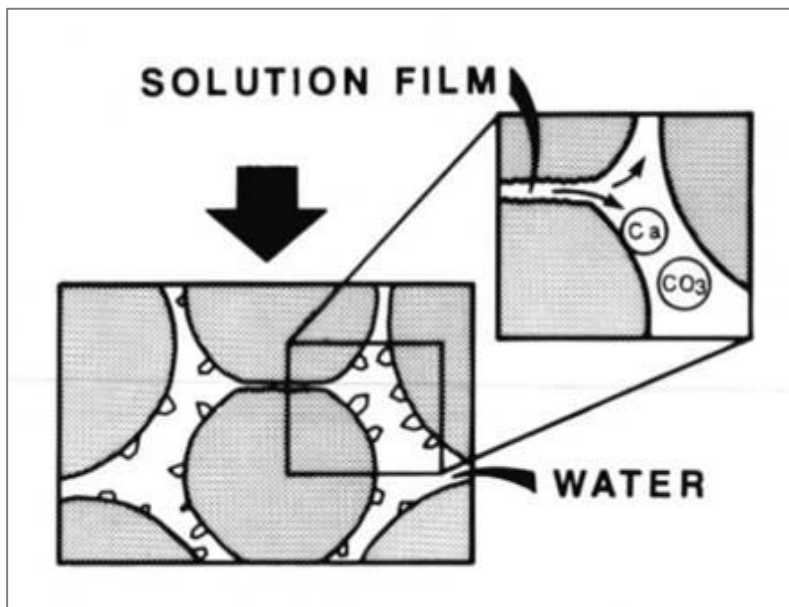


Figure 4. A conceptual sketch of elements on a microscale involved in pressure-solution of two grains pressed together at a sutured contact (after Choquette & James 1987)


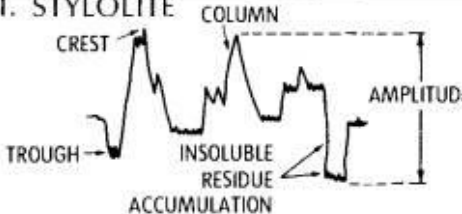


<p>I. MICROSTYLOLITE</p> 	<ol style="list-style-type: none"> 1. Sutured contacts between interpenetrating grains 2. Amplitude < .25mm 3. Minor insoluble residue
<p>II. STYLOLITE</p> 	<ol style="list-style-type: none"> 1. Sutured surface of interpenetrating columns 2. Laterally continuous surface on core scale 3. Amplitude ≥ 1cm 4. Variable insoluble residue accumulation among surfaces and along individual surfaces
<p>III. WISPY SEAM</p> 	<ol style="list-style-type: none"> 1. Converging and diverging sutured to undulose surfaces 2. Individual surfaces laterally discontinuous on core scale 3. Individual surface amplitude < 1cm 4. Insoluble residue accumulation along individual surfaces ≤ 1mm
<p>IV. SOLUTION SEAM</p> 	<ol style="list-style-type: none"> 1. Undulose surfaces 2. Laterally continuous on core scale 3. Insoluble residue accumulation ≥ 1mm

Figure 5. Types and characteristics of pressure solution features encountered in the subsurface (after Moore 1989).

Stylolites are a prominent feature of many limestones and are a serrated interface between two rock masses, with a sutured appearance in cross-section. The amplitude of the suture is much greater than the diameters of the sediment grains. Stylolites transect the rock fabric, cutting across grains, cement and matrix indiscriminately. They are normally absent in limestones with more than 5-10% clay (Choquette & Pray 1970, Tucker & Wright 1990). The initial surface at which dissolution begins is generally parallel to the bedding, though all orientations are known including surfaces perpendicular to the bedding. The controlling factor is the orientation of the axis of linear stress and this is generally vertical, being a simple consequence of overburden. Stylolites can in places be traced laterally into bedding planes. The zig-zag form of the surface is presumed to be a consequence of lateral variations, along the interface, of solubility differences of the rock across the interface. Where a more soluble part confronts a less soluble part across a solution film, then the more soluble part will dissolve and the less soluble part will move into the resultant space. The process is the same as grain-to-grain pressure solution, in that where the grains are equally soluble under stress they will both dissolve equally, but where they have different stress

solubilities one will dissolve more rapidly than the other (Bathrust 1975). Theoretically, the migration of ions away from the dissolving surfaces can proceed by two paths: either in the stylolite surface film in a fully cemented rock, or away from the surface, parallel to the linear stress axis, in a permeable rock. The stylolite surface is commonly a film of residual non-carbonate material rich in clay (Bathrust 1975).

Higher temperatures and increased pressures at depth, however, tend to accelerate many diagenetic processes. Elevated pore-fluid pressures, which reduce grain-to-grain stress, and early hydrocarbon input, retard mechanical and chemical burial diagenesis.

1.3 Study Area

The study area is located in northwestern Greece at Epirus region (Fig. 6). The samples collected for this study, belong to the Ionian Unit, which consists part of the external Hellenides and are of Senonian age, according to the geological sheet “THESPROTIKON”, created by the Institute of Geology & Mineral Exploration (I.G.M.E.) of Greece, in 1962-63.

During the Pliensbachian, extensional stresses associated with the opening of the Tethys Ocean, resulted in the breaking of the huge carbonate platform that covered western Greece and the opening of the Ionian Basin (Bernoulli and Renz 1970, Karakitsios 1990, Karakitsios 1992). The Ionian Basin was in fact an intra-platform rift basin bounded on the east by Gavrovo-Tripolitza carbonate platform and on the west by the Apulia carbonate platform (Aubouin 1959, Bosellini & Morsilli 1997).

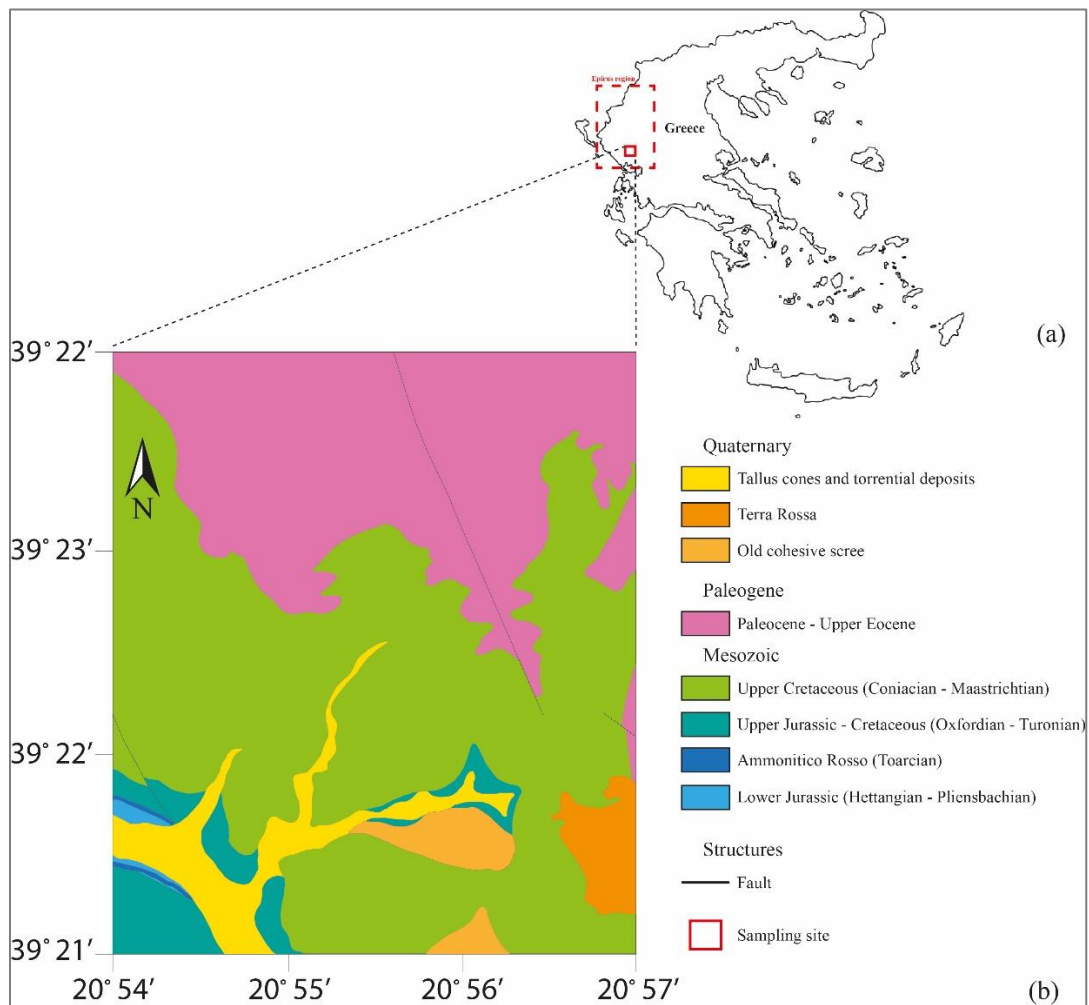


Figure 6. (a) Location of the study area. (b) Geological map showing the Upper Cretaceous pelagic limestones.

Sedimentary rocks comprising the Ionian Unit, range from Triassic evaporates to Jurassic – Upper Eocene carbonates and minor cherts and shales, which are overlain by Oligocene flysch (Karakitsios & Rigakis 2007). Three distinct stratigraphic sequences can be identified in the Ionian Unit (Karakitsios 1992, Karakitsios 1995, Karakitsios et al. 2004, Karakitsios 2013) (Fig. 7):

1. A prerift sequence, represented by the early Liassic Pantokrator Limestones. These shallow water limestones overlie early to middle Triassic evaporites through Foustapidima Limestones of Ladinian-Rhaetian age.
2. A synrift sequence that began with the deposition of the Siniais Limestones and their lateral equivalent, the Louros Limestones of Pliensbachian age. These formations correspond to the general sinking of the Ionian domain (formation of the Ionian basin), which was followed by an intrabasinal differentiation that separated the initial basin into smaller paleogeographic units presenting, in general, a half-graben geometry. This is recorded in the abruptly changing thickness of the synrift formations, forming prismatic synsedimentary wedges, which, in the deeper part of the halfgrabens, include complete Toarcian to Tithonian successions, while in the elevated part of the halfgrabens hiatuses and unconformities are located. Deposition was controlled both by structures formed during the extensional tectonic phase (related to the opening of the Neotethys Ocean), and the halokinesis of the Ionian zone evaporitic base.
3. A postrift sequence defined by an Early Berriasian breakup that is marked by an unconformity at the base of the Vigla Limestones (over the elevated part of the synrift half grabens). The postrift sequence (Vigla Limestones and overlying Alpine formations) largely obscures the synrift structures and, in some cases, directly overlies the Pantokrator Limestones prerift sequence. The permanence of differential subsidence during the deposition of the Vigla Limestones as shown by the strong variation in the thickness of this formation, is probably due to the continuation of halokinetic phenomena of the Ionian zone evaporitic base. This paleogeographic configuration continued with minor off- and on-lap movements along basin margins until the late Eocene, when orogenic movements and flysch sedimentation began.

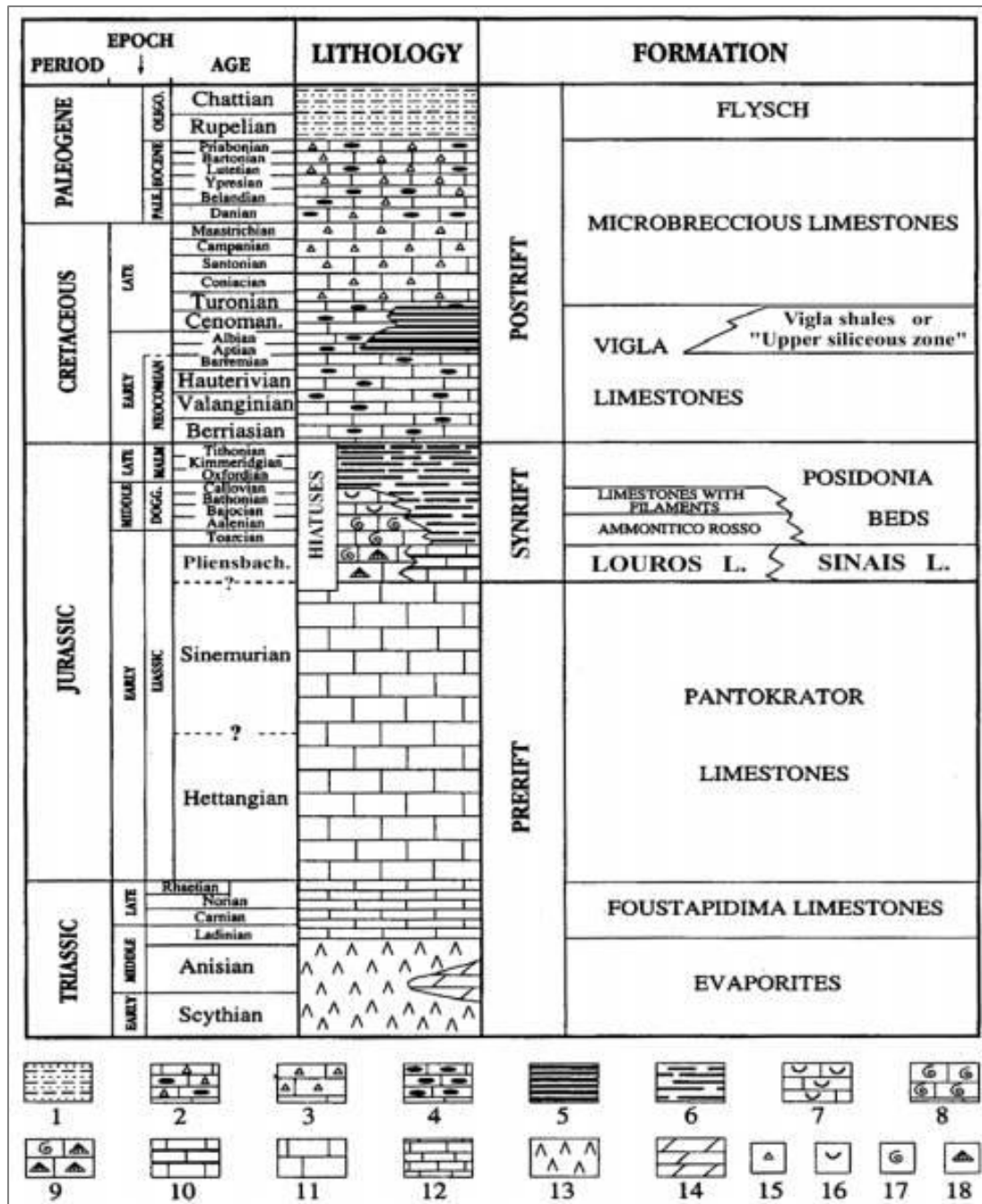


Figure 7. Representative stratigraphic column of the Ionian zone (Karakitsios, 1995). 1: pelites and sandstones; 2: cherty limestone with clastic material; 3: pelagic limestones with clastic material; 5: cherty beds with green and red clay, sometimes shaly; 6: pelagic limestones, marls, and siliceous argillites; 7: pelagic limestones with pelagic lamellibranches; 8: pelagic, red, nodular limestones with ammonites; 9: micritic limestones with small ammonites and brachiopods; 10: pelagic limestones; 11: platform limestones; 12: platy black limestones; 13: gypsum and salt; 14: dolomites; 15: breccia; 16: section of pelagic lamellibranch (filament); 17: ammonite; 18: brachiopod (after Karakitsios et al. 2004).

1.4 Scope of the present study

Fe-bearing clays are important in the study of oxidizing and reducing environments, since they bound Fe^{3+} in a way which is not susceptible to reductive dissolution as Fe oxides are, and so, Fe in clay minerals could act as renewable source of redox equivalents in anoxic environment. Stylolites are one of the main results of chemical compaction, which takes place in the deep burial diagenetic environment and are ubiquitous geo-patterns observed in rocks in the upper crust, from geological reservoirs in sedimentary rocks to deformation zones, in folds, faults, and shear zones. Although, a lot of studies have been conducted through the years, in order to determine their geometrical and compositional characteristics and the factors leading to their genesis, and how can they be used to measure strain and formation stress, the non-carbonate minerals (various types of clays, apatite-group minerals, feldspars, etc.) contained in them are not fully investigated from a mineralogical and geochemical point of view. The current work focuses on the study of Fe-bearing minerals found in stylolites, using a combination of macroscopic, microscopic, analytical and spectroscopic methods. Special emphasis will be given to trace elements' geochemistry by means of discrimination diagrams, etc., and to the Fe oxidation state using Moessbauer spectroscopy, as well as, to the characterization in nanoscale using TEM-EDS. Thus, the entire study is expected to contribute to geological history of the Ionian Unit, as represented in northwestern Greece at Epirus region. The purpose of the present work is to study, for first time in the literature, Fe-bearing minerals found in stylolites, using an overall of analytic methods.

2. Materials and Methods

2.1. Samples and preparation

The samples were collected during the opening of the road A5 Ionia Odos at Epirus region (Fig. 6 & Fig. 8). The specimens concerned stylolite material (sample STYL) and the surrounding limestone (sample LSENON). The material collected from the stylolites of the limestones (Fig. 9 & Fig. 10), was initially grinded by hand with the use of an agate mortar, in order to obtain a homogenized grain size of $\leq 1\text{mm}$. Before the clay minerals could be identified, samples were treated with dilute acetic acid (CH_3COOH), in order to dissolve the carbonates and with hydrogen peroxide (H_2O_2) (3%) for the removal of organic matter.

Separation of silt and clay fraction (sample Fe-CLAY) was conducted by decantation, using the pipette method (Krumbein & Pettijohn 1961, Galehouse 1971, Folk 1974, Tucker 1988). Computation of the diameters of grains from knowledge of their settling velocities is dependent upon the exploitation of Stokes' Law of settling. When a particle in static water settles at a constant velocity the gravitational force exerted on the particle is balanced by fluid resistances represented by viscosity and particle drag coefficient. The balance is normally represented within the equation:

$$V_s = \frac{d^2(p_s - p)g}{18\mu}$$

Where V_s is the settling velocity, d the particle diameter, p_s and p the densities of the grain and water respectively, g is the gravitational acceleration and μ is the dynamic viscosity of the fluid.



Figure 8. The road section from which samples were collected to be studied.



Figure 9. Examined stylolites.



Figure 10. Fe-bearing clayey material (*sample STYL*).

Complete disaggregation is desirable before size separation, so the samples were afore placed in a beaker, covered with distilled water; a small amount of sodium hexametaphosphate solution $[(\text{NaPO}_3)_6]$ 10% was added, as a dispersant agent and they were immersed in an ultrasonic bath.

2.2 Powder X-Ray Diffraction (XRD)

Powder-XRD patterns were obtained using a Siemens (currently Bruker AXS) D-5005 X-ray diffractometer, and the EVA 10.0 program of the BrukerDIFFRACplus software

package, with regard to raw and acid-treated samples ($\text{CuK}\alpha$ radiation at 40 kV and 40 mA, with graphite monochromator).

2.3 Electron microscopic study (SEM-EDS)

The Scanning Electron Microscopic study and the corresponding Energy Dispersive microanalyses (SEM-EDS) were performed using a Jeol JSM-5600 equipped with an Oxford EDS, on both free surfaces (raw and acid-treated samples) and whole rock fragments.

2.4. Bulk geochemical analyses by Inductively-Coupled Plasma Emission/Mass-Spectrometry (ICP-ES/MS)

Further bulk geochemical analyses for major and trace elements were performed, through whole rock analysis by lithium borate fusion, using a Perkin Elmer ICP-OES/MSSPECTRO ARCOS/ELAN[®] 9000, respectively, following the $\text{LiBO}_2/\text{LiB}_4\text{O}_7$ fusion and HNO_3 digestion. The loss on ignition (LOI) was also measured at 1000 °C using standard procedures.

2.5. Mössbauer spectroscopy

Mössbauer spectrometry is based on the quantummechanical “Mössbauer effect,” which provides a nonintuitive link between nuclear and solid-state physics. Mössbauer spectrometry measures the spectrum of energies at which specific nuclei absorb γ rays.

Absorption Mössbauer spectra (MS) were collected with a $^{57}\text{Co}(\text{Rh})$ source moving at room temperature (RT) (Fig. 11), while the absorbers were in a variable temperature cryostat equipped with an electromagnet for magnetic fields up to 7.0 kOe, with the field perpendicular to the gamma-ray beam.



Figure 11.
Mössbauer analysis
hardware.

2.6. TEM-EDS

Nanoscale investigation of clay fraction was performed with a JEOL JEM-2100 LaB6 transmission electron microscope (TEM), operating at 200 kV (Fig. 12). Grain microstructure was also studied using a bright field detector in scanning (STEM) mode. Elemental analyses were carried out using an Oxford X-Max 100 Silicon Drift Energy Dispersive X-ray spectrometer (EDS), connected to TEM; such obtained characteristic X-ray spectra were further interpreted using the Cliff Lorimer qualitative measurement method (thin-film approximation). Data were acquired in areas ranging from 2 to 5 nm in STEM mode.



Figure 12. JEOL JEM-2100 LaB6 transmission
electron microscope (TEM).

3. Results

3.1. Mineralogy

3.1.1. X-Ray Diffraction (XRD) analyses of specimens

X-ray diffraction (XRD)-investigations were carried out to determine the mineral composition of the bulk stylolite material and the clay fracture (<2 μ m) sample and their semiquantitative distribution. XRD analyses were carried out on oriented mounts including air-dried and ethylene-glycolated specimens. Data recording was started at 3 and ended at 64 $^{\circ}2\theta$ with a step size of 0.020 $^{\circ}2\theta$ and a count time of 1 seconds per step for the bulk sample, and at 3 and ended at 24 $^{\circ}2\theta$ with a step size of 0.020 $^{\circ}2\theta$ and a count time of 2 seconds per step for the clay fracture (<2 μ m) sample. XRD analyzing of oriented specimens checked the 00l-spacing and the changing of this spacing that is caused after interlayer space saturation. Based on different minerals modification (Starkey et al. 1984, Moore & Reynolds 1989), the minerals which were presented in oriented mount were identified.

The XRD pattern of the air-dried bulk oriented mount (Fig. 13) showed the presence of quartz, calcite, illite and other clay minerals. While, the XRD pattern of the air-dried clay fracture oriented mount (Fig. 14) showed the presence of illite and probably montmorillonite. The presence of mixed-layered clay minerals is indicated by the reflections occurring between the nominal positions of the 001 peak of both members (*illite-montmorillonite*) and the positions of these intermediate reflections which are fixed by the proportions of the end-members in the interstratifications, and create a broad shape (Méring 1949, Moore & Reynolds 1989). In order to identify mixed-layered species which include smectites successfully, the best method of analysis is to study and compare diffraction patterns produced from both air-dried and ethylene glycol solvated preparations (Méring 1949, Moore & Reynolds 1989).

In the XRD pattern of the ethylene glycol solvated clay fracture oriented mount (Fig. 15) ethylene glycol solvation caused significant changes, which indicates that a smectite component is surely present (Tucker 1988, Moore & Reynolds 1989). Ethylene glycol solvation produced a peak 5.2 $^{\circ} 2\theta$, which along with the strong but broad reflection near the same degrees, suggests that the interstratification is random (Moore & Reynolds 1989). Proportions of illitic layers in the illite/smectite mixed-layer were calculated according to Moore & Reynolds (1997). Based on the relationship between the d-values (\AA) of 001/002 interference and 002/003 interference taken from ethylene-glycolated specimen (Table. 2), the sample was characterized as illite/smectite mixed-layer with 80% -90% illitic layers, respectively.

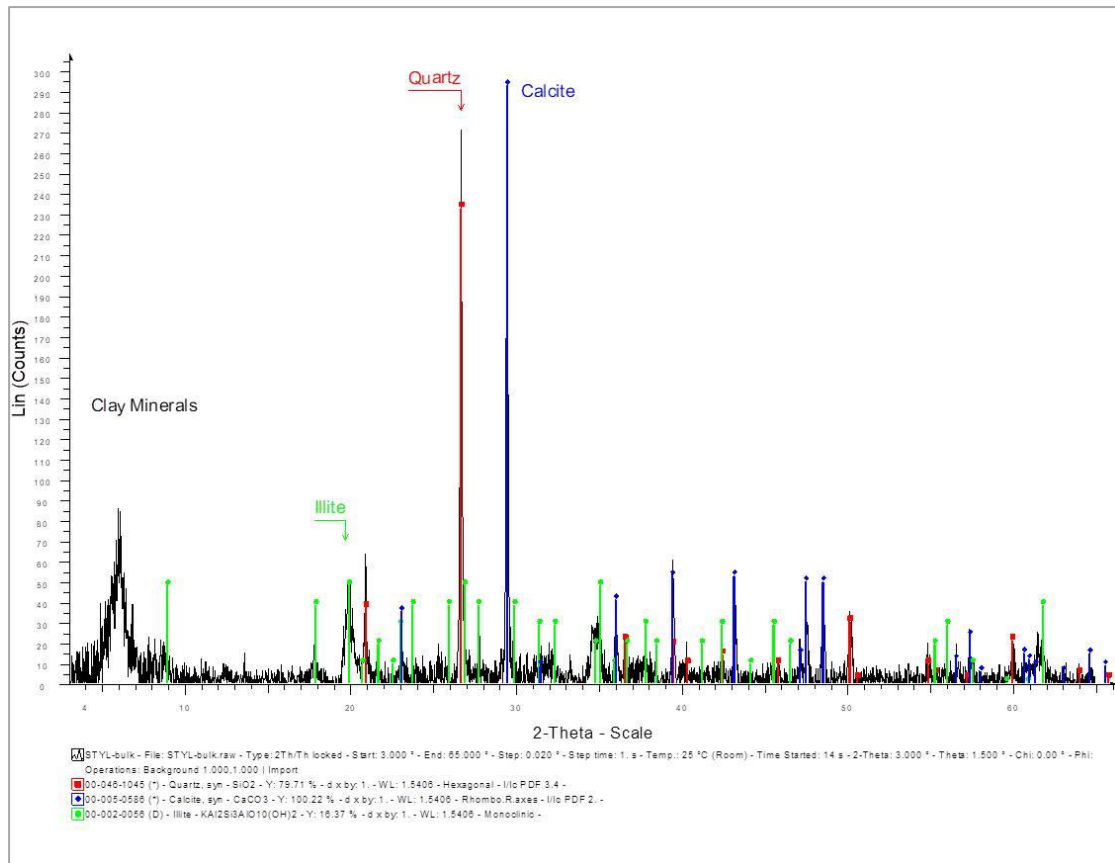


Figure 13. XRD pattern of air-dried bulk sample from oriented specimen, $^{\circ}2\theta$ $\text{CuK}\alpha$ position.

% Illite	Ordering type	<u>001/002</u>		<u>002/003</u>		$^{\circ}\Delta 2\theta$
		d(Å)	$^{\circ}2\theta$	d(Å)	$^{\circ}2\theta$	
10	0	8,58	10,31	5,61	15,80	5,49
20	0	8,67	10,20	5,58	15,88	5,68
30	0	8,77	10,09	5,53	16,03	5,94
40	0	8,89	9,95	5,50	16,11	6,16
50	0	9,05	9,77	5,44	16,29	6,52
60	1	9,22	9,59	5,34	16,60	7,01
70	1	9,40	9,41	5,28	16,79	7,38
80	1	9,64	9,17	5,20	17,05	7,88
90	3	9,82	9,01	5,10	17,39	8,38

Table 2. The positions of reflections for estimating proportion of illitic layer in illite/EG-smectite (after Moore & Reynolds, 1997).

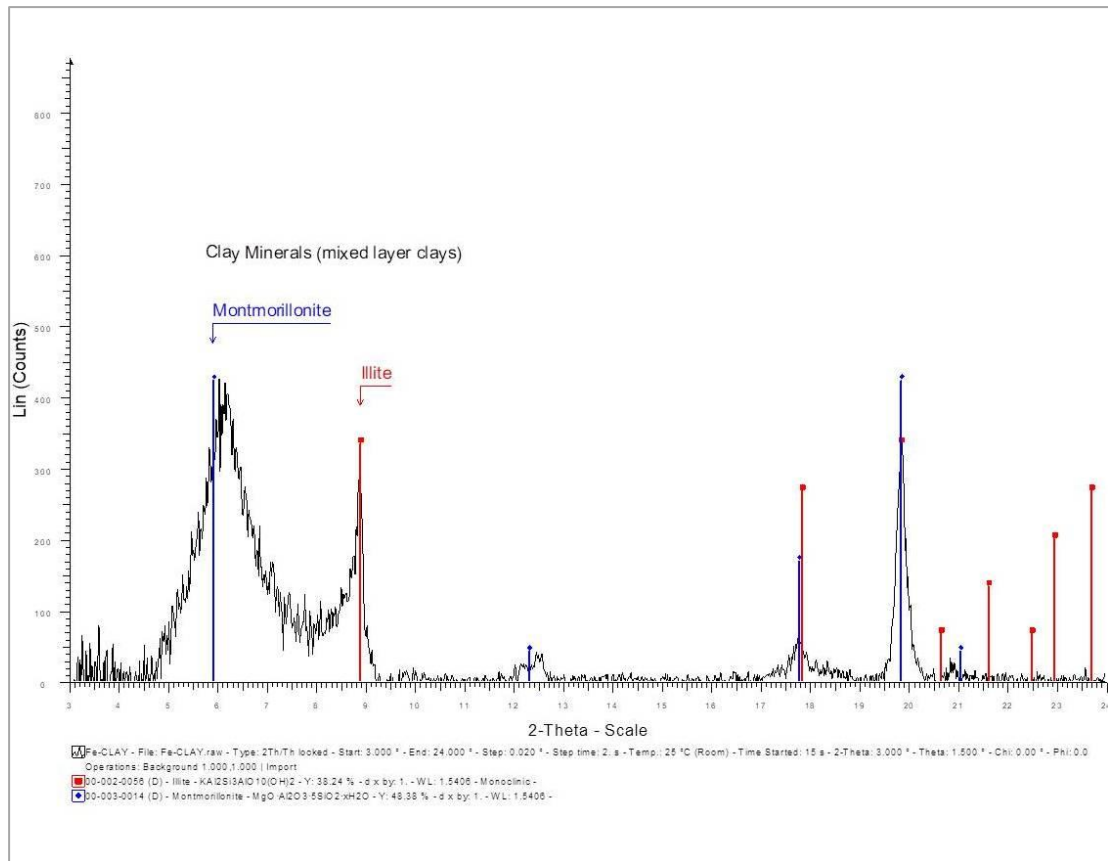


Figure 14. XRD pattern of air-dried clay fracture sample from oriented specimen, $^{\circ}2\theta$ CuK_α position.

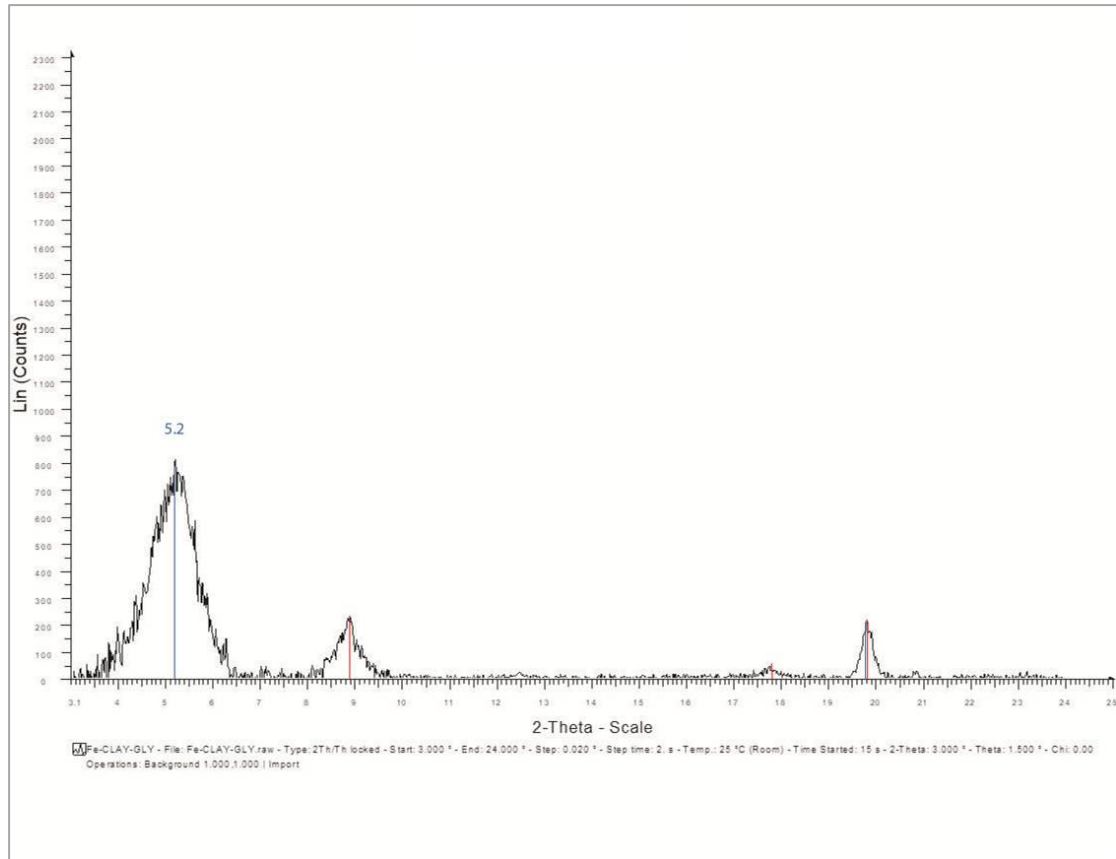


Figure 15. XRD pattern of ethylene glycol solvated clay fracture sample from oriented specimen, $^{\circ}2\theta$ $\text{CuK}\alpha$ position.

3.1.2. Scanning Electron Microscope - Energy Dispersive Microanalyses (SEM-EDS)

The scanning electron microscope was used to examine the textural and morphological features of the limestone, as well as, the chemical composition of the stylolite material. The specimens were prepared by drying at room temperature and carbon coating.

The SEM images of the limestone sample are shown in Fig.16. Scanning electron microscopy showed that the surrounding limestone is micrite, hence a rock composed of carbonate mud (*calclutite*) (Folk 1962). Micrite consists of 1 to 4 μm -diameter crystals and is produced within the basin of deposition and shows little or no evidence of significant transport (Folk 1959).

The SEM-EDS study on the Fe-clay stylolite material revealed that it contains a mixed Al-Si phase, which contains measurable quantity of Fe (Fig. 17-20). This, in comparison with the XRD pattern implies, that the Fe concentration is due to Fe-illite.

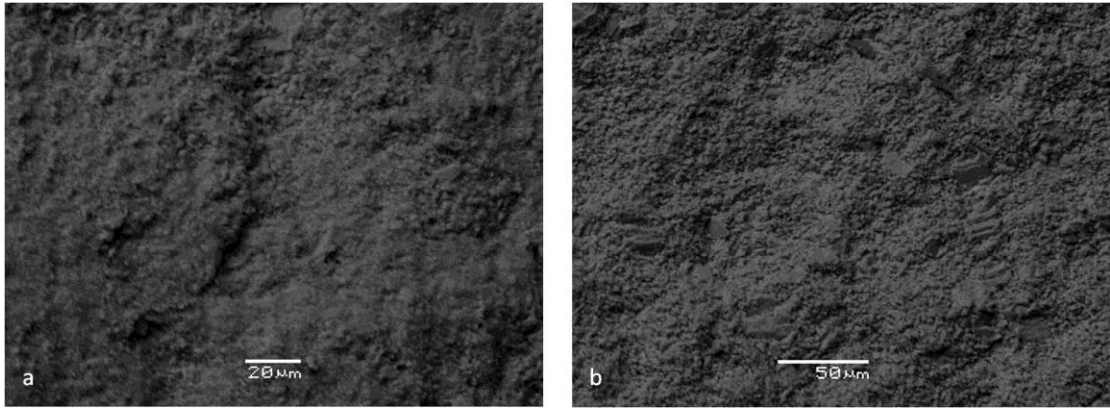


Figure 16. Backscattered electron images (BSI) of: a) micritic limestone; b) detail of micritic limestone.

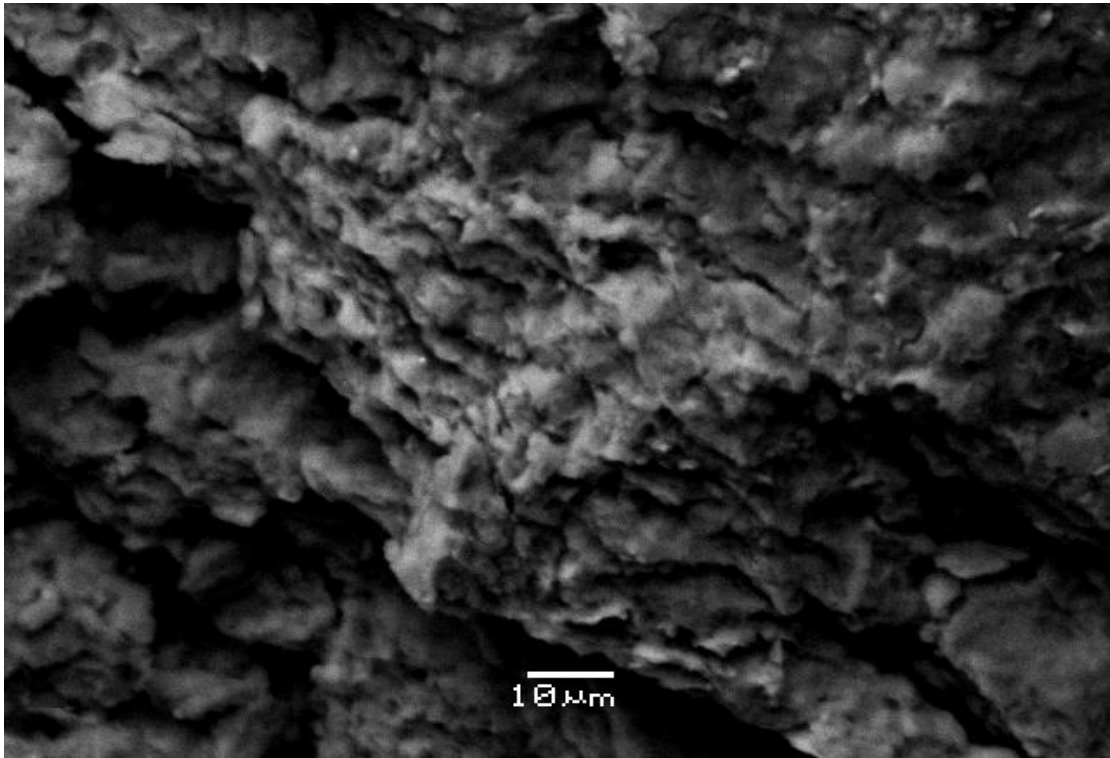


Figure 17. SEM micrograph of the mixed Al-Si phase.

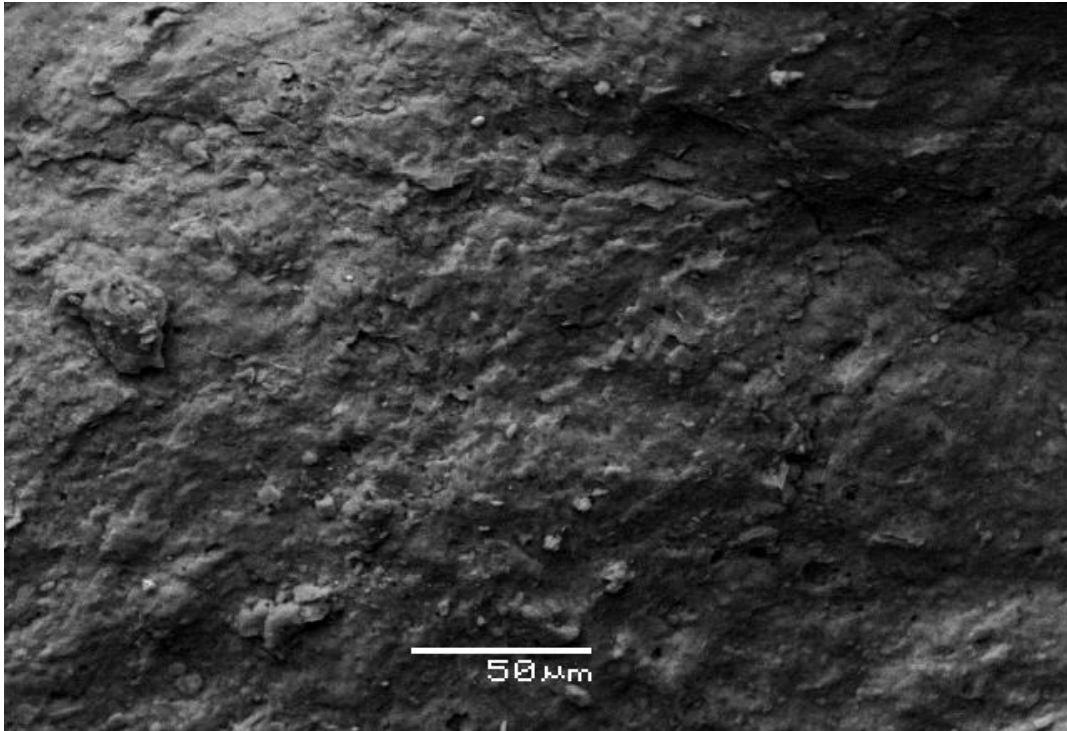


Figure 18. SEM micrograph of the mixed Al-Si phase.

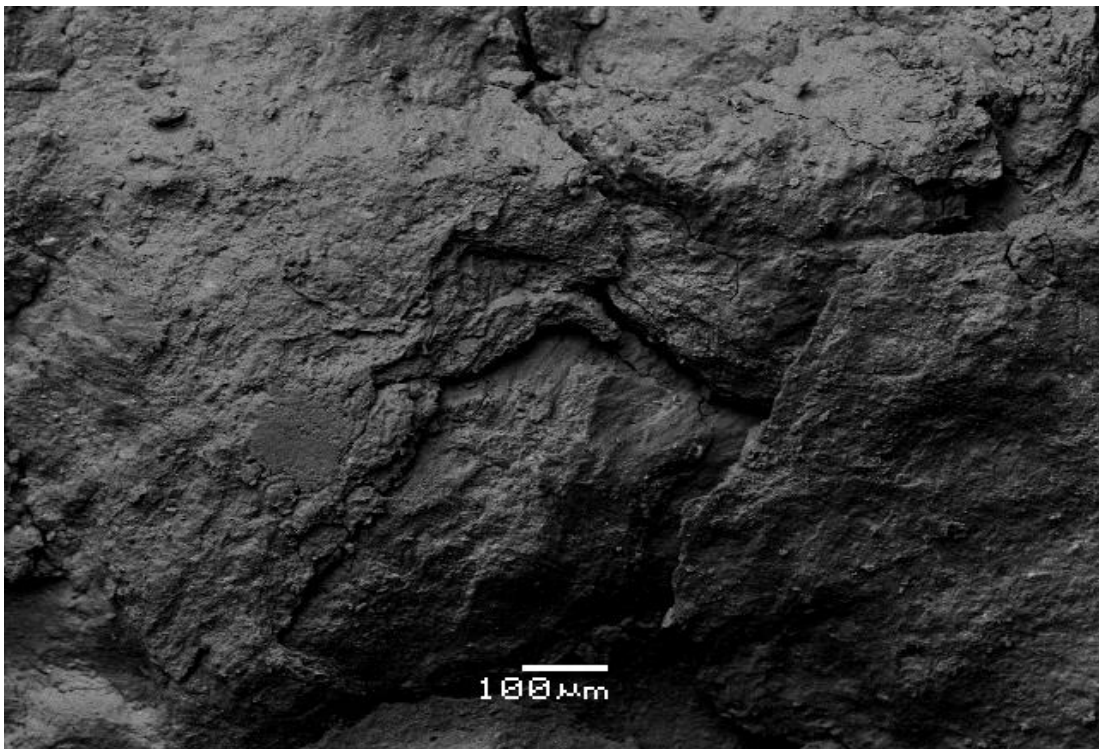


Figure 19. SEM micrograph of the mixed Al-Si phase.

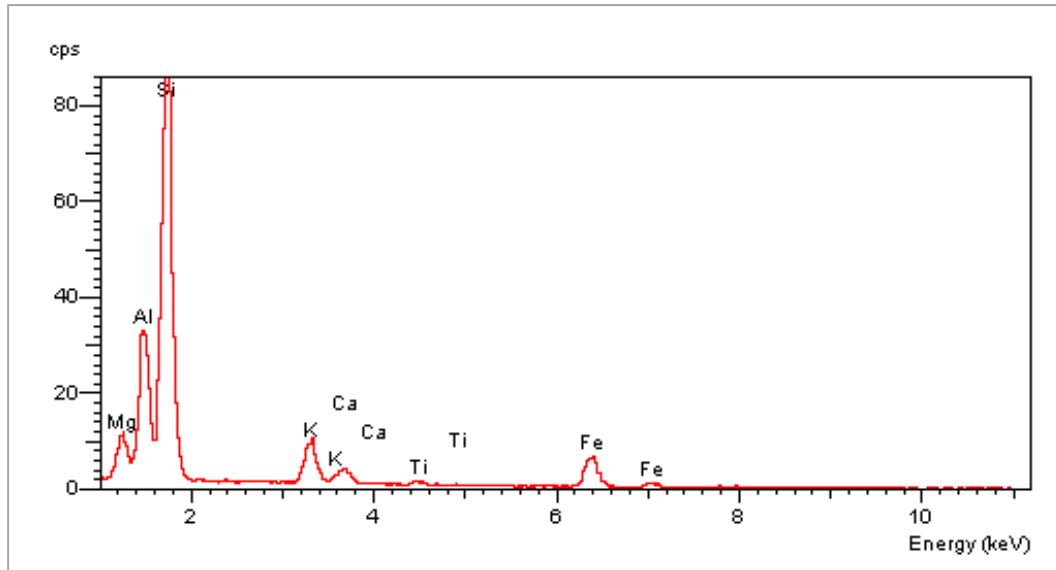


Figure 20. EDS analysis of the mixed Al-Si phase.

Furthermore, detailed SEM-EDS study on the Fe-clay stylolite material revealed the presence of apatite (Fig. 21-25) and of a TiO_2 authigenic mineral, probably rutile or anatase (Fig.26-29).

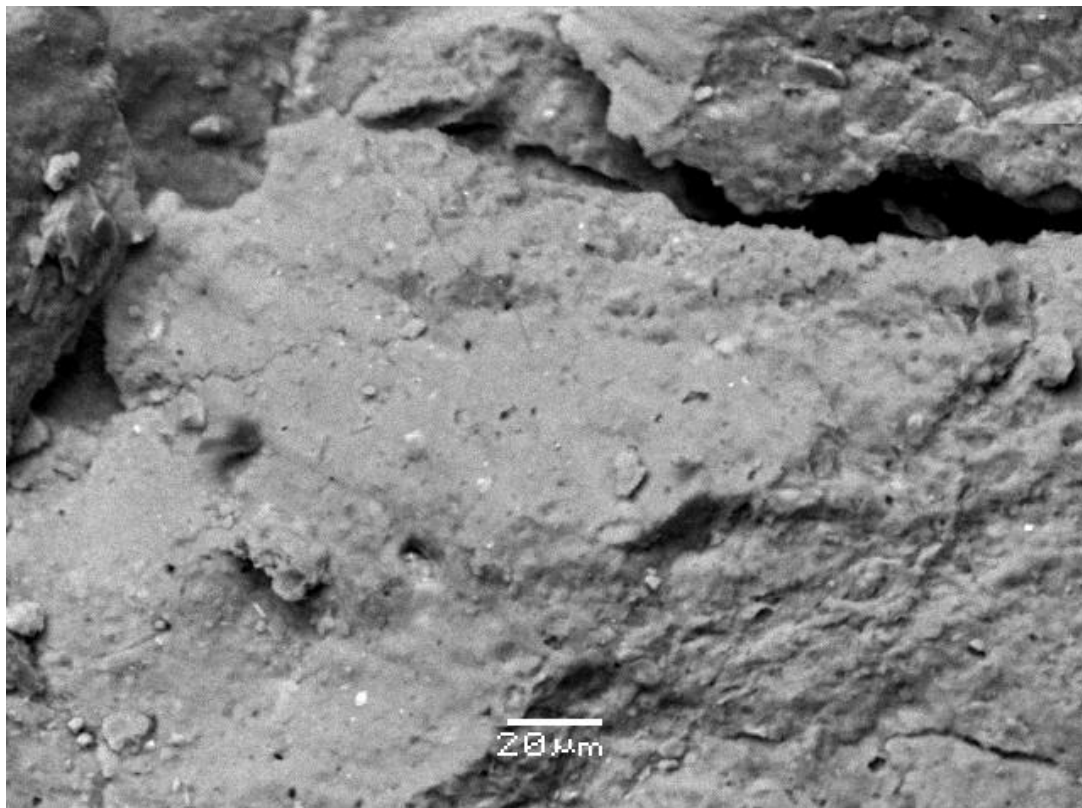


Figure 21. SEM micrograph of the stylolite sample. Presence of apatite.

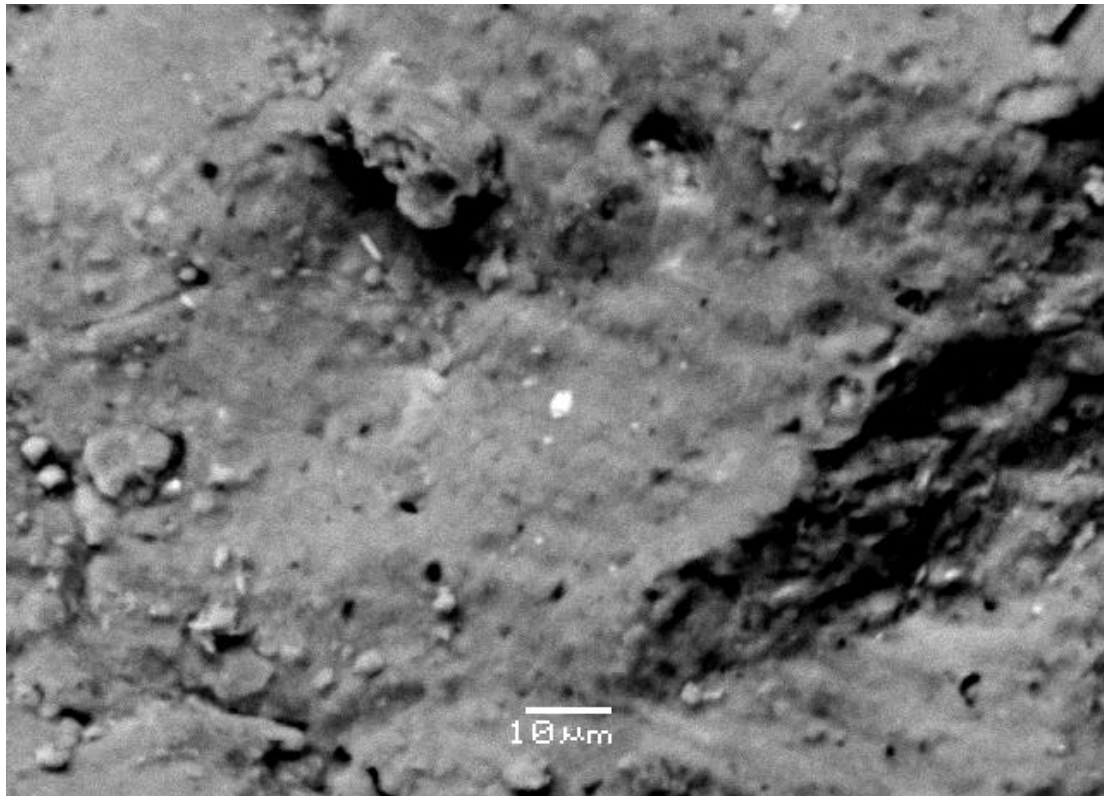


Figure 22. SEM micrograph of the stylolite sample. Presence of apatite.

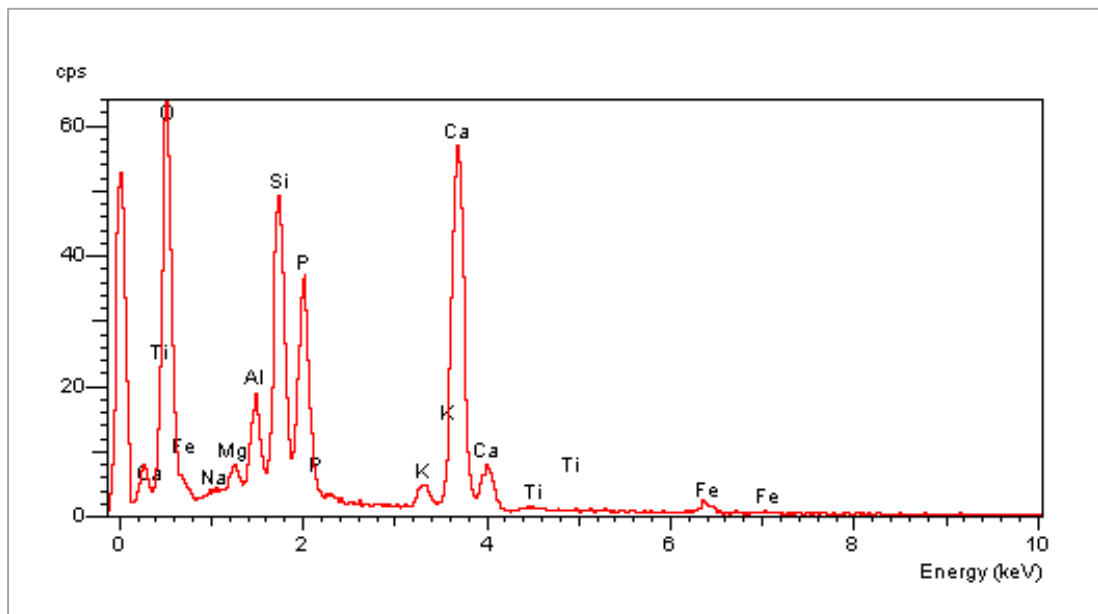


Figure 23. EDS analysis of the stylolite sample, where apatite was recognized.

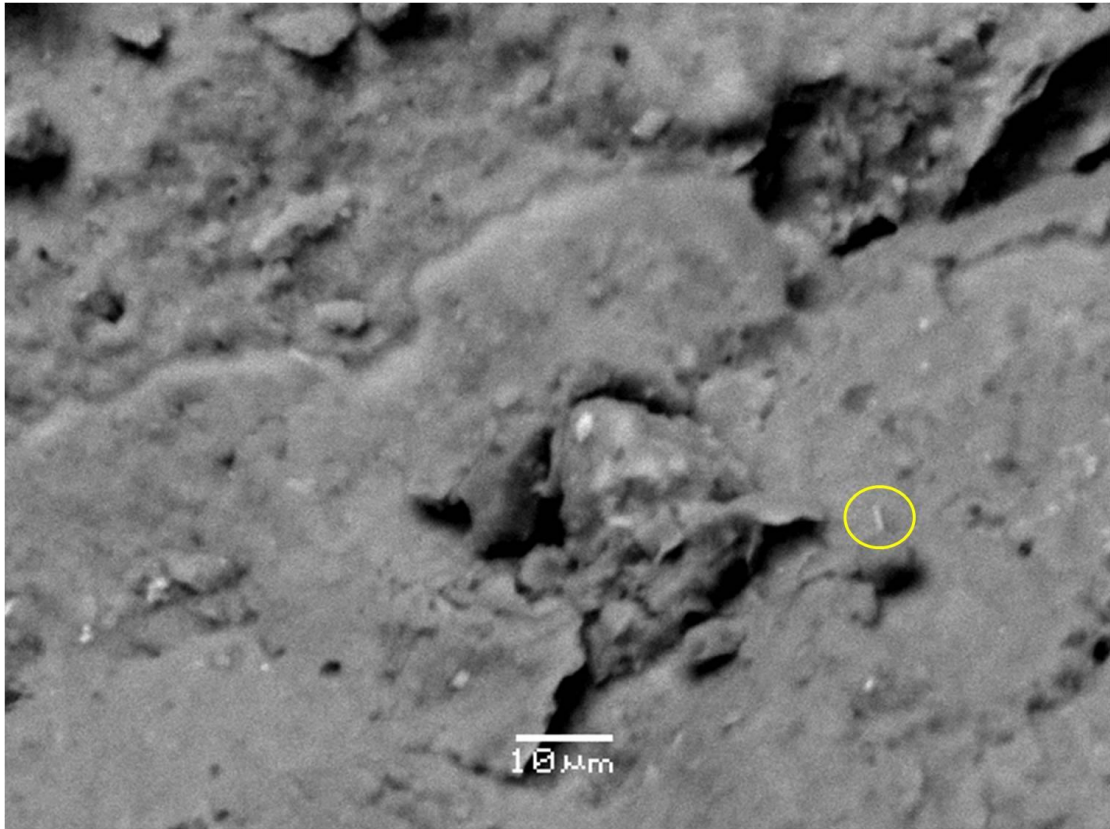


Figure 24. SEM micrograph of the stylolite sample. Presence of apatite. A rutile needle (2μm length) was also detected (yellow circle).

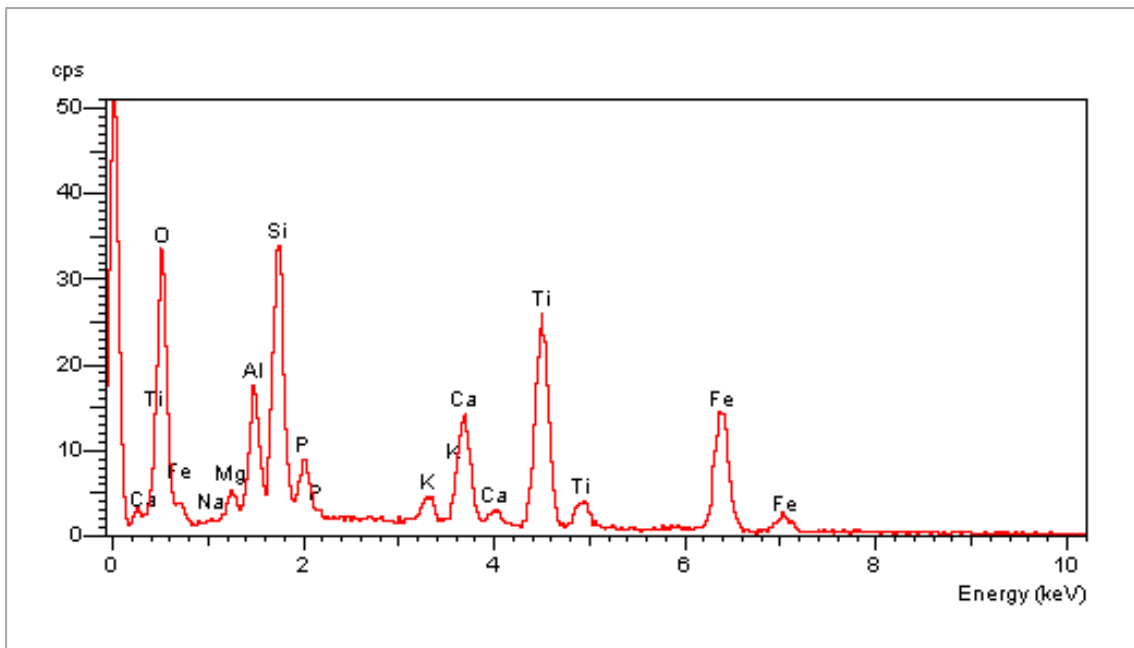


Figure 25. EDS analysis of the stylolite sample, where apatite was recognized.

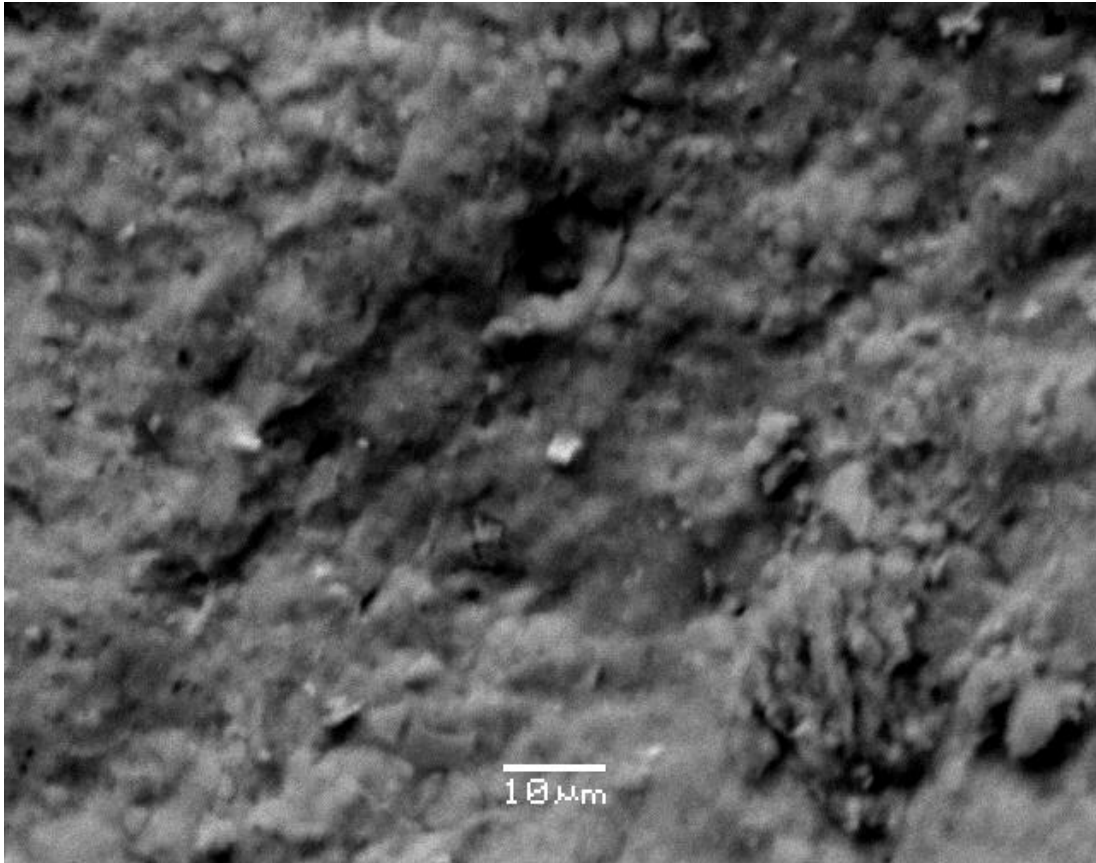


Figure 26. SEM micrograph of the stylolite sample. Presence of TiO_2 authigenic mineral, probably rutile or anatase.

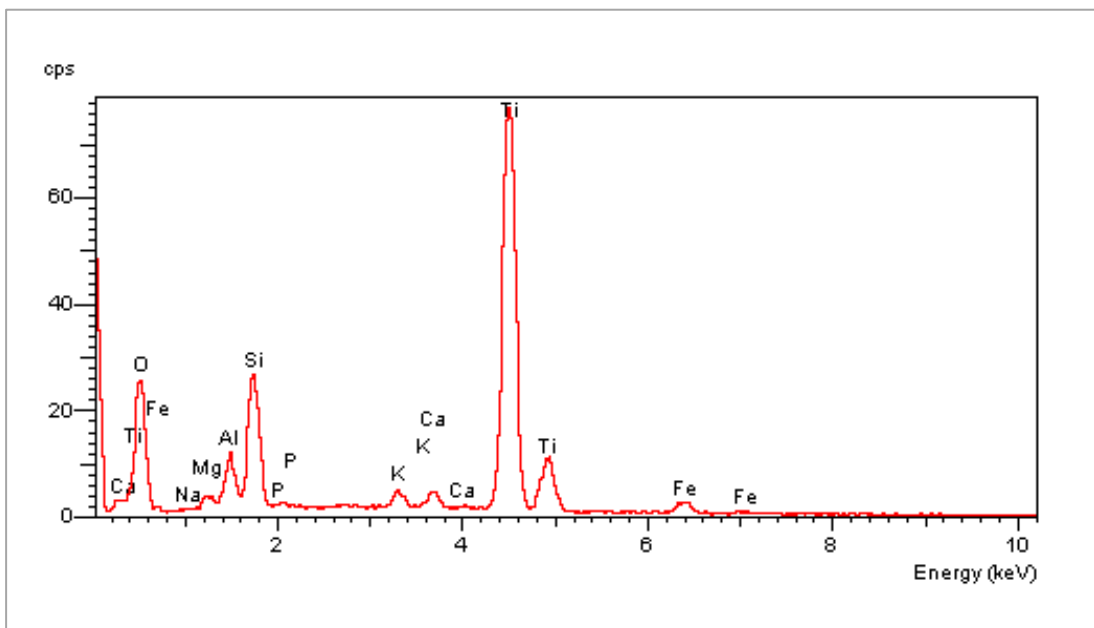


Figure 27. EDS analysis of the stylolite sample, with the presence of TiO_2 authigenic mineral, probably rutile or anatase.

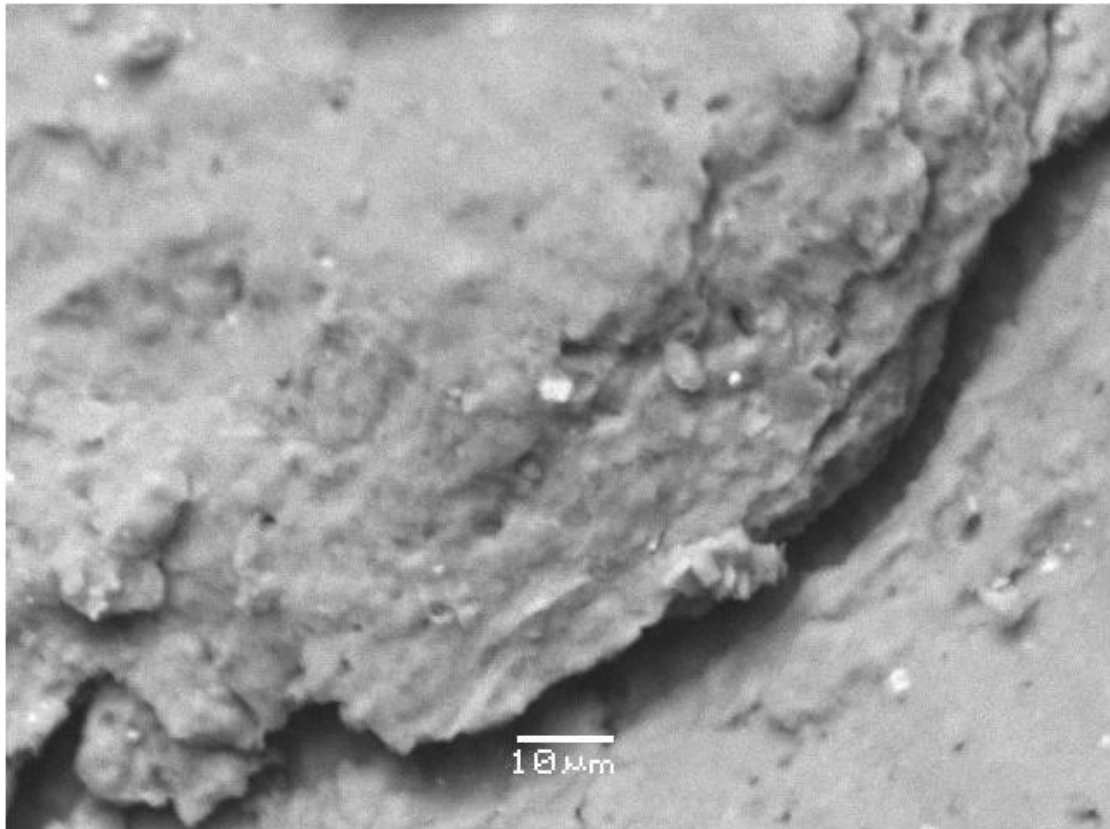


Figure 28. SEM micrograph of the stylolite sample. Presence of TiO_2 authigenic mineral, probably rutile or anatase.

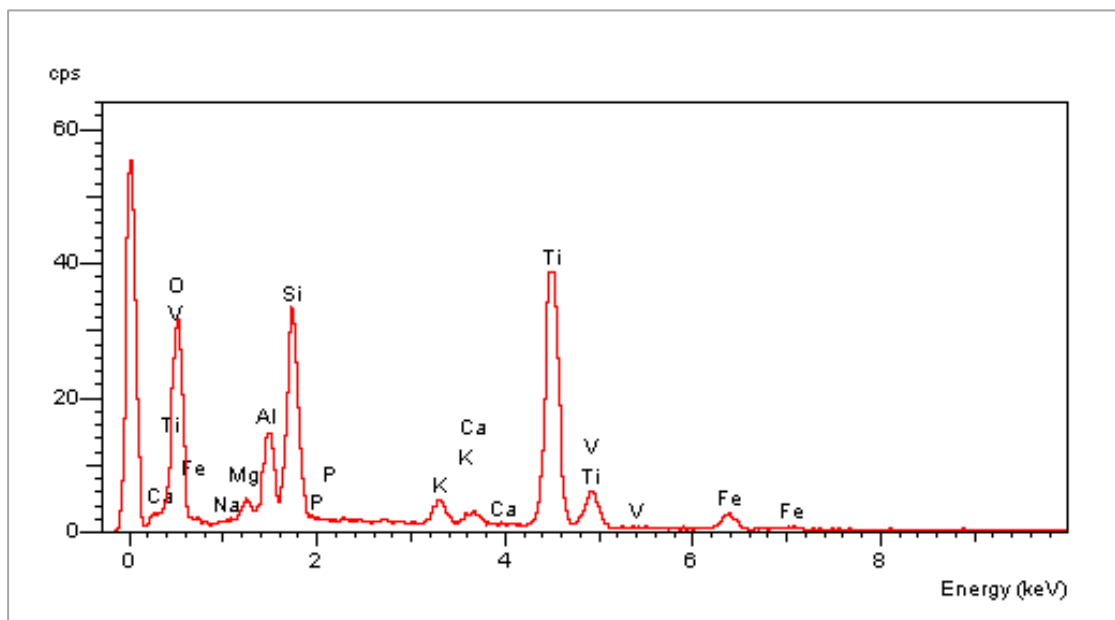


Figure 29. EDS analysis of the stylolite sample, with the presence of TiO_2 authigenic mineral, probably rutile or anatase.

3.2. Geochemistry

The bulk chemical composition of the studied stylolite material, the clay fracture of the same material and of the surrounding limestone from Epirus region has been yielded by means of ICP-ES/MS measurements. Analytical findings provide convincing evidence that all the illustrated elements can be accurately measured by this analytical technique. The bulk chemical composition of all the studied samples is presented in Table 3.

The UCC-normalized spider diagrams (Fig. 30) (Rudnick & Gao 2003), regarding the surrounding limestone sample, have indicated a clear depletion in almost every element, besides a small enrichment in Sr and a big enrichment in Se. The coprecipitation of Sr with calcite and aragonite has been extensively studied because of the potential applicability of experimental results to geothermometry, diagenetic conditions and processes, and the usefulness of strontium isotopes in understanding subsurface processes. SrCO_3 is isostructural with aragonite, although not with calcite, and Sr is generally the most abundant coprecipitate found in marine aragonites of both biogenic and inorganic origin (Katz et al. 1972, Morse & Mackenzie 1990). The Sr concentrations, in limestones consisting of calcite, indicate diagenetically altered limestones and highlight the complex behavior of carbonate minerals during diagenesis and the impact on the geochemical information of the primary and secondary phases.

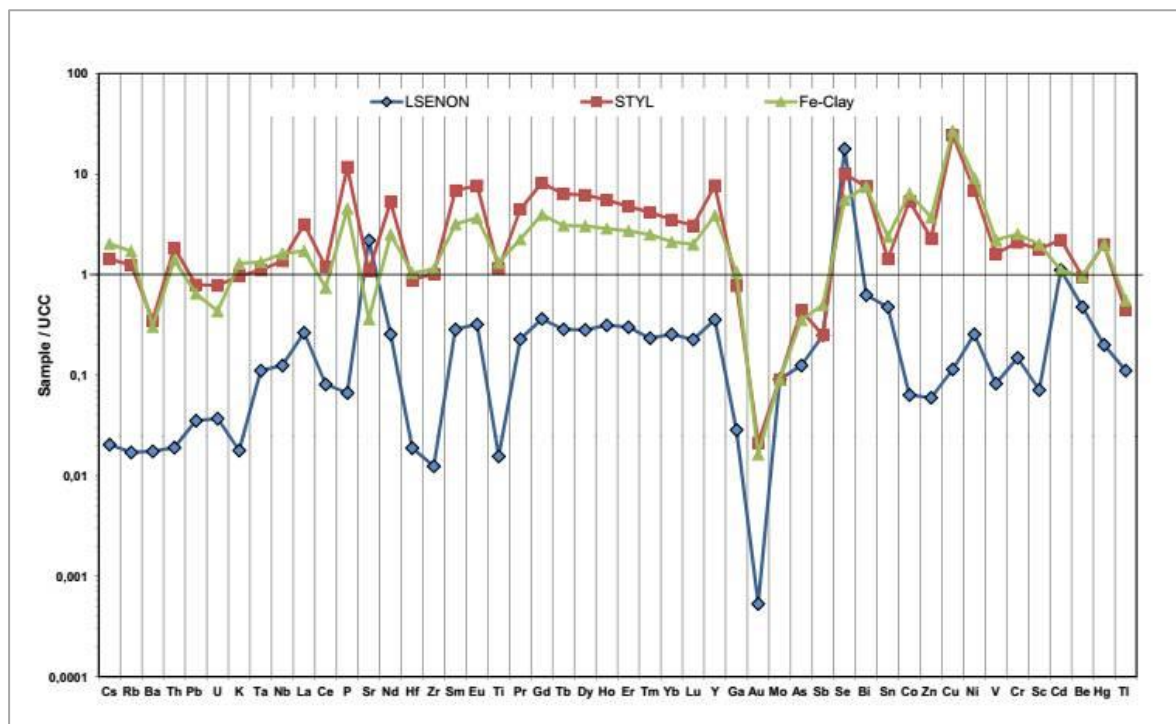


Figure 30. UCC-normalized spider diagrams for the studied samples.

Sample Code	LSENON	STYL	Fe-CLAY
Description	Surrounding limestone	Stylolite material	Clay fracture of whole stylolite material
<i>wt. %</i>			
SiO ₂	0.83	39.87	49.64
Al ₂ O ₃	0.2	11.91	16.67
Fe ₂ O ₃	0.1	4.6	6.35
MgO	0.23	2.99	4.1
CaO	55.19	15.37	2.3
Na ₂ O	<0.01	0.11	0.1
K ₂ O	0.05	2.7	3.62
TiO ₂	<0.01	0.73	0.84
P ₂ O ₅	0.01	1.77	0.68
MnO	0.03	0.04	0.04
Cr ₂ O ₃	<0.002	0.028	0.034
TOT/C	12.12	2.8	0.25
TOT/S	<0.02	0.04	0.02
LOI	43.2	19.5	N.A.
<i>ppm</i>			
Ba	11	221	191
Ni	<20	340	461
Sc	<1	25	28
Be	<1	2	2
Co	1.1	93.3	111
Cs	<0.1	7	9.9
Ga	<0.5	13.5	18.6
Hf	<0.1	4.7	5.5
Nb	1.5	16.4	19.4
Rb	1.4	102	140.1
Sn	<1	3	5
Sr	700.6	345.7	115.8
Ta	<0.1	1	1.2
Th	<0.2	19.3	14.8
U	<0.1	2.1	1.7
V	<8	157	214
W	0.8	8.5	12.4
Zr	2.4	196.6	216.9
Y	7.5	161.7	81.3
La	8.2	98.3	53.2
Ce	5.1	74.8	46.7
Pr	1.62	31.64	15.95
Nd	6.9	142.7	67.6
Sm	1.34	32.23	14.92
Eu	0.32	7.69	3.66
Gd	1.45	32.6	15.76
Tb	0.2	4.42	2.15
Dy	1.1	24.08	11.85

Table 3. Major and trace element concentrations in the studied samples.

The enrichment in Se, which was also observed in the non-carbonate samples, is mostly an enrichment noticed in shales, especially black shales (Bullock et al. 2017). The distribution of Se, as well as Te, in sedimentary environments is primarily a function of redox conditions, and may be transported and concentrated by the movement of reduced fluids through oxidized strata (Bullock et al. 2017). The Te depletion in all samples, combined with the Se enrichment, with respect to the continental crust, could imply a roll-front deposition (Bullock et al. 2017). Se enrichment in roll-fronts relates to the initial mobilization of trace elements in oxidized conditions, and later precipitation down gradient in reduced conditions (Bullock et al. 2017).

Both stylolite material and the Fe-clay, present similar chemical imprints, as shown in the UCC-normalized spider diagrams. The two samples have indicated a clear enrichment in chalcophile elements, such as Se, Zn and Cu, while only the bulk stylolite material shows enrichment in Cd. Resembling enrichment in chalcophile elements, regarding sedimentary rocks, is detected in black shales, which are an important reservoir of most chalcophile elements in the Earth's crust (Barnes 2016). Also, the bulk stylolite material is more enriched in High-Field Strength Elements (HFSE), than the Fe-clay, which could be attributed in the presence of apatite.

Depletion was observed in metalloids, for both non-carbonate samples, while there is a big enrichment in siderophile elements, such as Co and Ni. In sedimentary rocks, Ni is mostly held in detrital ferromagnesian silicate minerals, detrital primary Fe oxides, hydrous Fe and Mn oxides, and clay minerals. The levels of concentration in shale, sandstone and carbonate rocks may reach values as 68, 2 and 20mg kg⁻¹ respectively (Mielke 1979). Nickel also shows a distinct enrichment in diatomaceous ooze in certain contemporary basins, which suggests that the enrichment mechanism is either linked and involved with anoxic conditions, or that Ni is slightly enriched in a heavy-mineral fraction which accumulates in low-C, coarser grained sediments (François 1988). In the study of François (1988) in Saanich Inlet (British Columbia, Canada) sediments, there was no indication that Ni was scavenged from the water column since the Ni concentration found in the settling particulates at greater depths could easily be explained by the addition of aluminosilicates brought in by lateral advection. This suggests that the increase in Ni concentration found in the anoxic sediments of Saanich Inlet is the result of an addition of Ni via reactions occurring at the sediment-water interface, and not due to its direct association with planktonic organic matter.

In sedimentary rocks, Co tends to vary with the Fe and Mn content and is concentrated in the fine grained fractions. Arkose and greywacke are more enriched, their Co concentrations usually reflecting the abundance of mafic minerals (Ure & Berrow 1982). Cobalt is most mobile in the surface environment under acidic and reducing conditions, where the formation of high valency phases of Fe and Mn is inhibited. It is

rapidly removed from solution by co-precipitation and sorption in most oxidizing, near-neutral or alkaline stream water as the dissolved Fe and Mn precipitate out as secondary oxides, hydrous Mn oxides having a particularly strong sorption affinity for cobalt. Divalent cobalt (Co^{2+}) is bioaccessible when it is organically bound (McBride 1994), and cobalt may also bind to humic and fulvic acids and inorganic colloids (Qian et al. 1998). Certain bacteria are known to mobilise Co already complexed as chelate compounds (Kabata-Pendias & Pendias 2001). Measurements of cobalt in seawater suggest that cobalt is scavenged from the deep sea and hence follows biogeochemical pathways similar to manganese, other measurements of cobalt in pore waters of marine sediments showed that cobalt was released into pore waters in the sub-oxic sediment zone during dissolution of sedimentary manganese oxides (Heggie & Lewis 1984). According to Heggie & Lewis (1984) solid-phase cobalt concentrations in surface (oxic) sediments, above the pore water remobilization horizon, are almost double those measured in the deep (anoxic) sediment zone. The sediment and pore-water distributions indicate that a large fraction of sedimentary cobalt is recycled with manganese between oxic and sub-oxic pore waters and redeposited in surface (oxic) sediments (Heggie & Lewis 1984). In oligotrophic surface waters, Co concentrations are controlled by phytoplankton uptake and binding to organic ligands (Saito and Moffett 2001, 2002) rather than by the scavenging reactions with Mn that occur in coastal and deep waters (Moffett and Ho 1996). Cobalt concentrations in phytoplankton are similar to abundances of Cd and Cu and enriched by as much as 10x over Mo (Ho et al. 2003). Organic material can also sorb trace elements and transfer them to sediments (Broecker and Peng 1982; Krauskopf 1956), although this process is not as quantitatively significant for Co as it is for other metals (e.g., Cd, Zn; Algeo and Maynard 2004; Yee and Fein 2003). Deposition of phytoplankton biomass may also add Co to oxic sediments (Saito et al. 2004). Regardless of the pathway for authigenic Co delivery to sediments, Co released during early diagenesis is immobilized by scavenging with Fe(III) (oxyhydr)oxides and Mn(III/IV) oxides. Because higher Co availability is linked to periods in Earth's history when the oceans were anoxic, had on average lower Co burial rates, higher Co mobility, and probably longer Co residence times, environmental availability and catalytic suitability may both be reflected in the utilization of Co in organisms or proteins that evolved early (Swanner et al. 2014). Finally, marine cyanobacteria have an absolute requirement for Co that cannot be met by other metals (Saito et al. 2002; Sunda and Huntsman 1995), which again may reflect evolution in largely anoxic or sulfidic oceans with greater Co availability (Saito et al. 2003), yet thrive in the oxic oceans where Co concentrations are often less than 40 pM.

A comparison of the mean metal concentrations in the studied samples with the corresponding values of these metals in the average shale (Turekian and Wedepohl,

1961) (Fig. 31) reveals that there is enrichment in P, some REE, Se, Cu, Co, and Ni, while there is depletion in Mo and As.

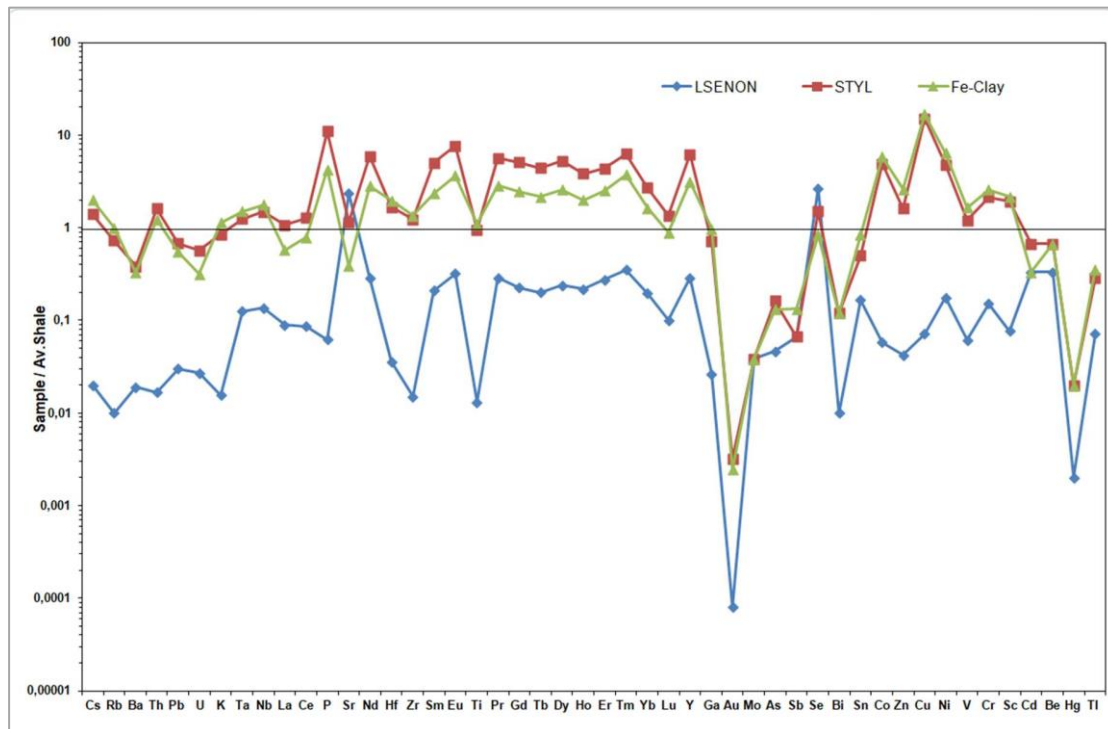


Figure 31. World average shale value (ASV)-normalized spider diagrams for the studied samples.

Th/Sc and Zr/Sc ratios are used to identify sediment recycling and sorting processes (McLennan et al, 1993, Rollinson 2014). Th/Sc monitors the compositional variation of the source, while higher Zr/Sc ratios are associated with zircon enrichments due to sedimentary recycling. Geochemically, Th/Sc and Zr/Sc ratios of non-carbonate samples (Fig. 32) indicate that they have not derived from any external source and are less affected by sedimentary recycling, as well as an authigenic provenance, since they coincide with pelagic clays.

The rare earth elements (REE), are a group of 14 elements that have similar crystal ionic radii and valance state. They have a decreasing crystal ionic radius from La (1.016 Å) to Lu (0.85 Å) and a single 3+ valence within the siliciclastic fraction of sediments and sedimentary rocks, which imposes limitations on their partitioning between different sediment fractions and the sources of those fractions, for example, between terrestrial-derived lithogenous debris and seawater-derived biogenous detritus and hydrogenous metal oxides. (Piper & Bau 2013). The REE of ancient sediments support their partitioning into these same fractions and further contribute to the identification of the redox geochemistry of the sea water in which the sediments accumulated (Piper & Bau 2013). Differences in the behavior of the individual REE in seawater are recorded by differences in the REE curves of the various seawater-derived fractions of marine sediments, i.e., the marine hydrogenous and biogenous sediment fractions

versus the terrestrial-derived lithogenous fraction (Goldberg 1963). On account of the complexation of the 3^+ REE in seawater (Byrne & Kim 1990, Byrne 2002) and the oxidation of Ce^{3+} to the $4+$ valence (Sholkovitz & Schneider 1991, Piepgras & Jacobsen 1992, Goldberg et al. 1963, Elderfield 1988), the REE curves of different marine sediment fractions might be expected to reflect the alkalinity and redox potential of the seawater from which they accumulated.

The non-carbonate studied samples contain rather significant amounts of REE, in comparison to the surrounding limestone sample. In the surrounding limestone sample $\Sigma LREE$, $\Sigma HREE$ and ΣREE reach the values of 23.16ppm, 4.67ppm and 27.83ppm respectively. While, in the bulk stylolite sample $\Sigma LREE$, $\Sigma HREE$ and ΣREE reach the values of 379.67ppm, 93.52ppm and 473.19ppm respectively and in the case of the Fe-clay sample 198.37ppm, 47.65ppm and 246.02ppm respectively (Table 4).

It is worth noting that the $\Sigma LREE$, $\Sigma HREE$ and ΣREE values of the bulk stylolite sample, are really close to Terra rossa respective values (Godelitsas et al., personal communication, May 7, 2019) ($\Sigma LREE$: 388ppm, $\Sigma HREE$: 66 and ΣREE : 454ppm)

Chondrite has been used for normalization of REEs (Fig. 33) (Haskin et al. 1968) because a bulk composition of the earth is assumed to be close to that of chondrite meteorites, which represent the primordial earth (Ohde & Mataragio 1999). The use of this method eliminates the abundance variation between REEs of odd and even atomic number, and allows determination of the extent of fractionation between the REEs, because such fractionation is not considered to have taken place during a meteorite's formation (White 2013).

REEs typically exist in a trivalent oxidation state, but Ce and Eu are unique in that they can also exist in tetravalent and divalent oxidation states, respectively, giving rise to their anomalous behaviors. Both are very important elements providing some constraints on paleocean chemistry. Cerium is the only REE with redox transformations at ambient oceanic conditions (Goldberg et al. 1963, Elderfield 1988; Sholkovitz & Elderfield 1988), so the Ce anomaly in ancient submarine sediments is one of the most useful indicators to monitor oceanic redox conditions. The Ce anomaly of seawater corresponds well to varying redox conditions (De Baar et al. 1988, German & Elderfield 1989; Sholkovitz & Schneider 1991) owing to rapid reduction or oxidation reactions between Ce^{3+} and Ce^{4+} in response to changes in the redox conditions (Sholkovitz et al. 1992) (Fig. 34).

Variations in redox conditions as well as differences in REE complexation and adsorption behavior are reflected by changes in the oxidation state of cerium Ce^{3+} - Ce^{4+} and Eu^{2+} - Eu^{3+} . These changes may result in differences in Ce and Eu abundances. Ce-anomaly (Ce/Ce^*) and Eu-anomaly (Eu/Eu^*) values are calculated by $Ce/Ce^* = Ce_{NASC} / [0.5 * (La_{NASC} + Pr_{NASC})]$ and $Eu/Eu^* = \log[2 * Eu_{NASC} / (Sm_{NASC} + Gd_{NASC})]$ (Fig.

35) (Leybourne & Johannesson 2008). Ce/Ce* values less than 1.0, depletion in sediment Ce, suggest reductive dissolution of insoluble Ce⁴⁺ to soluble Ce³⁺. Negative Eu/Eu* values (i.e., depletion in Eu) reflect oxidation of Eu²⁺ to Eu³⁺ and loss of Eu from the sediments (Hannigan et al. 2010). The relation between Ce/Ce* and Eu/Eu* anomalies approaches that of a binary mixing and could be interpreted as evidence of competitive processes whereby Eu/Eu* is responding to salinity and Ce/Ce* is responding to slight changes in oxidation as well as physical mixing and particle settling (Hannigan et al. 2010). The majority of marine sediments have negative Eu/Eu* except under hydrothermal conditions (McLennan 1989, Erel & Stolper 1993). Negative Eu-anomalies are explained by the reductive remobilization of Eu²⁺ from the sediments to the surface waters leading to negative Eu-anomalies in the sediment (Elderfield & Sholkovitz 1987).

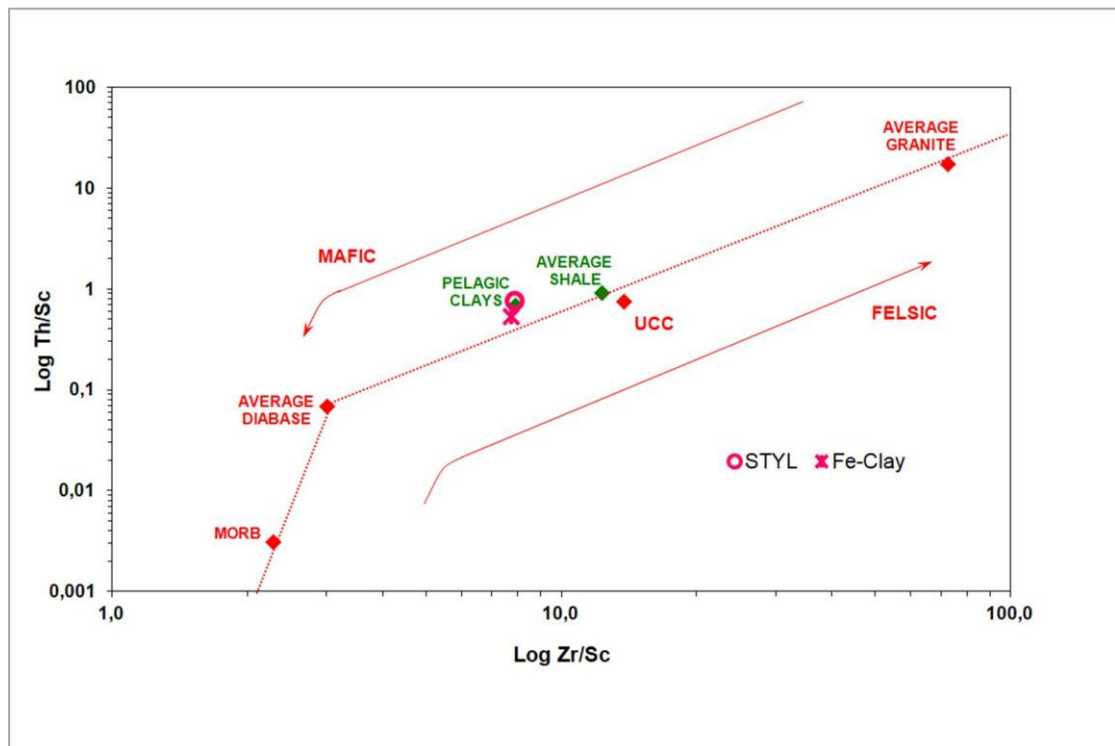


Figure 32. Th/Sc versus Zr/Sc diagram [after [McLennan et al 1993](#), [Rollinson 2014](#), [Li 1991](#) (Pelagic Clays), [Krauskopf & Bird 1994](#) (Shale)] for the non-carbonate studied samples.

Sample Code	LSENON	STYL	Fe-CLAY
Description	Surrounding limestone	Stylolite material	Clay fracture of whole stylolite material
ppm La	8.2	98.3	53.2

Ce	5.1	74.8	46.7
Pr	1.62	31.64	15.95
Nd	6.9	142.7	67.6
Sm	1.34	32.23	14.92
Eu	0.32	7.69	3.66
Gd	1.45	32.6	15.76
Tb	0.2	4.42	2.15
Dy	1.1	24.08	11.85
Ho	0.26	4.58	2.38
Er	0.69	10.94	6.26
Tm	0.07	1.25	0.75
Yb	0.51	7.01	4.22
Lu	0.07	0.95	0.62
Σ LREE	23.16	379.67	198.37
Σ HREE	4.67	93.52	47.65
Σ REE	27.83	473.19	246.02

Table 4. Rare-Earth Element (REE) concentrations in the studied samples.

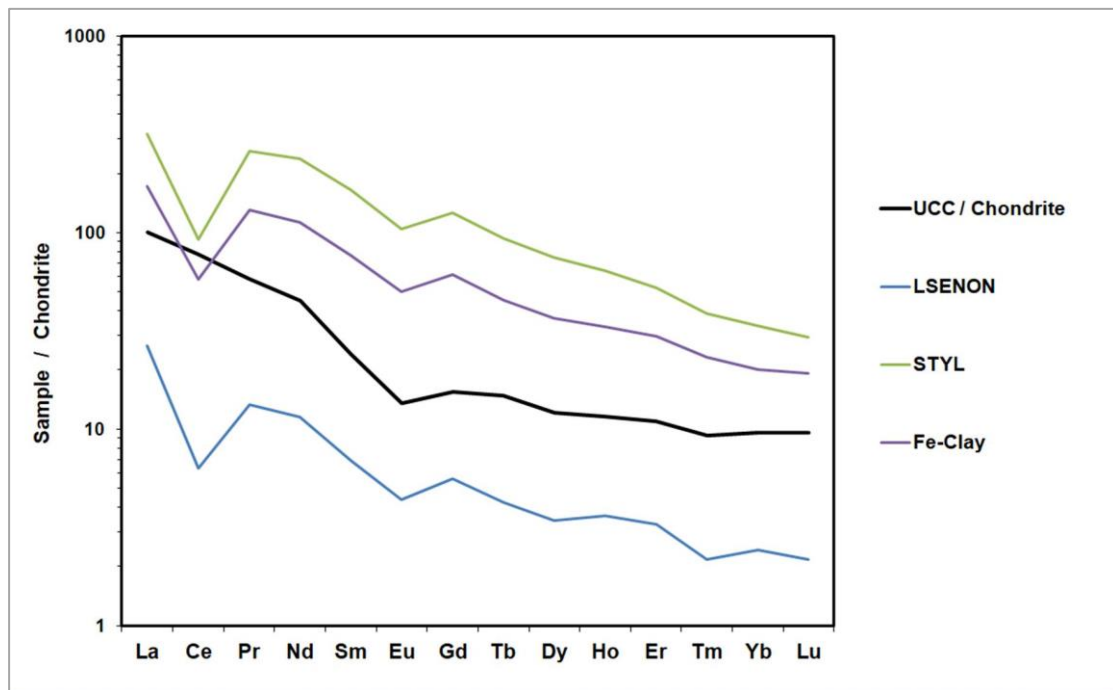


Figure 33. Chondrite-normalized diagram of the studied samples.

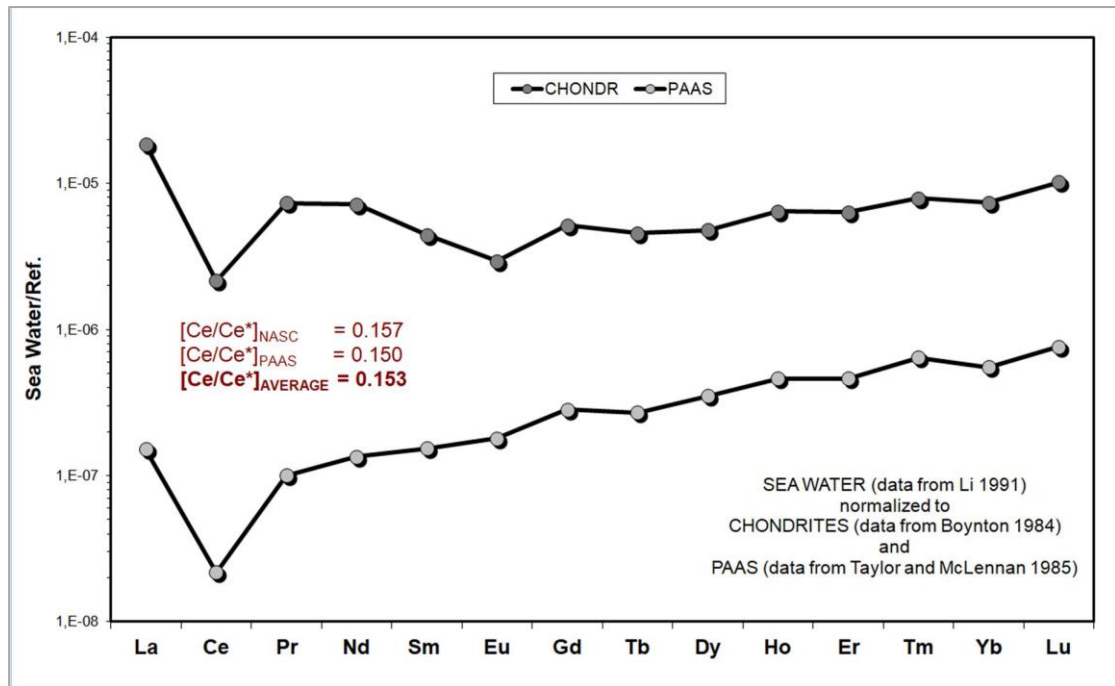


Figure 34. The Cerium anomaly of seawater.

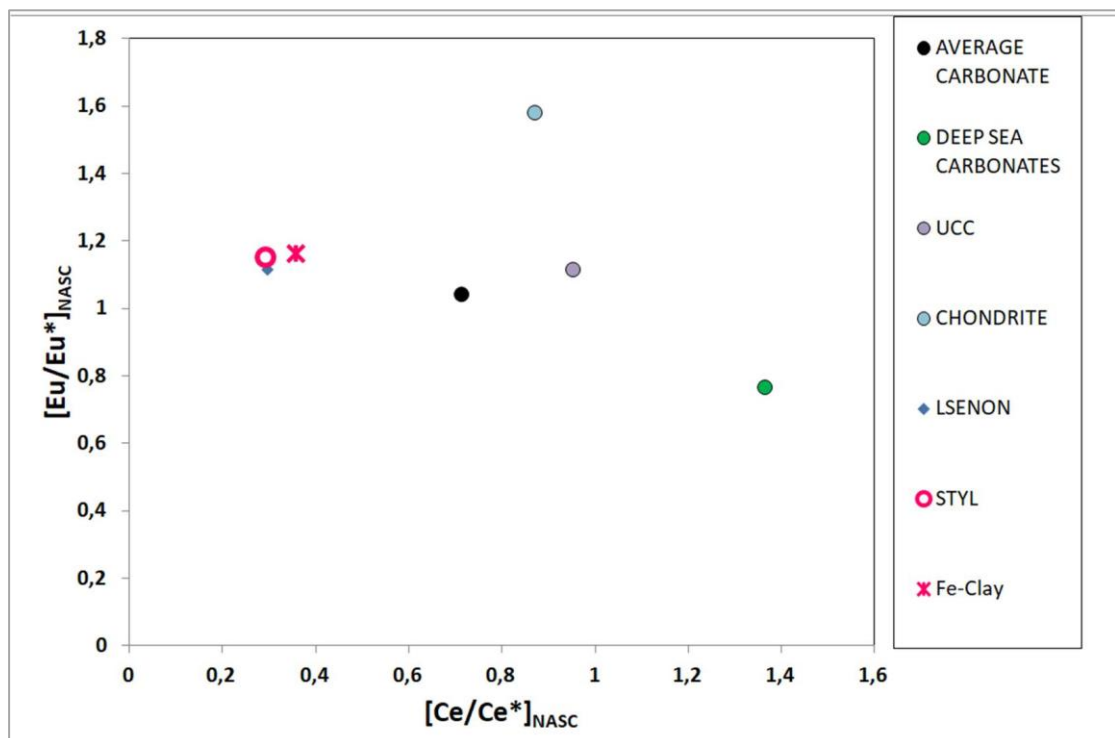


Figure 35. Eu/Eu* vs. Ce/Ce* discrimination diagram for the studied samples, in comparison with the values in respect of average carbonate, deep sea carbonates, UCC and Chondrite.

Comparing the Eu/Eu^* vs. Ce/Ce^* discrimination diagram of the samples of the current study, to that of the sedimentary Mesozoic (Dogger – L. Cretaceous) rocks from NW Greece (Epirus region) studied by Tzifas et al. (2014) (Fig. 36), it is evident that they have alike anomalies and Eu/Eu^* - Ce/Ce^* ratios, which could be attributed to similar variations in redox conditions in the Ionian basin, which could have lasted till Upper Cretaceous (current study's samples age).

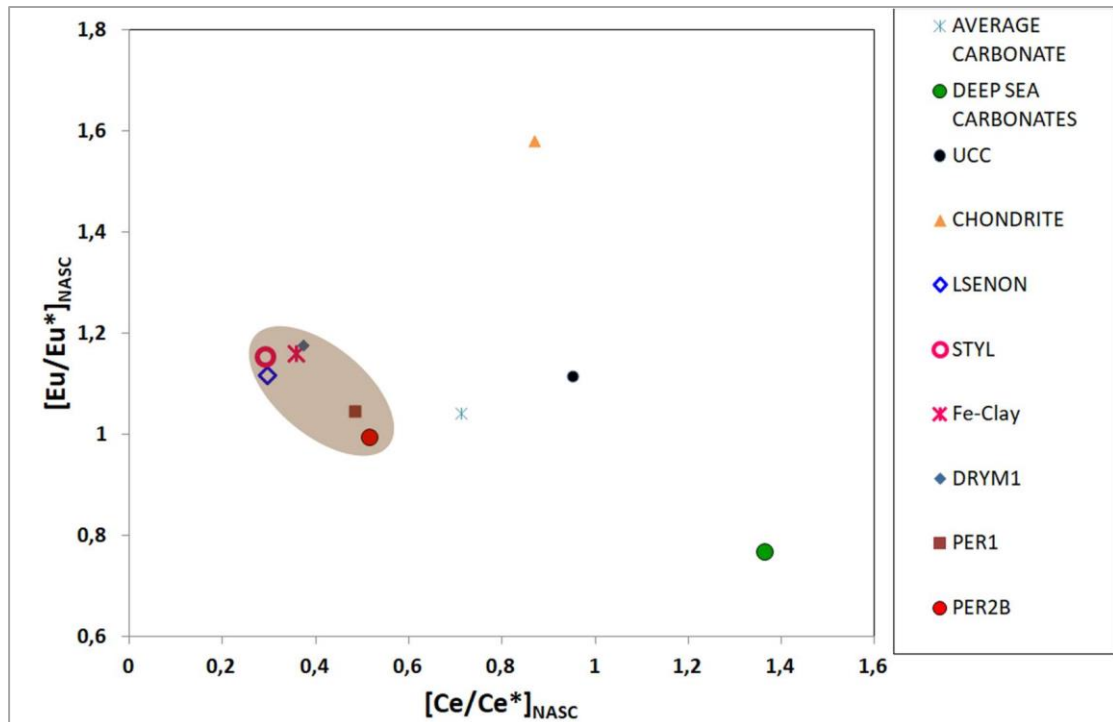


Figure 36. Eu/Eu^* vs. Ce/Ce^* discrimination diagram for the studied samples, in comparison with the values from Tzifas et al. (2014). DRYM1 (laminated phosphatized limestone), PER1 (bedded chert) and PER 2B (organic-rich part of the brecciated phosphatized limestones).

3.3. Fe-speciation

The redox chemistry of iron plays a major role in the geochemical cycling of many elements in freshwater and marine systems. Mössbauer spectroscopy is one of the few techniques which can quantify the proportions of Fe²⁺ and Fe³⁺ in both crystalline and amorphous materials and has been used in many studies of iron chemistry in sediments (Coey et al. 1974, Davison & Dickson 1984, Manning & Ash 1979, Nembrini et al. 1983, Readman et al. 1976, Hilton et al. 1986). Mössbauer spectroscopy has been used in mineralogical, petrological, and geochemical studies, and most of these applications concern the 14.4keV ⁵⁷Fe Mössbauer effect. Studies on silicate minerals have demonstrated the applicability of this technique to the investigation of the oxidation states and site population of iron and the identification of iron-bearing minerals. Mössbauer spectroscopy can also be applied to characterize more complicated geological materials, such as multiphase assemblages, for mineralogical identification, determination of the Fe³⁺ /Fe²⁺ ratio, and the semiquantitative analysis of iron distribution in each mineral and lattice site (Bancroft 1973).

Mössbauer spectroscopy results for the bulk stylolite material and Fe-clay are represented in Figures 37-38 and Table 5. Parameters of a two-doublet fit to the room temperature spectra of the bulk stylolite sample (Fig. 37) were a quadrupole splitting $\Delta E_Q = 0.56$ mm/s and an isomer shift $\delta = 0.35$ mm/s, and $\Delta E_Q = 2.70$ mm/s, $\delta = 1.11$ mm/s, in accord with Fe³⁺ and Fe²⁺ in octahedral coordination. In addition the 83% Fe³⁺ and 17% Fe²⁺ content suggests that the Fe-bearing clay minerals comprising the sample may be Fe-illites as well as montmorillonites, or mixed layer clays like illite-montmorillonite (Minai 1988, Murad & Wagner 1994, Drodt et al. 1998, Drits et al. 1997, Herber 2012).

Mössbauer Fitted Parameters						
Sample	T (K)	δ (mm/s)	ΔE_Q (mm/s)	FWHM, Γ (mm/s)	Area %	Fe valence
STYL	297	0.35	0.56		83	3+
		1.11	2.70		17	2+
Fe-CLAY	297	0.35	0.55	0.57	90	3+
		1.14	2.68	0.38	10	2+

Table 5. ⁵⁷Fe Mössbauer fitted parameters for the bulk stylolite and Fe-clay sample of the current study.

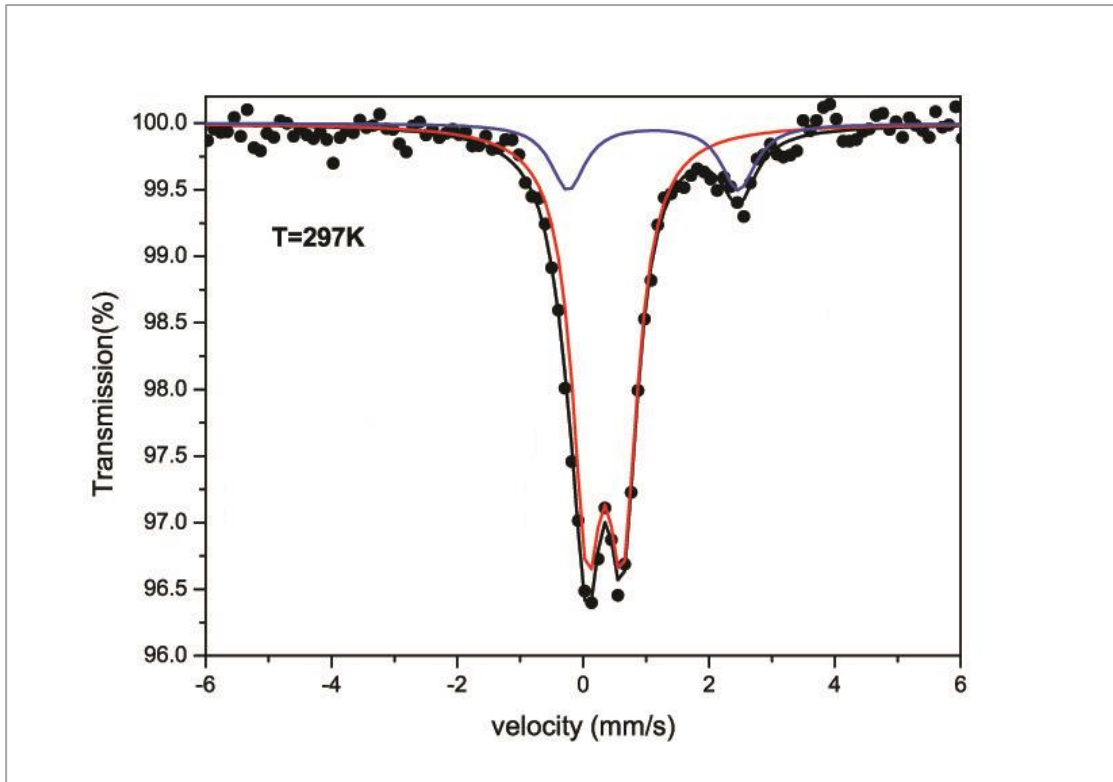


Figure 37. Mössbauer spectra of the bulk stylolite material measured at 297K (Fe^{3+} : red, Fe^{2+} : blue).

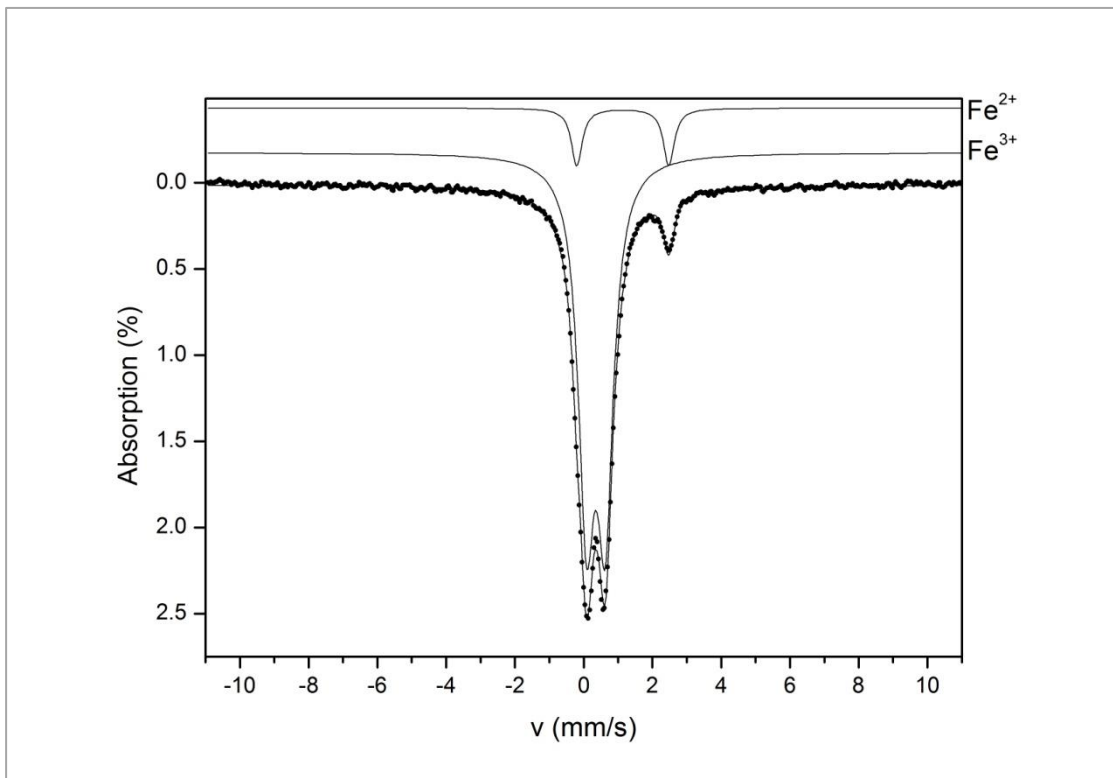


Figure 38. Mössbauer spectra of the clay fracture from the whole stylolite material measured at 297K.

Parameters of a two-doublet fit to the room temperature spectra of the clay fracture (<2 μ m) sample (Fig. 38) were a quadrupole splitting $\Delta E_Q = 0.55$ mm/s and an isomer shift $\delta = 0.35$ mm/s, and $\Delta E_Q = 2.68$ mm/s, $\delta = 1.14$ mm/s, in accord with Fe³⁺ and Fe²⁺ in octahedral coordination. In addition the 90% Fe³⁺ and 10% Fe²⁺ content suggests that the Fe-bearing clay minerals comprising the sample may be mostly Fe-illites, although a small portion of montmorillonites, or mixed layer clays like illite-montmorillonite, could not be rejected (Minai 1988, Murad & Wagner 1994, Drodt et al. 1998, Drits et al. 1997, Herber 2012).

3.4. Nanomineralogy

To go in detail in clay mineral distributions, transmission electron microscopy (TEM) experiments were performed on the Fe-clay sample. Similar to X-ray imaging technique, transmission electron microscopy (TEM) uses electron beams instead of X-rays (Fig. 39).

The sample shows thickness distributions characterized by a positive skew, with modes smaller than the mean values. The mean values are almost identical in all cases (16-17 nm), and most of the values are around 6-11 nm (Fig. 39B-43, 45B). These distributions are typical of a late diagenesis grade (Merriman & Peacor 1999), which is usually reached during burial diagenesis. It has been noted that clay packets show high density of high high-angle boundaries (Fig. 40A,43B), areas with packets parallel to sub-parallel to each other and packets with variable contrast as a consequence of variable- layer orientation and curved morphologies. Significant amount of small nanopores (<5 nm) were found in the Fe-clay sample (Fig. 41, 44-46), which were identified as intraparticle pores, according to the classification designed by Loucks et al. (2009). High magnification transmission electron microscopy images show the morphology of the intraparticle nanopores, the shapes of which trend to be irregular ellipsoidal or unrounded. Interparticle pores were, also, observed, some of which associated with clay sheets.

TEM images along with spectrum diagrams and element distribution tables are presented in Figures 47-60.

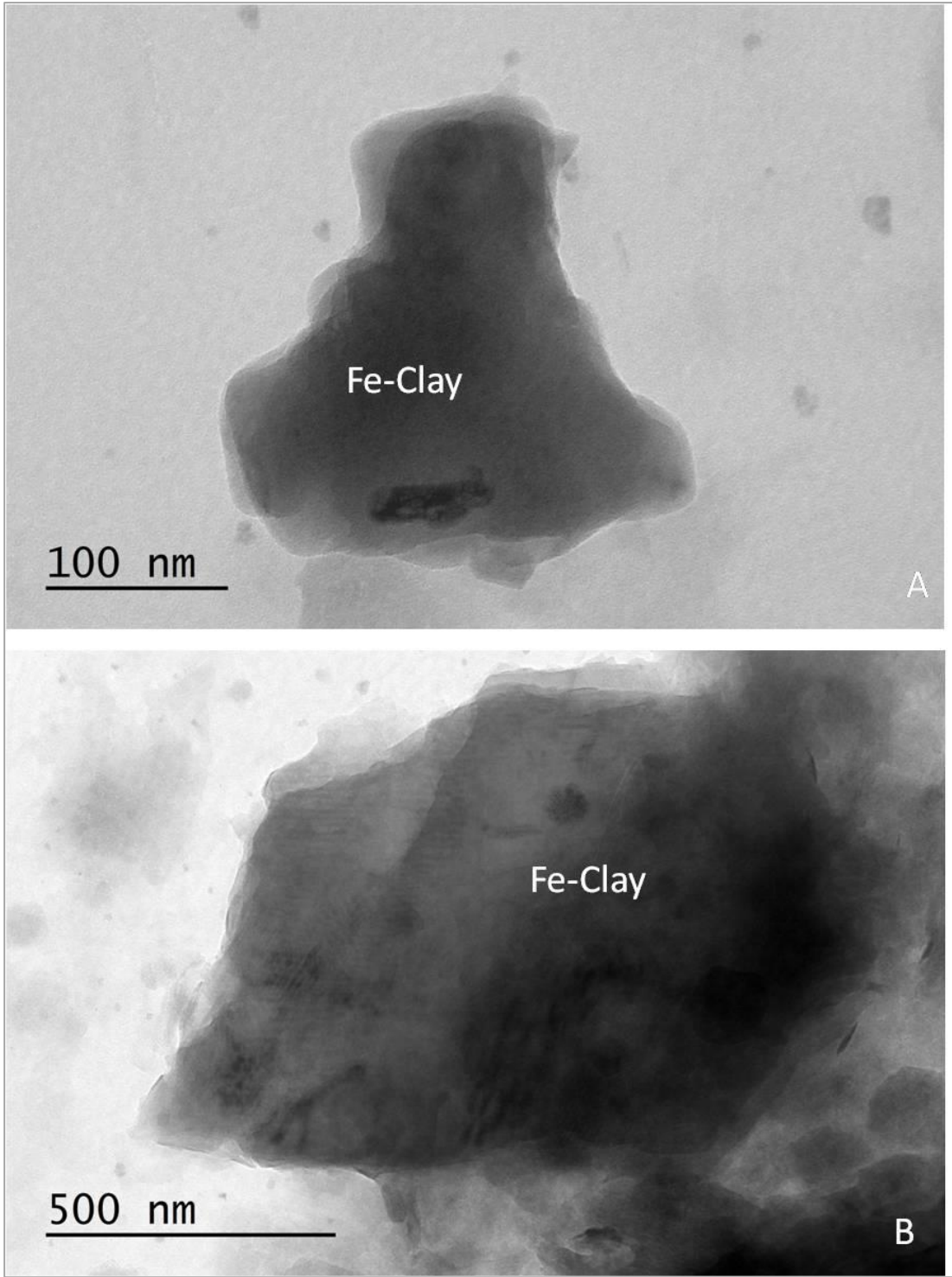


Figure 39. TEM Images of Fe-clay sample.

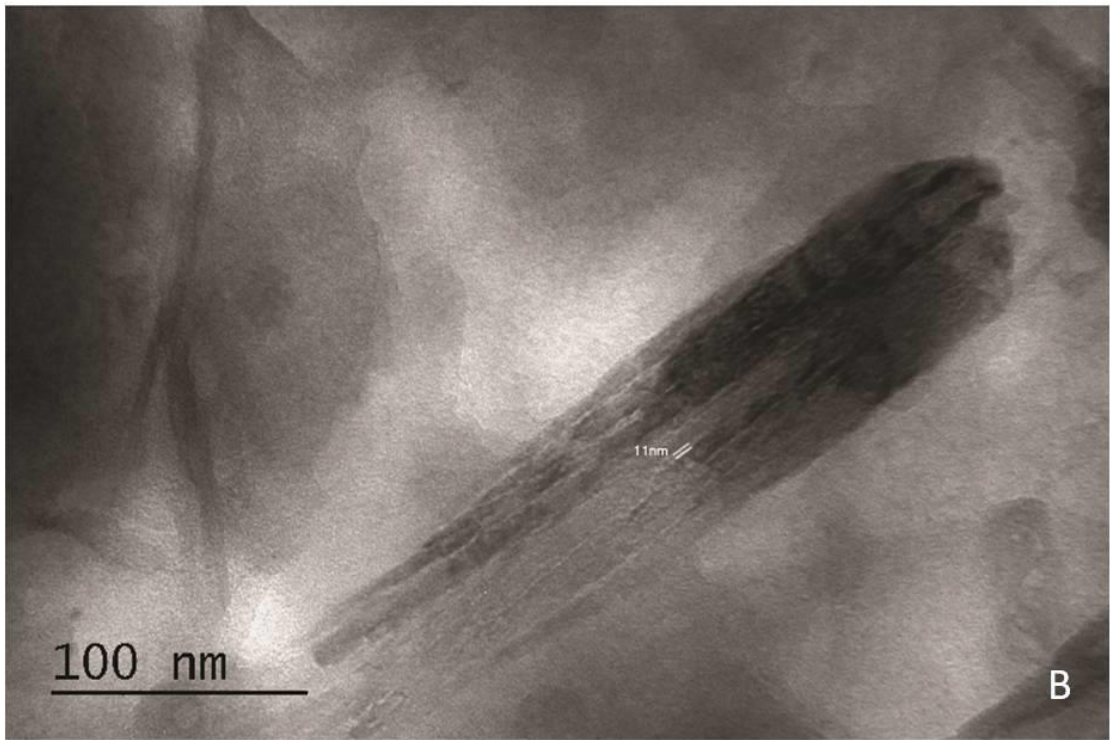
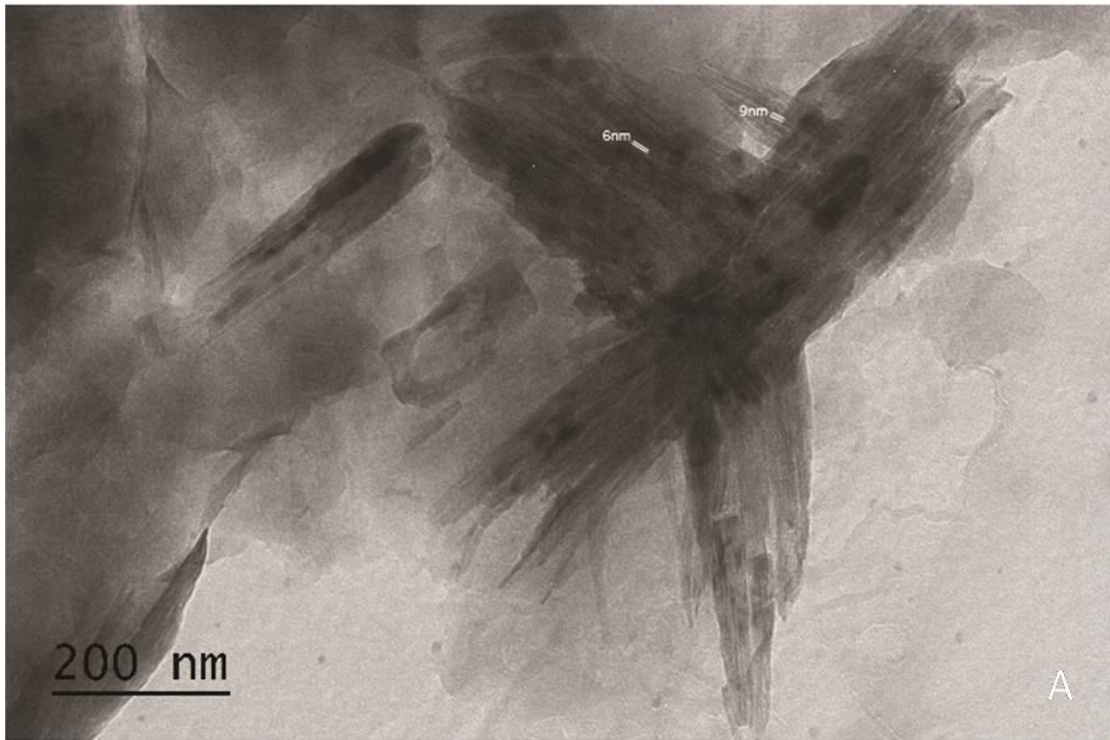


Figure 40. TEM Images of Fe-clay sample.

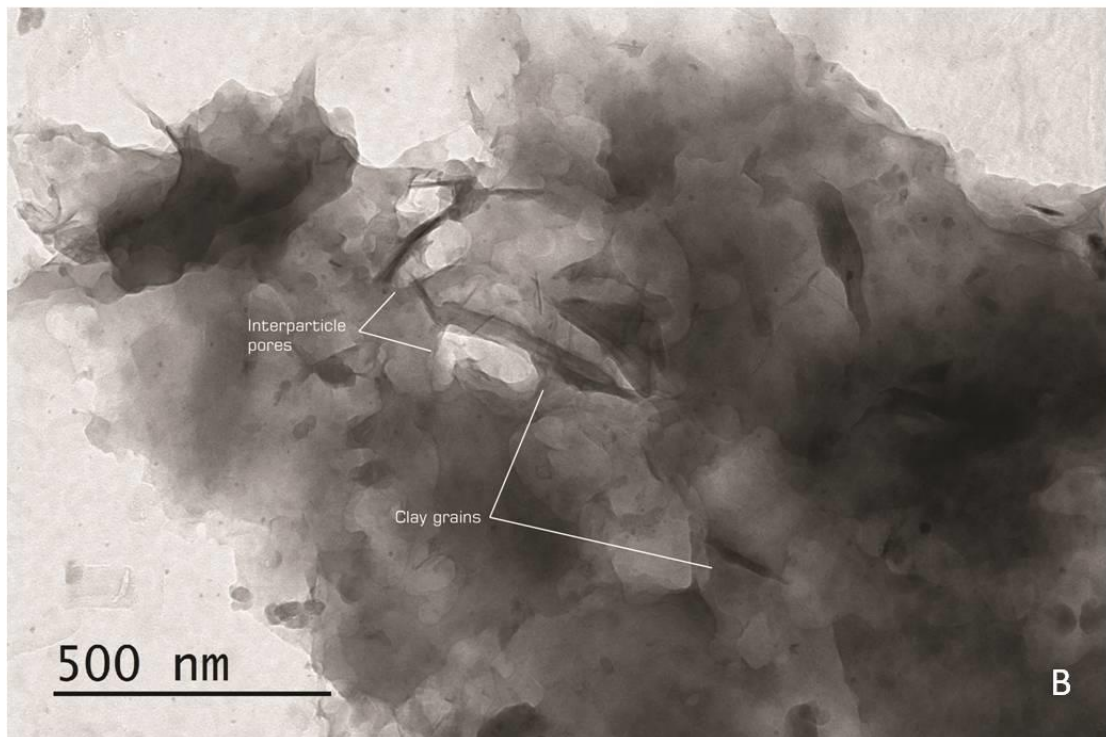
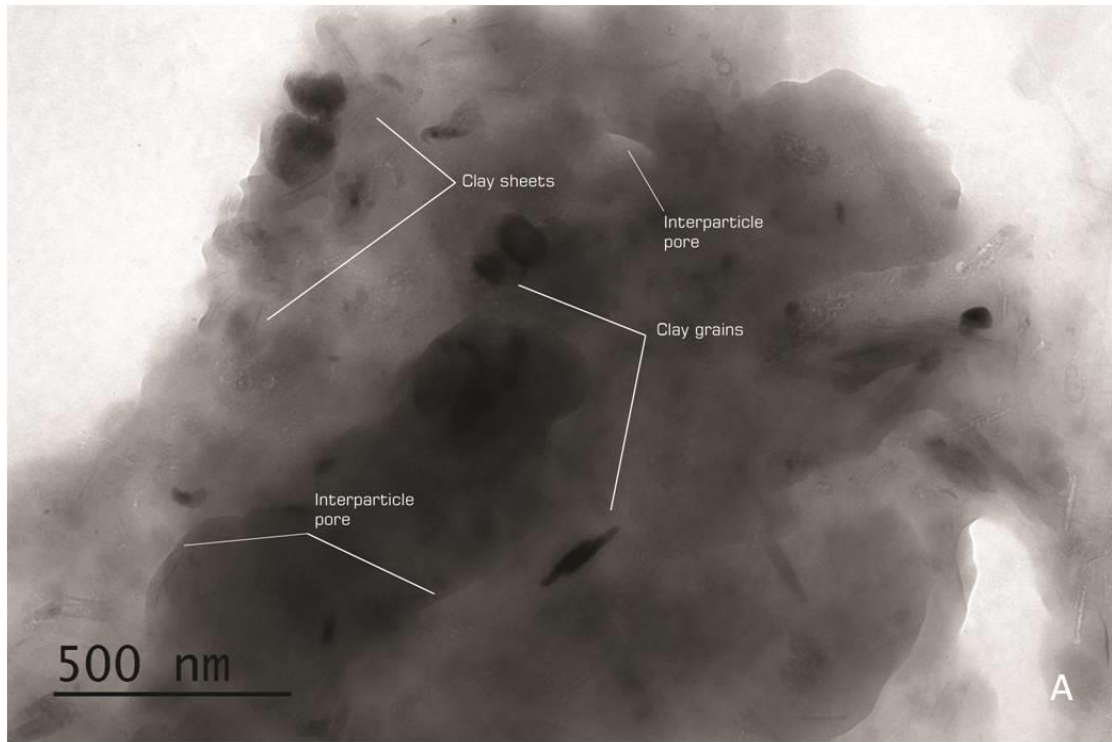


Figure 41. TEM Images of Fe-clay sample.

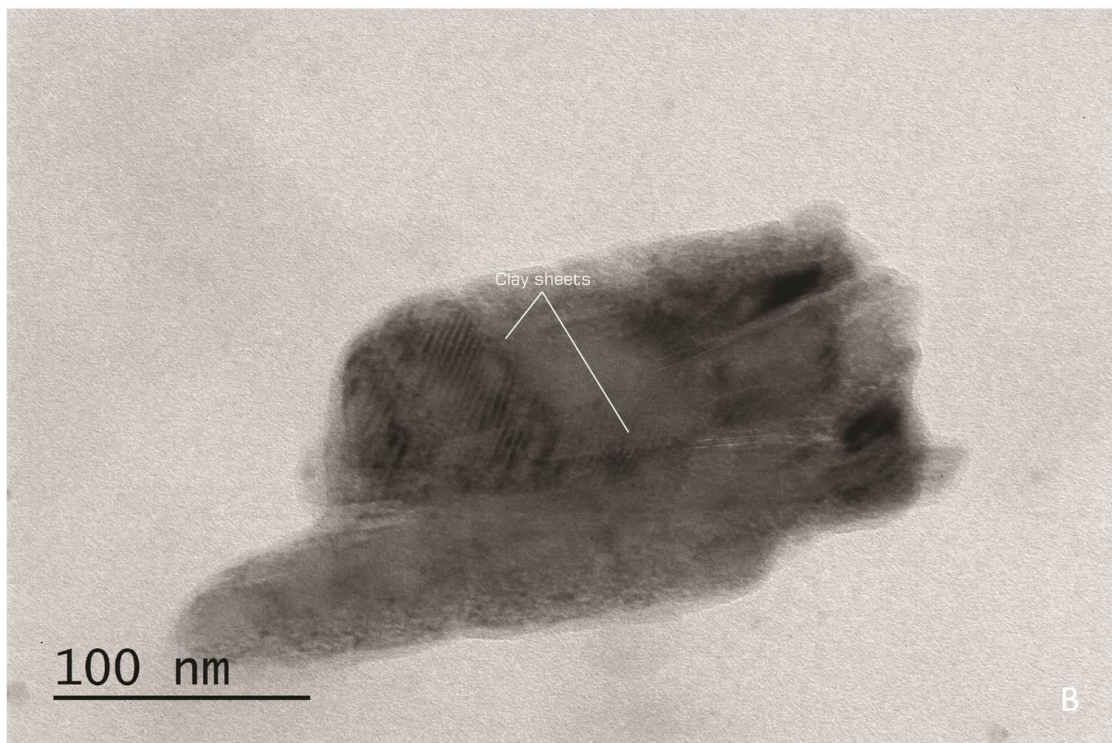
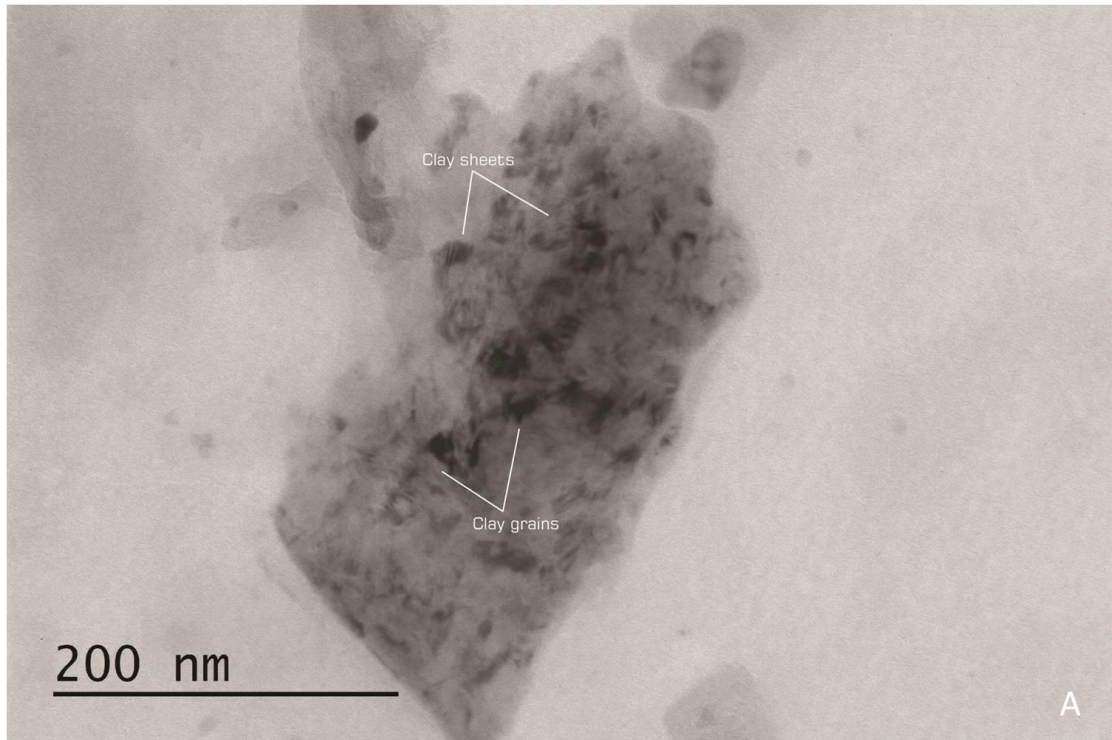


Figure 41. TEM Images of Fe-clay sample.

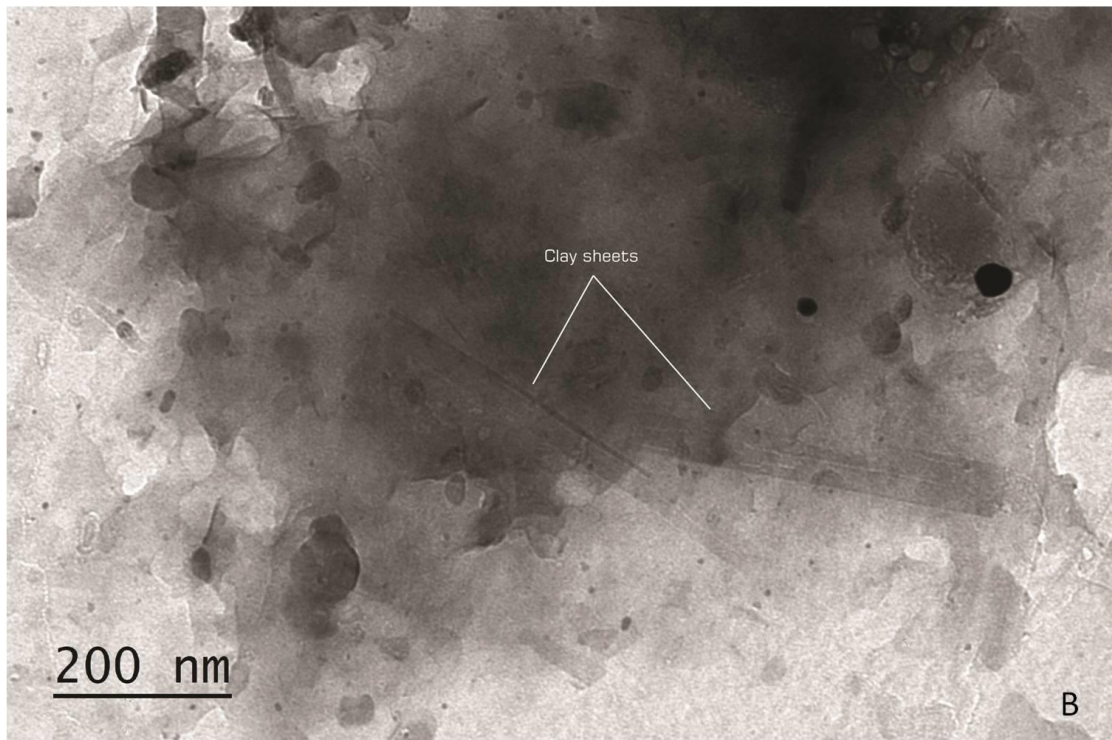
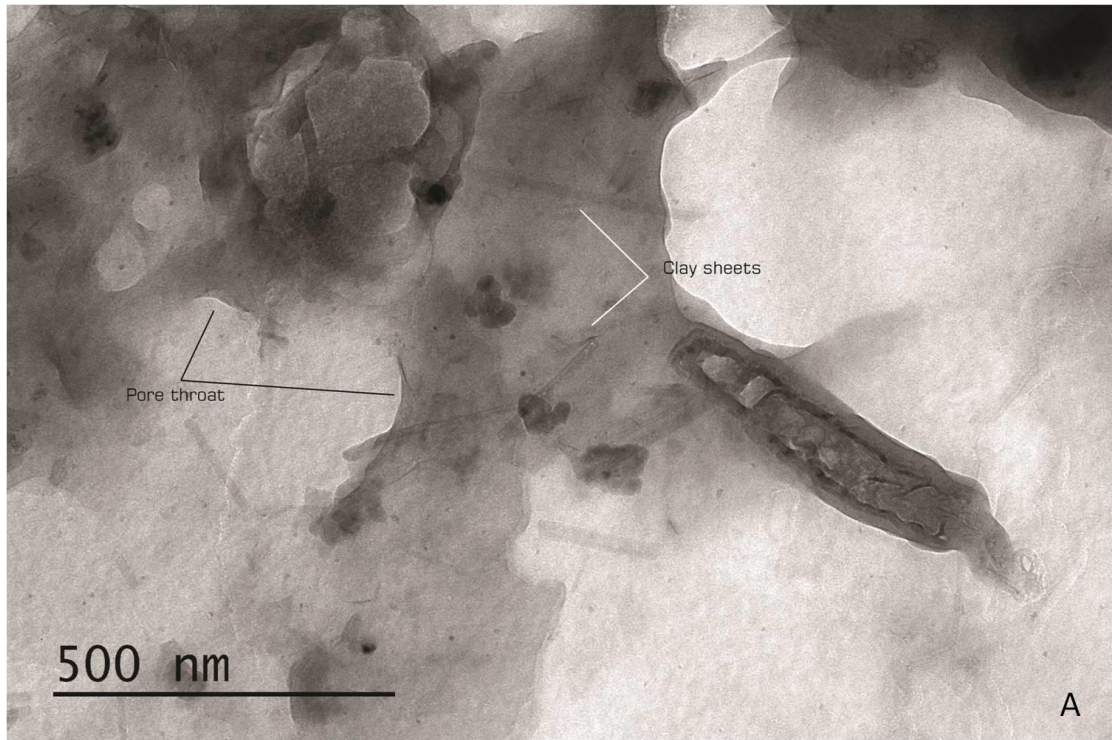


Figure 42. TEM Images of Fe-clay sample.

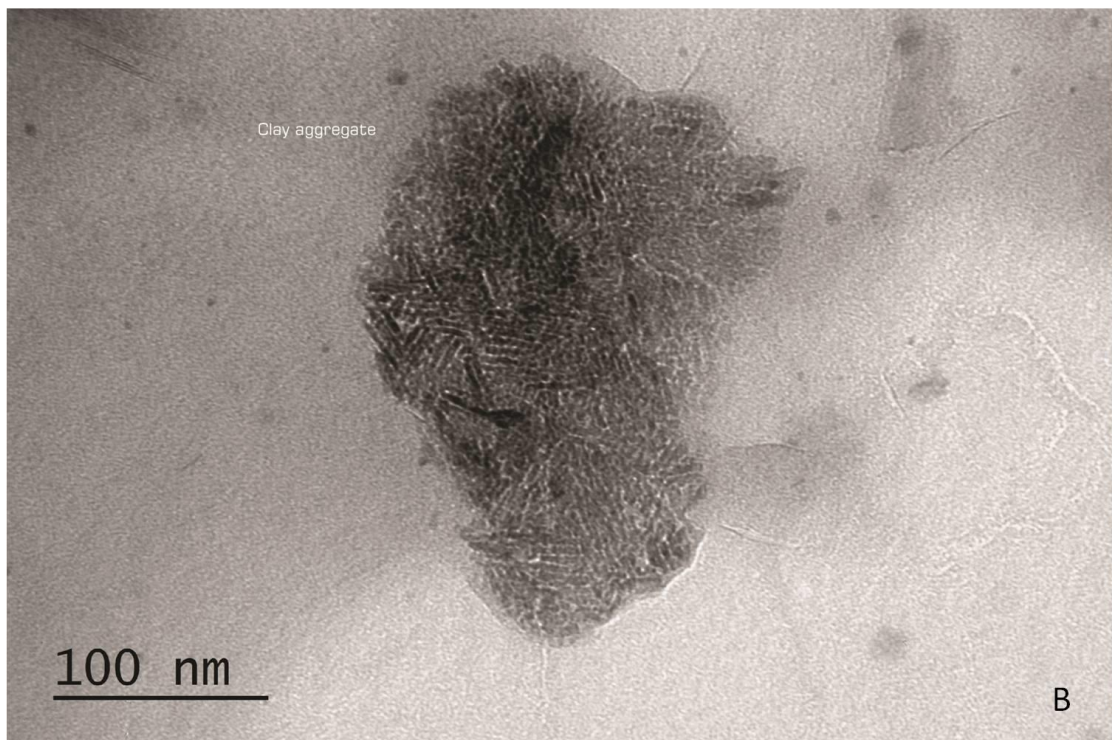
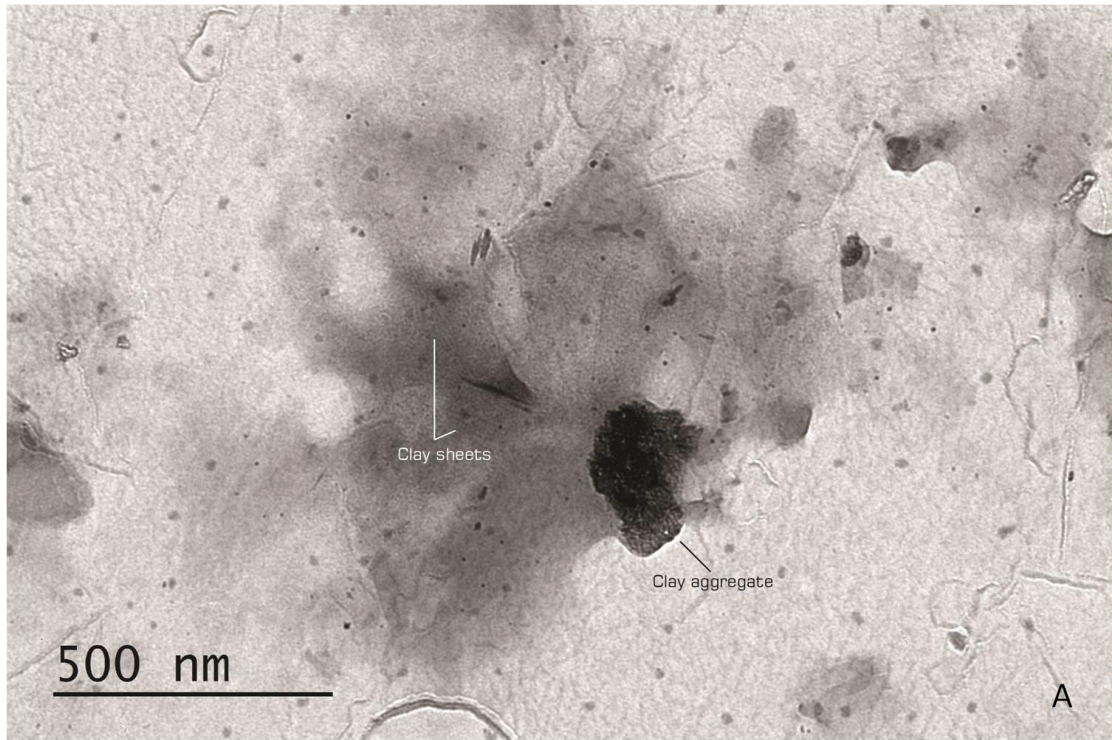


Figure 43. TEM Images of Fe-clay sample.

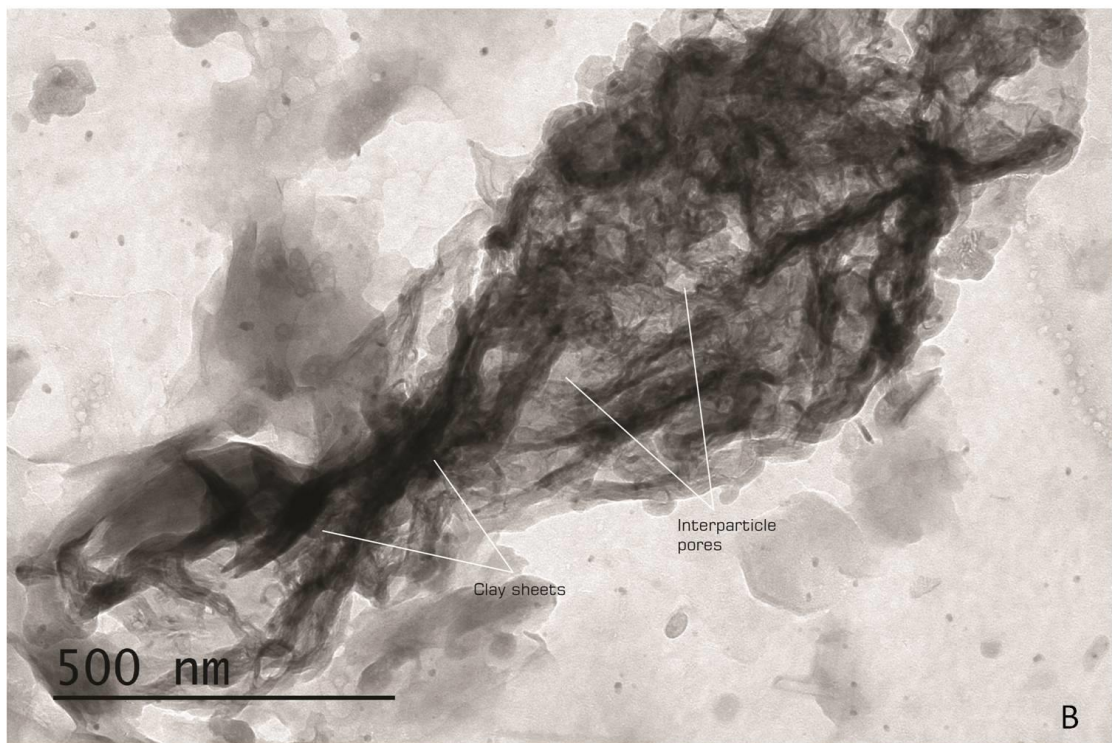
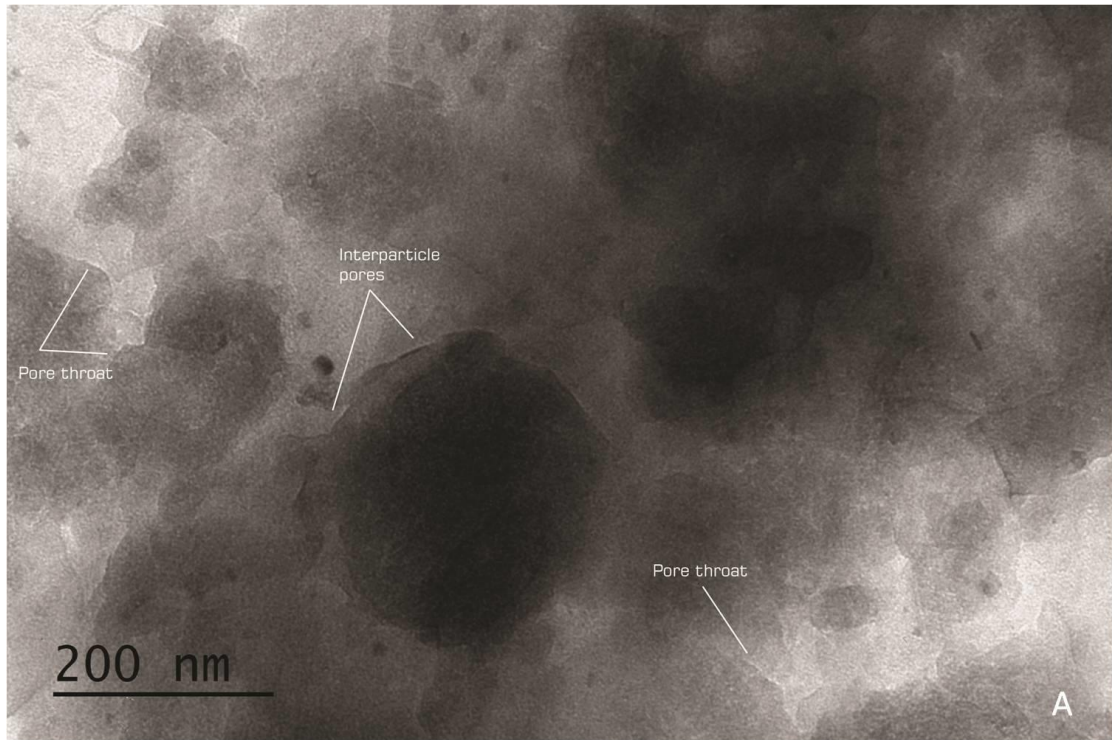


Figure 44. TEM Images of Fe-clay sample.

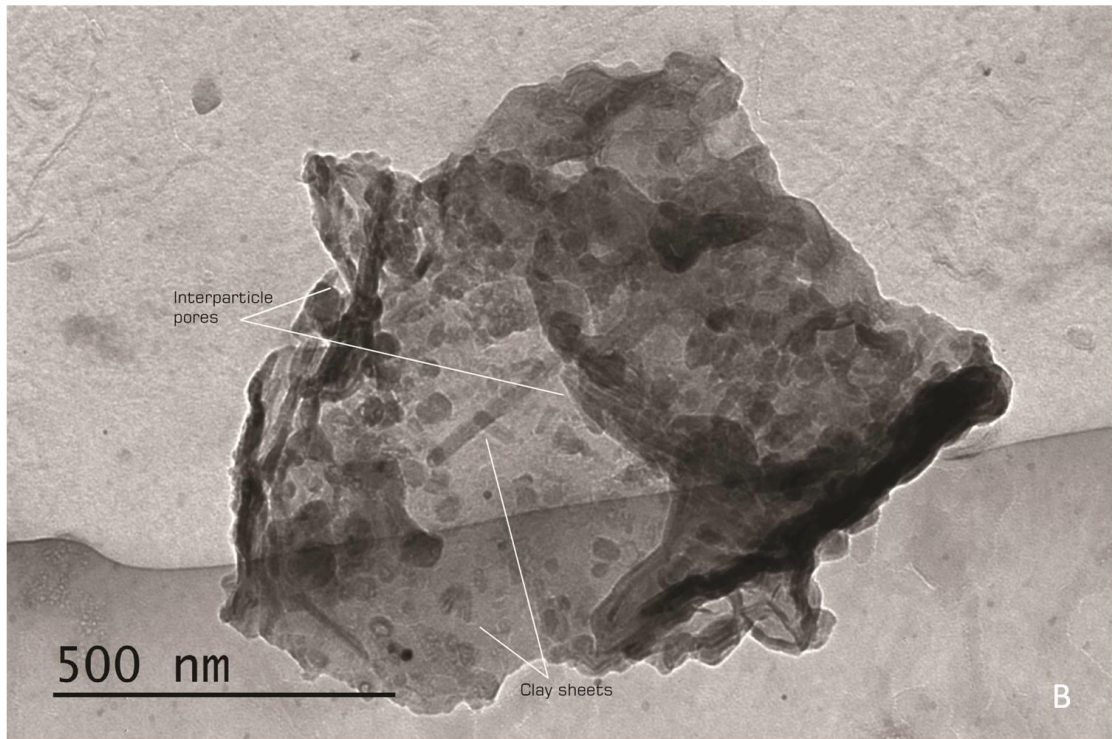
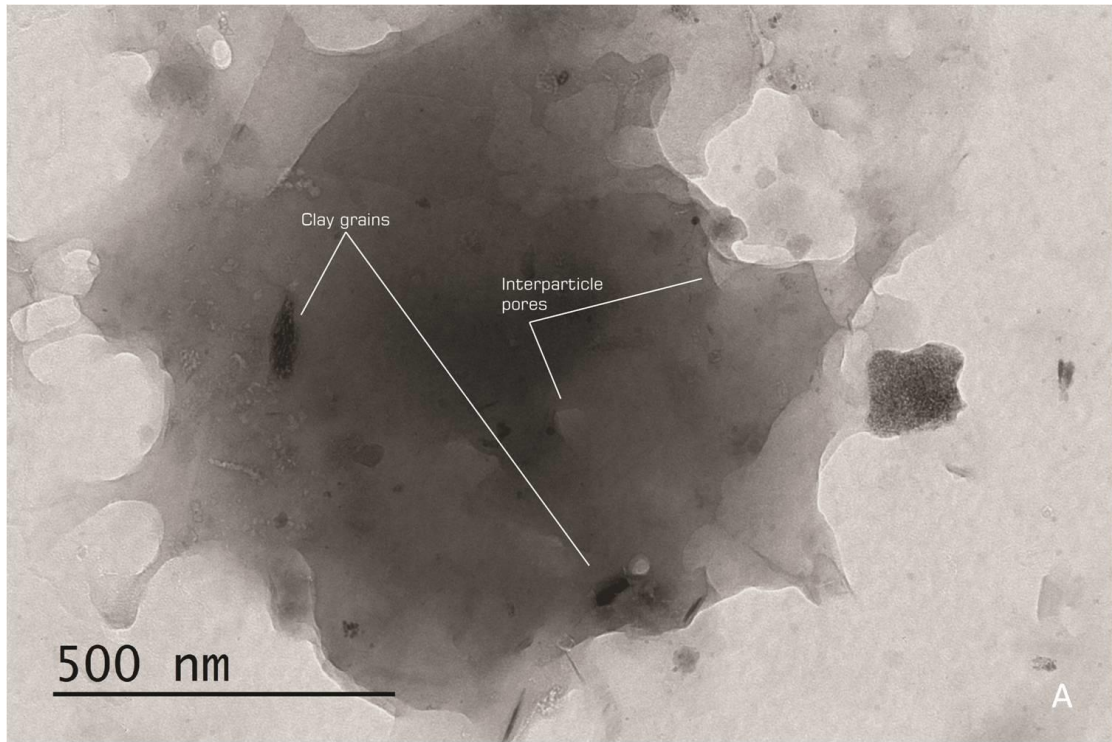


Figure 45. TEM Images of Fe-clay sample.

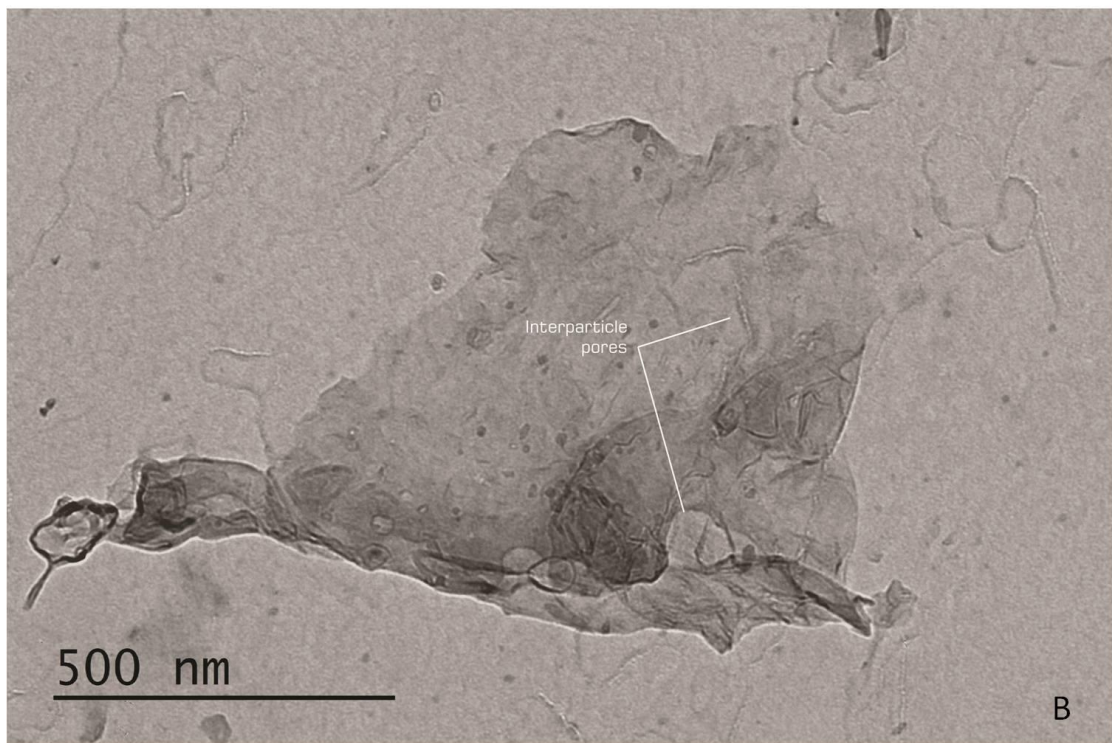
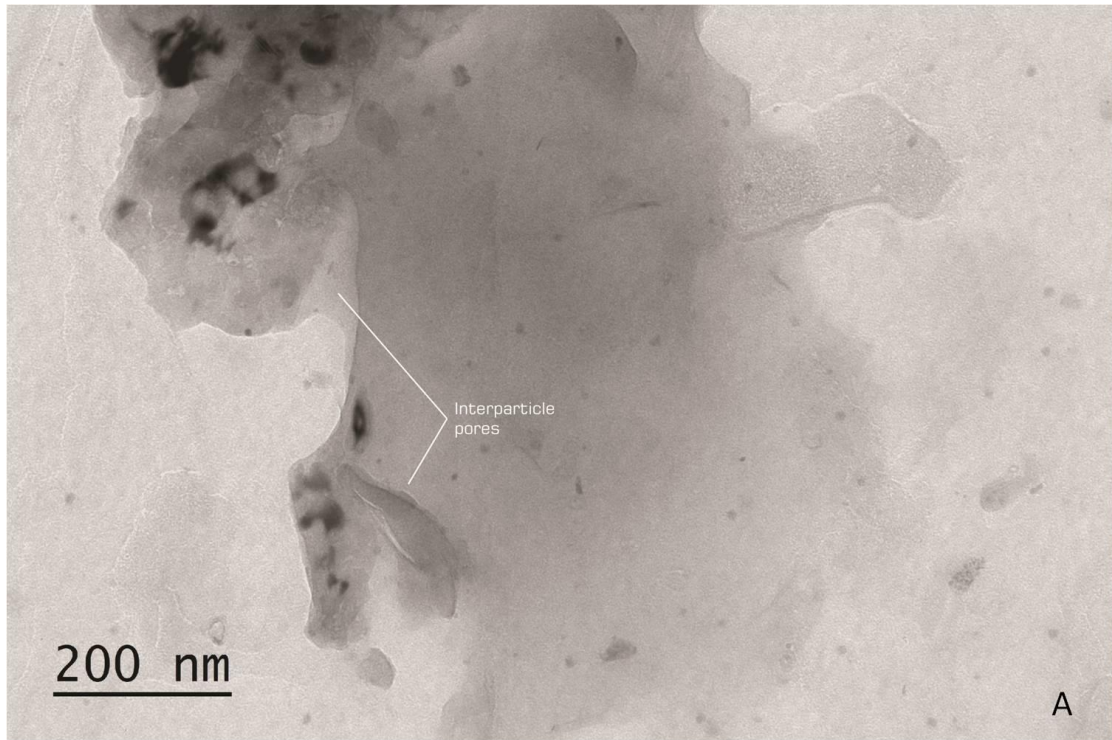


Figure 46. TEM Images of Fe-clay sample.

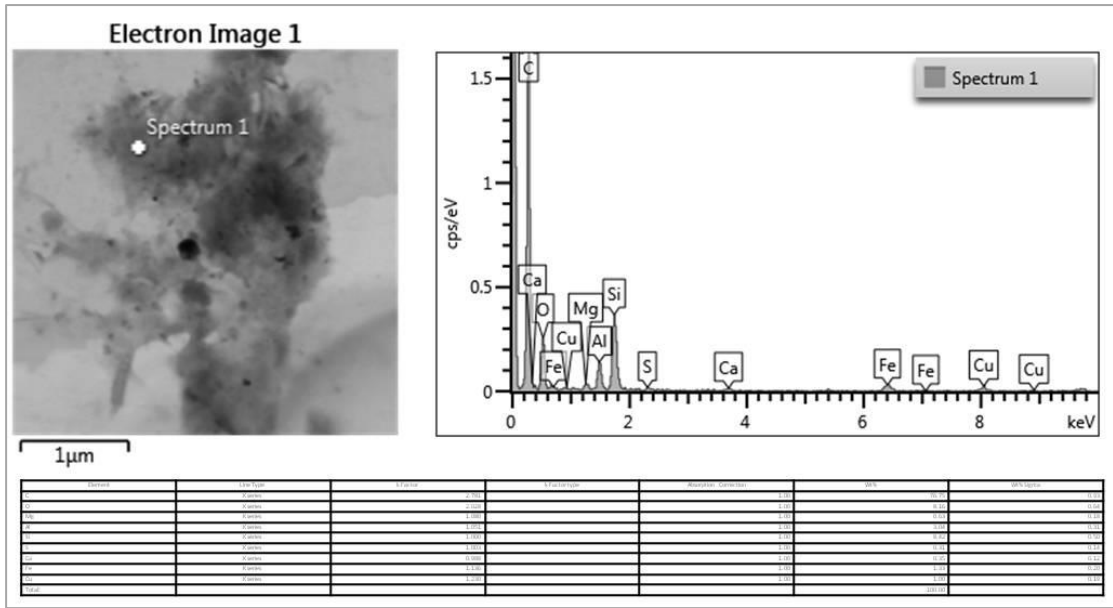


Figure 47. TEM Image, spectrum diagram and element distribution table of Fe-clay sample.

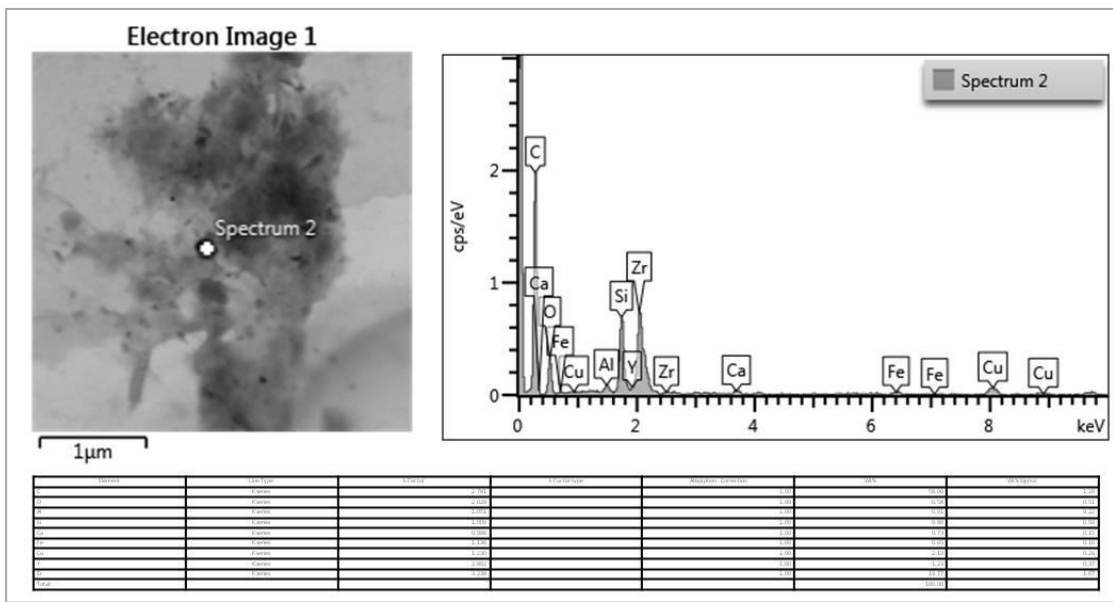


Figure 48. TEM Image, spectrum diagram and element distribution table of Fe-clay sample.

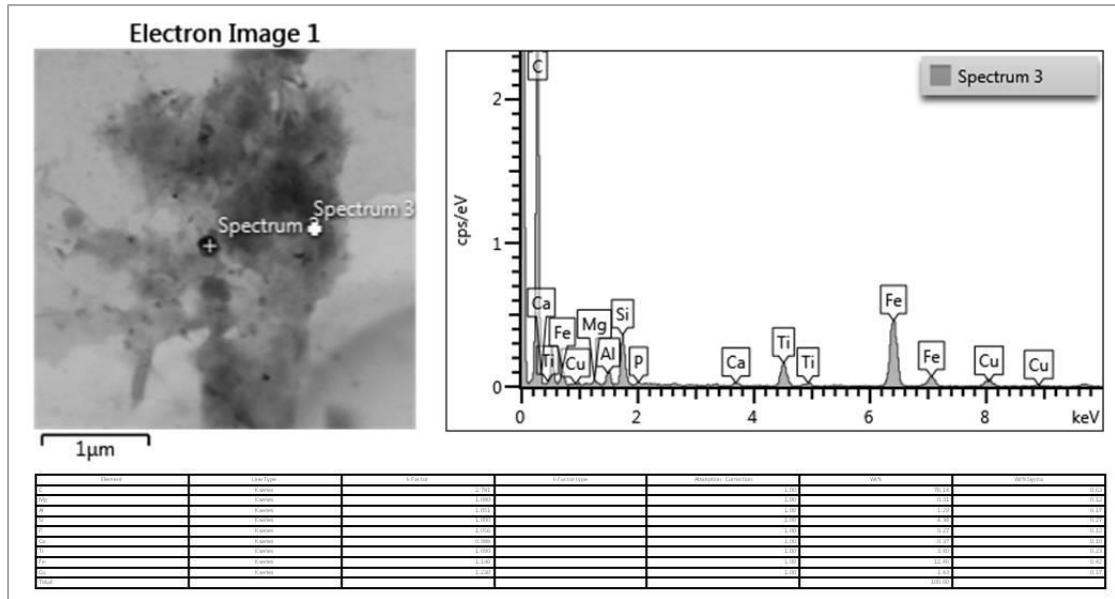


Figure 49. TEM Image, spectrum diagram and element distribution table of Fe-clay sample.

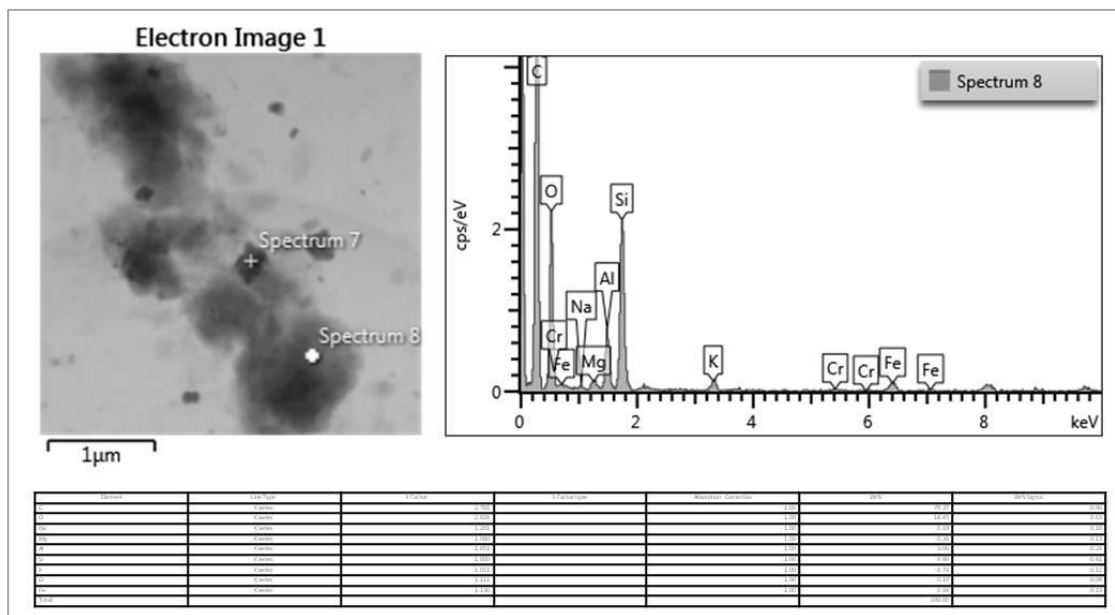


Figure 50. TEM Image, spectrum diagram and element distribution table of Fe-clay sample.

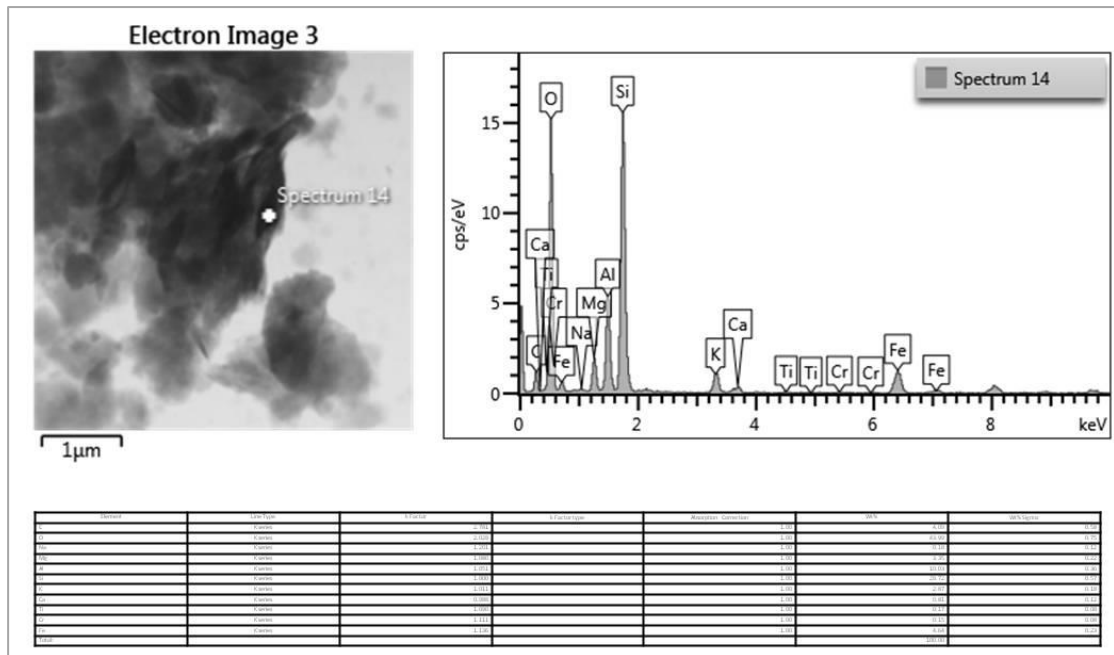


Figure 53. TEM Image, spectrum diagram and element distribution table of Fe-clay sample.

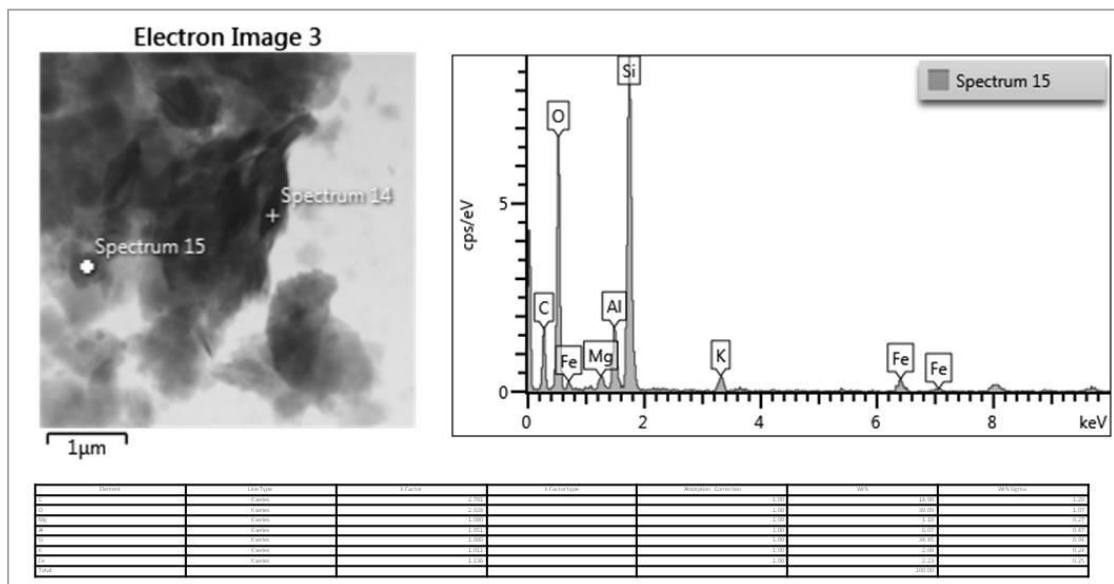


Figure 54. TEM Image, spectrum diagram and element distribution table of Fe-clay sample.

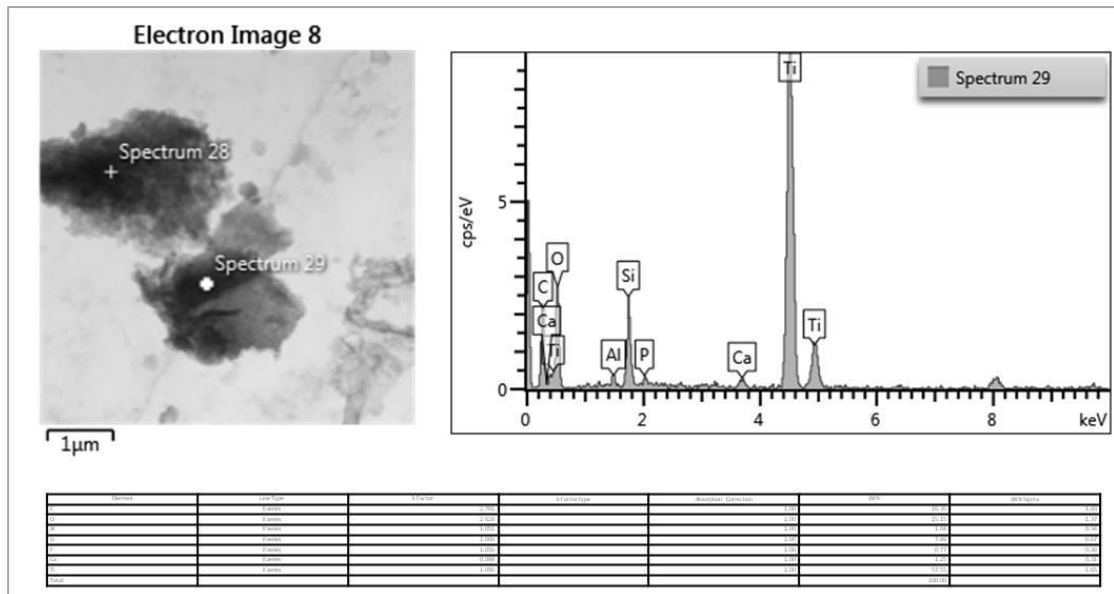


Figure 59. TEM Image, spectrum diagram and element distribution table of Fe-clay sample.

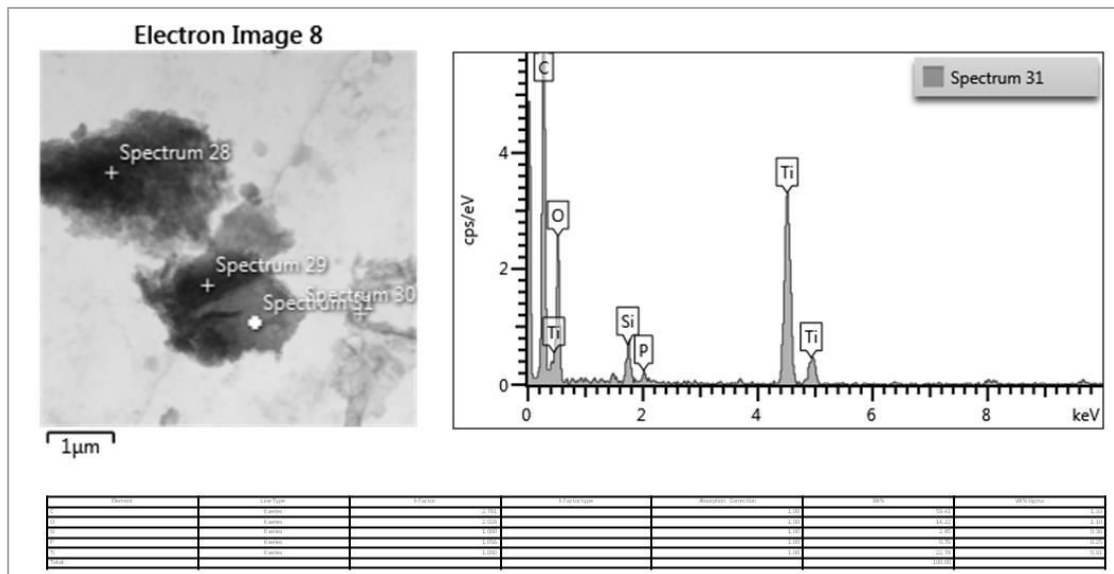


Figure 60. TEM Image, spectrum diagram and element distribution table of Fe-clay sample.

4. Discussion & Conclusions

Based upon the results presented above, mineral composition of the studied material comprises of mainly clay minerals, Fe-illite and mixed-layered clay mineral (*illite-montmorillonite*), with 80% -90% illitic layers, respectively, as well as, small quantities of calcite, quartz, apatite and a TiO₂ authigenic mineral, probably rutile or anatase. The presence of illitic layers in the observed mixed clay mineral, implies advanced diagenesis, which conforms to the origin of the material from a diagenetic product (*stylolite*) of a deep-burial diagenetic environment, above the realm of low-grade metamorphism. The specialized analytic examinations for the placement of Fe in the samples showed that Fe is positioned in the mineral structure of illite (*Fe-illite*) and probably in the illitic layers of the mixed-layered clay. The morphology of clay minerals, observed with TEM, reinforce the position of Fe in the illitic layers, as well as, late diagenetic grade of clay minerals, because of the thickness distributions.

Besides the diagenetic alterations, the authigenic provenance of clay minerals of the sample, is supported by the observed enrichment in Se and in chalcophile elements, such as Se, Zn and Cu. Th/Sc and Zr/Sc ratios, also, indicates an authigenic provenance, since they coincide with pelagic clays. The authigenic provenance complies with the nature of the surrounding limestone and the depositional environment of the formation. Besides the existence of authigenic minerals, part of the clay fracture of the sample could be part of the insoluble residue of the limestone sustained in chemical compaction and pressure dissolution. This suggestion is amplified by the presence of apatite, in addition to the detected enrichment in Ni and Co. Since there is no palaeogeographic evidence of the presence of mafic/ultra-mafic rocks close to the depositional basin of the formation, the enrichment in Ni and especially in Co could be attributed to biochemical factors, during the deposition of the original carbonate sediments.

Furthermore, sample geochemistry, enrichment in Se, Co and the negative Eu and Ce anomalies, insinuated formation under redox conditions. Although there are not any known variations in redox conditions in the Ionian basin during the Senonian, the insinuated redox conditions could be attributed either to reverberation of the known global oceanic anoxic event (OAE) of Cenomanian - Turonian age, or to the general conditions in deep-burial diagenetic environment, along with the chemical composition of subsurface brines. However, further study is needed before making any assumptions.

- The XRD pattern of the air-dried bulk oriented mount showed the presence of quartz, calcite, illite and other clay minerals. While, the XRD pattern of the air-dried clay fracture oriented mount showed the presence of illite and probably montmorillonite, as well as, the presence of mixed-layered clay mineral (*illite-montmorillonite*). The sample was characterized as illite/smectite mixed-layer with 80% -90% illitic layers, respectively.
- The SEM-EDS showed that the surrounding limestone is micrite and consists of 1 to 4 μm -diameter calcite crystals.
- The SEM-EDS study on the Fe-clay stylolite material revealed that it contains a mixed Al-Si phase, which contains measurable quantity of Fe. The presence of apatite and of a TiO_2 authigenic mineral, probably rutile or anatase, was also observed.
- The processing of the ICP-ES/MS measurements regarding the surrounding limestone sample, have indicated a clear depletion in almost every element, besides a small enrichment in Sr and a big enrichment in Se.
- Enrichment in Se, was also observed in the non-carbonate samples.
- Both stylolite material and the Fe-clay, present similar chemical imprints.
- The two samples have indicated a clear enrichment in chalcophile elements, such as Se, Zn and Cu, while only the bulk stylolite material shows enrichment in Cd.
- The bulk stylolite material is more enriched in High-Field Strength Elements (HFSE), than the Fe-clay, which could be attributed in the presence of apatite.
- Depletion was observed in metalloids, for both non-carbonate samples, while there is a big enrichment in siderophile elements, such as Co and Ni.
- A comparison of the mean metal concentrations in the studied samples with the corresponding values of these metals in the average shale revealed that there is enrichment in P, some REE, Se, Cu, Co, and Ni, while there is depletion in Mo and As.
- Th/Sc and Zr/Sc ratios of non-carbonate samples indicated an authigenic provenance, since they coincide with pelagic clays.
- All the samples showed negative Eu and Ce anomalies, which imply variations in redox conditions in the Ionian basin.
- Mössbauer spectroscopy results for the bulk stylolite material and Fe-clay suggest that the Fe-bearing clay minerals comprising the sample may be mostly Fe-illites, although a small portion of montmorillonites, or mixed layer clays like illite-montmorillonite, could not be rejected.
- TEM/EDS results for the Fe-clay sample showed that thickness distributions are characterized by a positive skew, with mode values around 6-11 nm. That clay packets show high density of high high-angle boundaries, areas with packets parallel to sub-parallel to each other and packets with variable contrast as a consequence of variable-layer orientation and curved morphologies. Also, significant amount of small intraparticle pores (<5 nm) were found in sample, whose shapes trend to be irregular ellipsoidal or unrounded. Interparticle pores were, also, observed, some of which associated with clay sheets.

Future research on illite, by the illite-crystallinity (IC) method, which is applied in petroleum exploration to detect diagenetic stages, but essentially to characterize the ultimate evolution stages before metamorphism, might prove important as it could extend our knowledge on the deep burial diagenetic environment and the formation of stylolites.

5. References

- Algeo, T. J., & Maynard, J. B. (2004). Trace-element behavior and redox facies in core shales of Upper Pennsylvanian Kansas-type cyclothems. *Chemical geology*, 206(3-4), 289-318.
- Aubouin, J. (1959). *Contribution à l'étude géologique de la Grèce septentrionale: les confins de l'Épire et de la Thessalie; Place des Hellénides parmi les édifices structuraux de la Méditerranée orientale*. Laboratoire de géologie de l'Université.
- Bailey, S. W. (1980). Summary of recommendations of AIPEA nomenclature committee on clay minerals. *American Mineralogist*, 65(1-2), 1-7.
- Bancroft, G. M. (1973). *Mössbauer spectroscopy: An introduction for inorganic chemists and geochemists*. Halsted press.
- Barnes, S.J. (2016). Chalcophile elements. *Encyclopedia of Geochemistry: A Comprehensive Reference Source on the Chemistry of the Earth*, 1-5.
- Bathurst, R. G. C., 1975. Carbonate sediments and their diagenesis. *Developments in Sedimentology* 12. (Second Edition) Elsevier/Amsterdam, 658 pp.
- Bathurst, R. G. C., 1984. The integration of pressure-solution with mechanical compaction and cementation. In: *Stylolite and Associated Phenomena Relevance to Hydrocarbon Reservoirs*. Abu Dhabi National Reserv. Res. Found. Spec. Pub., pp. 41-55.
- Bernoulli, D., & Renz, O. (1970). *Jurassic carbonate facies and new ammonite faunas from western Greece*.
- Bosellini, A., & Morsilli, M. (1997). A Lower Cretaceous drowning unconformity on the eastern flank of the Apulia Platform (Gargano Promontory, southern Italy). *Cretaceous Research*, 18(1), 51-61.
- Brigatti, M. F., Malferrari, D., Laurora, A., Elmi, C., & Mottana, A. (2011). Structure and mineralogy of layer silicates: recent perspectives and new trends. *Layered Mineral Structures and their Application in Advanced Technologies*, 11, 1-71.
- Broecker, W. S. Peng. T.-H. 1982. Tracers in the Sea. *Lamont-Doherty Geological Observatory, Columbia University, Palisades, NY*, 690p.
- Boynnton, W. V. (1984). Cosmochemistry of the rare earth elements: meteorite studies. In *Developments in geochemistry* (Vol. 2, pp. 63-114). Elsevier.
- Bullock, L., Parnell, J., Armstrong, J., Boyce, A., & Perez, M. (2017, April). The geological and microbiological controls on the enrichment of Se and Te in sedimentary rocks. In *EGU General Assembly Conference Abstracts* (Vol. 19, p. 3325).
- Byrne, R. H. (2002). Inorganic speciation of dissolved elements in seawater: the influence of pH on concentration ratios. *Geochemical Transactions*, 3(1), 11.

- Byrne, R. H., & Kim, K. H. (1990). Rare earth element scavenging in seawater. *Geochimica et Cosmochimica Acta*, 54(10), 2645-2656.
- Choquette, P. W., & Pray, L. C. (1970). Geologic nomenclature and classification of porosity in sedimentary carbonates. *AAPG bulletin*, 54(2), 207-250.
- Choquette, P. W., & James, N. P. (1987). Diagenesis# 12. Diagenesis in Limestones-3. The deep burial environment. *Geoscience Canada*, 14(1).
- Coey, J. M. D., Schindler, D. W., & Weber, F. (1974). Iron compounds in lake sediments. *Canadian Journal of Earth Sciences*, 11(10), 1489-1493.
- Davison, W., & Dickson, D. P. E. (1984). Mössbauer spectroscopic and chemical studies of particulate iron material from a seasonally anoxic lake. *Chemical geology* 42(1-4), 177-187.
- De Baar, H. J., German, C. R., Elderfield, H., & Van Gaans, P. (1988). Rare earth element distributions in anoxic waters of the Cariaco Trench. *Geochimica et Cosmochimica Acta*, 52(5), 1203-1219.
- Drits, V. A., Dainyak, L. G., Muller, F., Besson, G., & Manceau, A. (1997). Isomorphous cation distribution in celadonites, glauconites and Fe-illites determined by infrared, Mössbauer and EXAFS spectroscopies. *Clay minerals*, 32(2), 153-179.
- Drodt, M., Lougear, A., Trautwein, A. X., König, I., Suess, E., & Koch, C. B. (1998). Studies of iron in deep-sea sediments by Mössbauer spectroscopy. *Hyperfine Interactions*, 117(1-4), 383-403.
- Elderfield, H. (1988). The oceanic chemistry of the rare-earth elements. *Philosophical Transactions of the Royal Society of London. Series A, Mathematical and Physical Sciences*, 325(1583), 105-126.
- Elderfield, H., & Sholkovitz, E. T. (1987). Rare earth elements in the pore waters of reducing nearshore sediments. *Earth and Planetary Science Letters*, 82(3-4), 280-288.
- Erel, Y., & Stolper, E. M. (1993). Modeling of rare-earth element partitioning between particles and solution in aquatic environments. *Geochimica et Cosmochimica Acta*, 57(3), 513-518.
- Folk, R. L. (1959). Practical petrographic classification of limestones: American Association of Petroleum Geologists Bulletin, v. 43.
- Folk, R. L. (1962). Spectral subdivision of limestone types.
- François, R. (1988). A study on the regulation of the concentrations of some trace metals (Rb, Sr, Zn, Pb, Cu, V, Cr, Ni, Mn and Mo) in Saanich Inlet sediments, British Columbia, Canada. *Marine Geology*, 83(1-4), 285-308.
- Galehouse, J.S. (1971) Sedimentation analysis. In: *Procedures in Sedimentary Petrology* (Ed. by R.E. Carver), pp. 65—94. Wiley-Interscience, New York

- German, C. R., & Elderfield, H. (1989). Rare earth elements in Saanich Inlet, British Columbia, a seasonally anoxic basin. *Geochimica et Cosmochimica Acta*, 53(10), 2561-2571.
- Goldberg, E. D. (1963). Mineralogy and chemistry of marine sedimentation. *Submarine geology*, 436-466.
- Goldberg, E. D., Koide, M., Schmitt, R. A., & Smith, R. H. (1963). Rare-Earth distributions in the marine environment. *Journal of Geophysical Research*, 68(14), 4209-4217.
- Hannigan, R., Dorval, E., & Jones, C. (2010). The rare earth element chemistry of estuarine surface sediments in the Chesapeake Bay. *Chemical Geology*, 272(1-4), 20-30.
- Haskin, L. A., Haskin, M. A., Frey, F. A., & Wildeman, T. R. (1968). Relative and absolute terrestrial abundances of the rare earths. In *Origin and Distribution of the Elements* (pp. 889-912). Pergamon.
- Heggie, D., & Lewis, T. (1984). Cobalt in pore waters of marine sediments. *Nature*, 311(5985), 453.
- Herber, R. H. (2012). *Chemical Mössbauer Spectroscopy*. Springer Science & Business Media.
- Hilton, J., Long, G. J., Chapman, J. S., & Lishman, J. P. (1986). Iron mineralogy in sediments. A Mössbauer study. *Geochimica et Cosmochimica Acta*, 50(10), 2147-2151.
- Ho, T. Y., Quigg, A., Finkel, Z. V., Milligan, A. J., Wyman, K., Falkowski, P. G., & Morel, F. M. (2003). THE ELEMENTAL COMPOSITION OF SOME MARINE PHYTOPLANKTON 1. *Journal of phycology*, 39(6), 1145-1159.
- Kabata-Pendias, A., & Pendias, H. (2001). Trace elements in soils and plants CRC Press Inc. Boca Raton, FL, USA.
- Katz, A. M. I. T. A. I., Sass, E., Starinsky, A., & Holland, H. D. (1972). Strontium behavior in the aragonite-calcite transformation: An experimental study at 40–98 C. *Geochimica et Cosmochimica Acta*, 36(4), 481-496.
- Karakitsios, V. (1990). *Chronologie et géométrie de l'ouverture d'un bassin et de son inversion tectonique: Le bassin ionien (Epire, Grèce)* (Doctoral dissertation, Paris 6).
- Karakitsios, V. (1992). Ouverture et inversion tectonique du bassin Ionien (Epire, Grèce). In *Annales Géologiques des Pays Helléniques* (Vol. 35, pp. 185-318). Laboratoire de géologie de l'Université.
- Karakitsios, V. (1995). The influence of preexisting structure and halokinesis on organic matter preservation and thrust system evolution in the Ionian Basin, Northwest Greece. *AAPG bulletin*, 79(7), 960-980.
- Karakitsios, V. (2013). Western Greece and Ionian Sea petroleum systems. *AAPG bulletin*, 97(9), 1567-1595.

- Karakitsios, V., & Koletti, L. (1992). Critical revision of the age of the basal Vigla limestones (Ionian zone, western Greece), based on nannoplankton and calpionellids, with paleogeographical consequences, in B. Hamrsmid and J. Young, eds., Proceedings of the 4th International Nannoplankton Association Conference, Prague, Czech Republic: Knihovnicka Zemniho Plynu a Nafty, September 1991, v. 14a, p. 165–177
- Karakitsios, V., Tsikos, H., Van Breugel, Y., Bakopoulos, I., & Koletti, L. (2004). Cretaceous oceanic anoxic events in western continental Greece. *Bulletin of the Geological Society of Greece*, 36(2), 846-855.
- Karakitsios, V., & Rigakis, N. (2007). Evolution and petroleum potential of western Greece. *Journal of Petroleum Geology*, 30(3), 197-218.
- Krauskopf, K. B. (1956). Factors controlling the concentrations of thirteen rare metals in sea-water. *Geochimica et cosmochimica acta*, 9(1-2), 1-B32.
- Krauskopf KB, Bird DK (1994) Introduction to Geochemistry, 3rd Edition. McGraw Hill
- Krumbein, W.C. & Pettijohn, F.J. (1961) *Manual of Sedimentary Petrography*. Appleton-Century-Crofts, New York.
- Leybourne, M. I., & Johannesson, K. H. (2008). Rare earth elements (REE) and yttrium in stream waters, stream sediments, and Fe–Mn oxyhydroxides: fractionation, speciation, and controls over REE+ Y patterns in the surface environment. *Geochimica et Cosmochimica Acta*, 72(24), 5962-5983.
- Li, Y-H., 1991. Distribution patterns of the elements in the oceans. A synthesis, *Geochim. Cosmochim. Acta* 55:3223-3240.
- Loucks, R. G., Reed, R. M., Ruppel, S. C., & Jarvie, D. M. (2009). Morphology, genesis, and distribution of nanometer-scale pores in siliceous mudstones of the Mississippian Barnett Shale. *Journal of sedimentary research*, 79(12), 848-861.
- Manning, P. G., & Ash, L. A. (1979). Mossbauer spectral studies of pyrite, ferric and high-spin ferrous distributions in sulfide-rich sediments from Moira Lake, Ontario. *The Canadian Mineralogist*, 17(1), 111-115.
- McBride, M. B. (1994). Environmental Chemistry of soils.
- McLennan, S. M. (1989). Rare earth elements in sedimentary rocks: influence of provenance and sedimentary processes. *Geochemistry and Mineralogy of Rare Earth Elements, Reviews in Mineralogy* 21, 169-200.
- McLennan, S. M., Hemming, S., McDaniel, D. K., & Hanson, G. N. (1993). Geochemical approaches to sedimentation, provenance, and tectonics. *Special Papers-Geological Society of America*, 21-21.
- Méring, J. (1949). L'interférence des rayons X dans les systèmes à stratification désordonnée. *Acta Crystallographica*, 2(6), 371-377.

- Merriman, R. J., & Peacor, D. R. (1999). Very low-grade metapelites: mineralogy, microfabrics and measuring reaction progress. *Low-grade metamorphism*, 10-60.
- Mielke, J. E. (1979). Composition of the Earth's crust and distribution of the elements. In *Review of research on modern problems in geochemistry* (Vol. 16, pp. 9-37). UNESCO Report Paris.
- Minai, Y. (1988). 26. A MÖSSBAUER STUDY OF OCEANIC SEDIMENTS FROM SITE 612, DEEP SEA DRILLING PROJECT LEG 951. *Earthquake chemistry: collected papers*, 1, 359.
- Moffett, J. W., & Ho, J. (1996). Oxidation of cobalt and manganese in seawater via a common microbially catalyzed pathway. *Geochimica et Cosmochimica Acta*, 60(18), 3415-3424.
- Moore, C. H. (1989). *Carbonate diagenesis and porosity* (Vol. 46). Elsevier, pp. 338
- Moore, D. M., & Reynolds, R. C. (1989). *X-ray Diffraction and the Identification and Analysis of Clay Minerals* (Vol. 322, p. 321). Oxford: Oxford university press.
- Moore, C. H., & Wade, W. J. (2013). *Carbonate reservoirs: Porosity and diagenesis in a sequence stratigraphic framework*(Vol. 67). Newnes.
- Morse, J. W., & Mackenzie, F. T. (1990). *Geochemistry of sedimentary carbonates* (Vol. 48). Elsevier.
- Murad, E., & Wagner, U. (1994). The Mössbauer spectrum of illite. *Clay Minerals*, 29(1), 1-10.
- Nembrini, G. P., Capobianco, J. A., Viel, M., & Williams, A. F. (1983). A Mössbauer and chemical study of the formation of vivianite in sediments of Lago Maggiore (Italy). *Geochimica et Cosmochimica Acta*, 47(8), 1459-1464.
- Ohde, S., & Mataragio, J. (1999). Instrumental neutron activation analysis of carbonatites from Panda Hill and Oldoinyo-Lengai, Tanzania. *Journal of radioanalytical and nuclear chemistry*, 240(1), 325-328.
- Piegras, D. J., & Jacobsen, S. B. (1992). The behavior of rare earth elements in seawater: Precise determination of variations in the North Pacific water column. *Geochimica et Cosmochimica Acta*, 56(5), 1851-1862.
- Piper, D. Z., & Bau, M. (2013). Normalized rare earth elements in water, sediments, and wine: identifying sources and environmental redox conditions. *American Journal of Analytical Chemistry*, 4(10), 69-83.
- Qian, J., Xue, H. B., Sigg, L., & Albrecht, A. (1998). Complexation of cobalt by natural ligands in freshwater. *Environmental science & technology*, 32(14), 2043-2050.
- Readman, P. W., Coey, J. M. D., Mosser, C., & Weber, F. (1976). Analysis of some lake sediments from Greece. *Le Journal de Physique Colloques*, 37(C6), C6-845.
- Rollinson, H. R. (2014). *Using geochemical data: evaluation, presentation, interpretation*. Routledge.

- Rudnick, R. L., & Gao, S. (2003). Composition of the continental crust. *Treatise on geochemistry*, 3, 659.
- Saito, M. A., & Moffett, J. W. (2001). Complexation of cobalt by natural organic ligands in the Sargasso Sea as determined by a new high-sensitivity electrochemical cobalt speciation method suitable for open ocean work. *Marine chemistry*, 75(1-2), 49-68.
- Saito, M. A., & Moffett, J. W. (2002). Temporal and spatial variability of cobalt in the Atlantic Ocean. *Geochimica et Cosmochimica Acta*, 66(11), 1943-1953.
- Saito, M.A., Moffett, J.W., Chisholm, S.W., Waterbury, J.B., 2002. Cobalt limitation and uptake in *Prochlorococcus*. *Limnology and Oceanography* 47, 1629-1636
- Saito, M. A., Sigman, D. M., & Morel, F. M. (2003). The bioinorganic chemistry of the ancient ocean: the co-evolution of cyanobacterial metal requirements and biogeochemical cycles at the Archean–Proterozoic boundary? *Inorganica Chimica Acta*, 356, 308-318.
- Saito, M. A., Moffett, J. W., & DiTullio, G. R. (2004). Cobalt and nickel in the Peru upwelling region: A major flux of labile cobalt utilized as a micronutrient. *Global Biogeochemical Cycles*, 18(4).
- Savoyat, E., Monopolis, D., Katsikatsos, G., Lalechos, N., & Philippakis, N., (1962-63), Geological map of Greece, 1:50,000, I.G.M.E., sheet THESPROTIKON, Athens.
- Scholle, P.A. & Umber-Scholle, D., S., (2003), A color guide to the Petrography of Carbonate Rocks. Memoir 77, American Association of Petroleum Geologists, Tulsa, OK., pp. 474 .
- Sholkovitz, E. R., & Elderfield, H. (1988). Cycling of dissolved rare earth elements in Chesapeake Bay. *Global Biogeochemical Cycles*, 2(2), 157-176.
- Sholkovitz, E. R., & Schneider, D. L. (1991). Cerium redox cycles and rare earth elements in the Sargasso Sea. *Geochimica et Cosmochimica Acta*, 55(10), 2737-2743.
- Sholkovitz, E. R., Shaw, T. J., & Schneider, D. L. (1992). The geochemistry of rare earth elements in the seasonally anoxic water column and porewaters of Chesapeake Bay. *Geochimica et Cosmochimica Acta*, 56(9), 3389-3402.
- Starkey, H. C., Blackmon, P. D., & Hauff, P. L. (1984). The routine mineralogical analysis of clay-bearing samples. *Geological Survey bulletin (USA)*. no. 1563.
- Sunda, W. G., & Huntsman, S. A. (1995). Cobalt and zinc interreplacement in marine phytoplankton: biological and geochemical implications. *Limnology and Oceanography*, 40(8), 1404-1417.
- Swanner, E. D., Planavsky, N. J., Lalonde, S. V., Robbins, L. J., Bekker, A., Rouxel, O. J., Saito, M. A., Kappler, A., Mojzsis, S. J., & Konhauser, K. O. (2014). Cobalt and marine redox evolution. *Earth and Planetary Science Letters*, 390, 253-263.
- Taylor, S. R., & McLennan, S. M. (1985). The continental crust: its composition and evolution.

- Tucker M.E., (2001), *Sedimentary petrology: an introduction to the origin of sedimentary rocks*, John Wiley and sons, pp. 251
- Tucker, M. E. (1988). *Techniques in sedimentology* (No. 552.5. 08 TEC).
- Tucker, M., E. & Wright, V., P., (1990), *Carbonate sedimentology*, Oxford, Blackwell Scientific Publications. pp.482.
- Tucker, M. E., & Bathurst, R. G. (Eds.). (2009). *Carbonate diagenesis* (Vol. 69). John Wiley & Sons.
- Turekian, K. K., & Wedepohl, K. H. (1961). Distribution of the elements in some major units of the earth's crust. *Geological Society of America Bulletin*, 72(2), 175-192.
- Tzifas, I. T., Godelitsas, A., Magganas, A., Androulakaki, E., Eleftheriou, G., Mertzimekis, T. J., & Perraki, M. (2014). Uranium-bearing phosphatized limestones of NW Greece. *Journal of Geochemical Exploration*, 143, 62-73.
- Ure, A. M., & Berrow, M. L. (1982). The elemental constituents of soils. *Environmental chemistry*, 2, 94-204.
- Velde, B. (1992). *Introduction to clay minerals: chemistry, origins, uses and environmental significance*. Chapman and Hall Ltd.
- Weaver, C. E. (1989). *Clays, muds, and shales*, vol. 44, Elsevier
- Weaver, C. E., & Pollard, L. D. (1973). *The chemistry of clay minerals* (Vol. 15). Elsevier.
- White, W. M. (2013). *Geochemistry*. John Wiley & Sons.
- Yee, N., & Fein, J. B. (2003). Quantifying metal adsorption onto bacteria mixtures: a test and application of the surface complexation model. *Geomicrobiology Journal*, 20(1), 43-60.